Biomedical Applications of Magnetic Nanoparticles

Dissertation

Zur Erlangung des Grades des Doktors der Naturwissenschaften

der Naturwissenschaftlich-Technischen Fakultät III

der Universität des Saarlandes

von

Mohaned Hammad

Saarbrücken

2016

Tag des Kolloquiums:	25.11.2016
Dekan:	Prof. Dr. G. Kickelbick
Berichterstatter:	Prof. Dr. R. Hempelmann
	Prof. Dr. M. Schneider
Akad. Beisitzer:	Dr. M. Albrecht

ABSTRACT

The thesis focuses on the specific design of multifunctional magnetic nano-carriers for different biomedical areas. Different shapes of core/shell bi-magnetic nanoparticle have been synthesized by seed-mediated growth, and their structural and magnetic properties have been studied. The experimental results showed that core/shell nanoparticles have a higher specific absorption rate compared to the core ones. For drug delivery application, the surface of the magnetic nanoparticles is functionalized using different techniques (Diels-Alder reaction and layer-by-layer technique).

More precisely, a novel bi-functional thermo-responsive system, which consists of core/shell bi-magnetic nanoparticles with furan surface functionality, is bonded with N-(2-Carboxyethyl)maleimide through Diels-Alder reaction. The chemotherapeutics doxorubicin is attached onto the surface of the nano-carriers, and a high loading efficiency of 92% is obtained. This system with high responsiveness to a high frequency external alternating magnetic field shows a very good therapeutic efficiency in hyperthermia and drug release at relatively low temperatures (50 °C). On the other hand, a switch-controlled drug release is realized by coating the core/shell bi-magnetic nanoparticle with a pH- and thermo-responsive polymer shell. Doxorubicin is loaded onto the surface of the last coating layer, and a high loading efficiency is obtained. The nano-carriers are characterized with FTIR, dynamic light scattering, Zeta potential, *In vitro* hyperthermia, and vibrating sample magnetometry. The *in vitro* drug release experiments confirm that a small amount of doxorubicin is released at body temperature and physiological pH, whereas a high drug release is obtained at acidic tumor pH under hyperthermia conditions (43 °C). The core/shell bi-magnetic nano-carriers facilitate controllable release of doxorubicin as effect of induced thermo- and pH-responsiveness of the polymer when are subjected to an high-frequency alternating magnetic field at acidic pH; thereby the drug release rate is controlled using on-off cycles of the applied field.

KURZFASSUNG

Diese Arbeit befasst sich mit der speziellen Gestaltung von multifunktionalen magnetischen Nanopartikeln für diverse biomedizinische Anwendungen. Verschiedene Formen der Kern/Schale-bi-magnetischen Nanopartikel wurden durch die „seed-mediated growth“ Methode synthetisiert, und die strukturellen und magnetischen Eigenschaften dieser Formen untersucht. Die Versuchsergebnisse haben gezeigt, dass die Kern/Schale-Nanopartikel eine höhere spezifische Energiea als reine Kern Partikel haben. Für die Drug Delivery Anwendung wird die Oberfläche der magnetischen Nanopartikel auf unterschiedlichen Wege (Diels-Alder-Reaktion und Layer-by-Layer-Verfahren) funktionalisiert.

Dazu wurde an ein neuartiges bifunktionelles thermosensitives System, welches aus furanbeschichteten Kern/Schale bi-magnetischen Nanopartikel besteht, N-(2-Carboxyethyl) maleimid durch Diels-Alder Reaktion angebunden. Mit der Anbindung des chemotherapeutischen Doxorubicins an die Oberfläche der nano-carriers wurde ein hohe Beladungsgrad von 92% erzielt. Dieses System mit hoher Ansprechempfindlichkeit auf hochfrequente äußere magnetische Wechselfelder zeigt eine sehr gute therapeutische Wirksamkeit in der Hyperthermie und als Drug-Delivery-System bei relativ niedrigen Temperaturen (50 °C). Ein schaltbare Wirkstofffreisetzung wird durch Beschichtung der Kern/Schale bimagnetischen Nanopartikel mit einer pH- und temperaturempfindlichen Polymerschicht ermöglicht. Mit der Anbringung des Doxorubicins auf die Oberfläche der letzten Beschichtung wurde eine hohe Beladungseffizienz erhalten. Diese System wird mittels dynamischer Lichtstreuung, FT-IR-, In-vitro-Hyperthermie, UV/Vis- und Fluoreszenz-Spektroskopie, sowie Zetapotential-Messungen charakterisiert. Die *in vitro* Wirkstofffreisetzungsversuche bestätigen, dass eine kleine Menge von Doxorubicin bei Raumtemperatur und physiologischen pH freigesetzt wird, während eine hohe Wirkstofffreisetzung bei sauren pH-Werten in Tumoren unter Hyperthermi Bedingungen (43 ° C) erhalten wird. Die Kern/Schale bi-magnetischen Nanopartikel erleichtern die Freisetzung von Doxorubicin infolge der induzierten thermo- und pH-Ansprechempfindlichkeit des Polymers, wenn sie in einem hochfrequenten magnetischen Wechselfeld einem sauren pH-Wert ausgesetzt werden. Dadurch wird die Arzneimittelfreisetzungsrate anhand on-off -Zyklen des angelegten Feldes gesteuert.

TABLE OF CONTENTS

LIST OF TABLES

LIST OF FIGURES

1 INTRODUCTION

Healthcare and life science applications have drawn a great deal of interest for nanotechnology based systems and solutions. Nanostructured drugs and targeted drug delivery, sensing of target molecules, and imaging of cell and tissues are just a few examples for applications in medicine. However a wide variety of materials are used in medicine, the magnetic nanoparticles (MNPs) seem to hold one of the fastest moving and most exciting research areas. MNPs have a diverse range of applications from engineering to biomedical aspects. In fact, the application of MNPs to target tumor cells inside the human body was first conceived in the late 1970's.[1,2] The key point was to inject the attached anticancer drugs to small magnetic spheres inside the body and concentrate the drug-loaded particles inside the tumor tissue under applying external magnetic fields (AMF), in order to reduce drug payload, and thereby reduce the side effects associated with chemotherapeutic agents.

The present dissertation is an attempt to solve some of today's most important problems that drive to the side effect of chemotherapy and extend the hyperthermic effect of the MNPs with novel design and functionality of MNPs. In principle, this doctorate thesis is divided into five parts. In the first part concerning synthesis of shape-anisotropic and core/shell magnetic nanoparticles (CS-MNPs), physical properties, and surface modification for hyperthermia application are reviewed. The study presents the effects of substitution of Zn^{2+} on the structural and magnetic properties of $Zn_xCo_{1-x}Fe_2O_4@MnFe_2O_4$ nanoparticles, which affect the specific absorption rate (SAR), and thus may extend hyperthermia therapy to deeper tumors.

Part 2 focuses on the control and characterization of magnetic properties of the $Zn_{0.4}Co_{0.6}Fe_2O_4@Zn_{0.4}Mn_{0.6}Fe_2O_4$ nanoparticles, which enhanced the SAR of bi-magnetic nanoparticles. This research has been focused on chemical synthesis of truncated octahedron CS-MNPs in order to improve their SAR, which can suppress the amount of injected CS-MNPs in cancer therapy and heat shock protein because of improved heating efficiency of CS-MNPs. The study demonstrates that the SAR could be tuned by the concentration of precursor and the synthesis time, and reveals the relationship between the heating performance and the magnetic properties at high frequency.

In part 3 we develop a facile method which is based on functionalized CS-MNPs, which consists of shape-anisotropic CS-MNPs, functionalized with doxorubicin (DOX) via a thermo-responsive linker, and demonstrate a controlled drug release system upon exposure to high-frequency alternating magnetic field

(HF-AMF) radiation based on the retro-Diels/Alder (rDA) reaction. A fast drug release is activated by rDA reaction and could be applied synergistically with hyperthermia.

Alternatively in part 4 we use the layer-by-layer (LBL) technique to develop a dual pH- and thermo-responsive MNPs drug carrier which is suitable for the magneto-thermal therapy and controlled release. Poly(allylamine-hydrochloride) (PAH) and polyacrylic acid (PAA), biodegradable polyelectrolytes, will be used as functionalization agents of CS-MNPs and as external stimulus-responsive polymers. The system provides an improved controlled release of the anticancer drug over burst release when is subjected to HF-AMF and tumor acidic pH.

Finally, Part 5 summarizes the results of this doctorate work and gives conclusions of the work.

2 THEORY AND BACKGROUND

2.1 MAGNETIC NANOPARTICLES

2.1.1 Introduction

In recent years, much attention has been paid to the development of MNPs, the understanding of their behavior, and the successful application of such MNPs in the life science areas.[3] MNPs with relevant physiochemical and structural properties have been extensively investigated for various applications such as magnetic drug targeting, hyperthermia, magnetic resonance imaging (MRI), tissue engineering and repair, biosensing, biochemical separations, and bioanalysis.[4] The preparation of monodisperse-sized nanoparticles is very important because the physicochemical properties of these nanoparticles depend strongly on their dimensions. For biomedical uses, MNPs should possess very small size and narrow size distribution together with high magnetization values. The major advantage of using small size particles is their higher effective surface areas, lower sedimentation rates, and improved tissular diffusion.[5] Finally, we address some of the most relevant preparation effects on the magnetic properties and structure of the MNPs.

2.1.2 Synthesis of Magnetic Nanoparticles

During the last few years, great interest has been recently devoted to the development of shape-controlled, highly stable, and narrow size distribution MNPs with enhanced magnetic properties.

The main synthesis pathways for the preparation of MNPs are reported as follows:[6]

1) Physical methods, such as gas-phase deposition and electron beam lithography.
2) Wet chemical preparation methods, such as sol–gel synthesis, oxidation method, chemical co-precipitation, hydrothermal reactions, flow injection synthesis, thermal decomposition, aerosol/vapor-phase method, supercritical fluid method, and synthesis using nanoreactors.
3) Microbial methods, which are generally simple, efficient, versatile.

The overview focuses on thermal decomposition and co-precipitation method because it is relevant with our synthesis of magnetic nanoparticles.

2.1.2.1 Thermal decomposition

Monodisperse MNPs with smaller size can be synthesized through the thermal decomposition of organometallic compounds in high-boiling organic solvents containing stabilizing surfactants. The key

factor for the production of monodisperse MNPs can easily be obtained by controlling the ratios of the starting reagents including organometallic compounds, surfactant, and solvent reaction, as well as the experiment parameters such as temperature, heating time, and heating rate.[7] Narrow size distribution and shape control of magnetic nanoparticles can be obtained due to feature of the nucleation and growth mechanisms during the decomposition of the precursors.[8]

A large number of nuclei are formed by the formation of molecular clusters as monomers which are obtained by degradation of the precursor molecules. When the temperature increases, the concentration of these clusters increases until it reaches a critical point of supersaturation. The particles grow at the same rate, once the reaction mixture has reached a growth temperature leading to a homogeneous size distribution.[9] Particle growth can be stopped by removing the temperature source.

A burst nucleation can basically be initiated in two ways: when the monomers quickly rise over critical supersaturation, a burst nucleation occurs and thus grow at the same rate, forming monodisperse particles,[10] or by rapid injection of reagents into the reaction (figure 2.1).

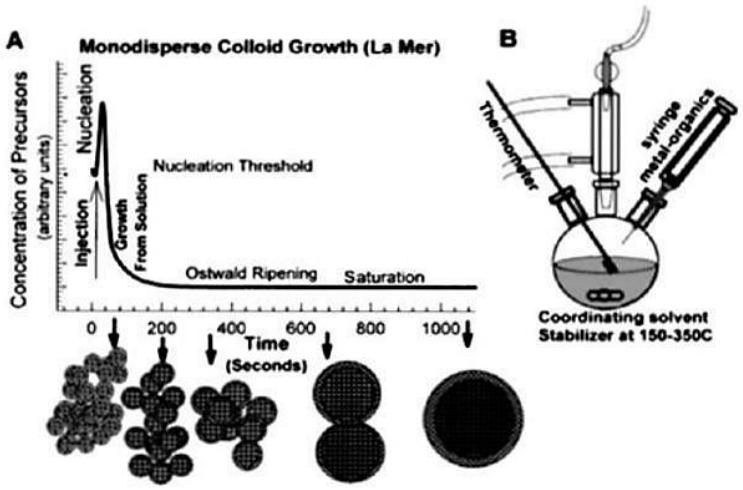

Figure 2.1. a) Schematic illustration of the LaMer model, b) a typical "hot-injection" set-up to achieve the burst nucleation. Reprinted from ref. 10.

Decomposition of nonmetal precursors such as carbonyl leads to formation of the metal nanoparticles. For instance, Hyeon *et al.* were able to prepare monodisperse γ-Fe2O3 nanocrystals with a size of approximately 13 nm by decomposition of iron pentacarbonyl at 100 °C and subsequent addition of trimethylamine oxide as a mild oxidant at elevated temperature.[11] The thermal decomposition of iron pentacarbonyl at relatively low temperature lead to nucleation, and the decomposition of the iron oleate complex at a higher temperature induces growth. Peng *et al.* reported the synthesis of size- and shape-

controlled magnetic oxide nanocrystals based on the pyrolysis of metal fatty acid salts in non-aqueous solution.[12] The size of the particles could be controlled from 3-50 nm by adjusting the precursor/surfactant ratio, the temperature, and the injection time as shown in figure 2.2.

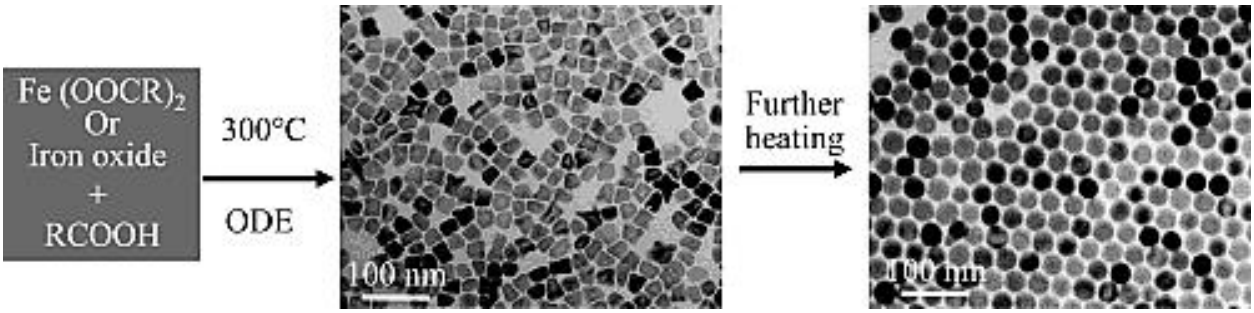

Figure 2.2. TEM images of Fe_3O_4 nanocrystals taken at different reaction times. Reprinted from ref. 12.

The thermal-decomposition method is also used for preparation of metallic nanoparticles, which have high magnetization compared to metal oxides. Metallic iron nanoparticles were synthesized by thermal decomposition of $Fe(CO)_5$ in the presence of polyisobutene in decalin under nitrogen atmosphere at 170 °C.[13]

2.1.2.2 Co-precipitation method

The co-precipitation method is considered as the convenient chemical way to synthesize iron oxide nanoparticles from aqueous Fe^{2+}/Fe^{3+} salt solutions by the addition of a base under inert atmosphere at room temperature or at elevated temperature. The MNPs prepared at or near room temperature, are usually poorly crystalline, or amorphous. On the other hand, when the co-precipitation reaction occur at higher temperatures (50-100 °C), it leads to condensation of the precipitated metal hydroxides to form crystalline metal oxides.[14]

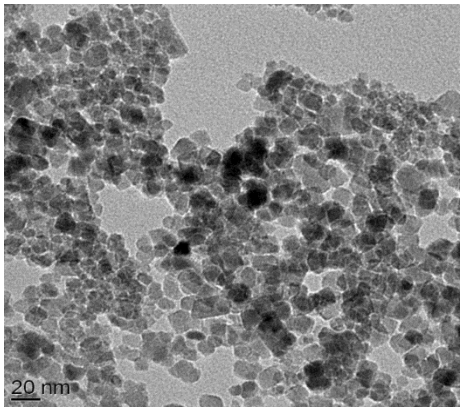

Figure 2.3. TEM image of $Zn_{0.4}Co_{0.6}Fe_2O_4$ synthesized by co-precipitation method.

Depending on the type of salts (e.g. chlorides, sulfates, nitrates), the Fe^{2+}/Fe^{3+} ratio, the reaction temperature, the pH value, and ionic strength of the media, MNPs can be produced in a highly reproducible fashion. Since the magnetite is sensitive to oxidation, an inert gas purging is needed during the reaction to prevent magnetite transformation to maghemite. The disadvantage of co-precipitation method is controlling of the particle size and thus obtaining a narrow particle size distribution. A dispersibility of nanoparticle in water can be improved by subsequent acidification of the particle surface with nitric acid or by addition of tartrate ions, giving the MNPs stability in acidic and basic media over long periods of time.[15] The main advantages of this method are the high reproducibility and high yields which are especially interesting for industrial scale applications.[16]

2.1.3 Nanomagnetism

2.1.3.1 Introduction

Nanomagnetism concerns the characteristic length scale of magnetism, which deals with the magnetic properties of objects that have at least one dimension in the nanoscopic range. The local atomic symmetry results from the crystal structure and finite-size effects due to quantum confinement of the electrons inside the material dominate the behaviour of these structures and are responsible for these unique properties.[17] Because of their extraordinary magnetic properties, nano-magnets have many applications in life science which is different from the bulk magnets, such as magnetic recording, giant magnetoresistance (GMR) devices, targeting drug delivery, MRI, magnetic hyperthermia, and bionsensors.[18] We will introduced briefly the important nanomagnetic effects, and then discuss the magnetic loss processes.

2.1.3.2 Single domain and superparamagnetism

The subdivision of MNPs according to finite-size effects are classified by: (1) The single domain limit and (2) the superparamagnetic limit, which both lead to individual material-dependent length scales. The size of the magnet has a great influence on its magnetic behavior. As the size of magnet increase, the number of domains will increase, and thus the magnetostatic energy will decrease, whereas the more domain walls will also increase the exchange and the anisotropy energies. Also the size of the magnet affect the coerecivity.[19] As shown in figure 2.4, for very small particles whose diameters are below than the critical diameter of superparamagnetism (D_{spm}), the magnetic moment is not stable, and therefore coercivity (H_c) is 0. However, the moment is stable in the range between D_{spm} and the critical diameter of a single domain (D_{sd}). Finally, for the multi-domain region, H_c decreases with increasing particle diameter.

Therefore, the magnetic nanoparticle has the maximal H_c when its diameter is equal to D_{sd}, and it will become superparamagnetic when its diameter becomes smaller than D_{spm}.[20]

.

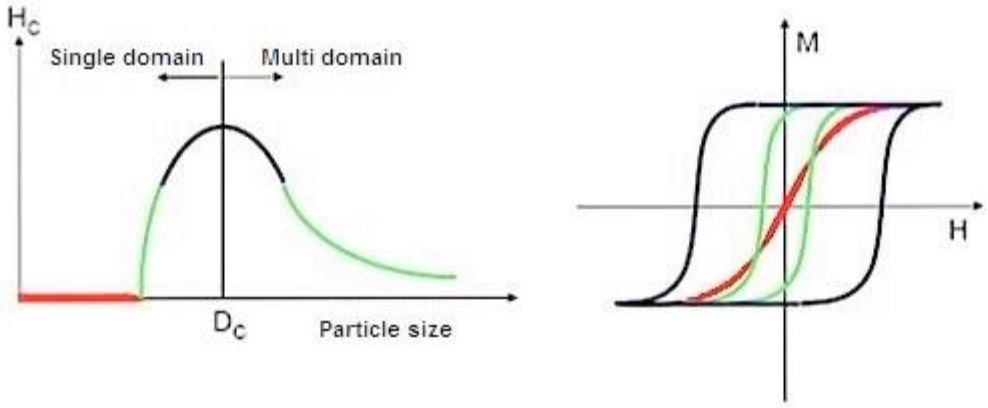

Figure 2.4. Size dependence of coercivity of magnets.

All the magnetic moments for the single domain magnet are aligned to the anisotropy axis, thus the exchange energy and anisotropy energy is zero. Therefore, the magnetostatic energy is the only dominant energy. The reason for such an arrangement arises from the fact that the thermal energy in smaller particles will be able to overcome the anisotropy energy. So the magnetization is no longer in a stable configuration. Nanoparticles with an uniaxial anisotropy randomly flip the direction of their magnetization. This effect is induced by thermal energy. The average time to perform such a flip is given by the relaxation time:[21]

$$\tau_N = \tau_0 \exp\left(\frac{KV}{k_B T}\right) \quad (2.1)$$

Where:

τ_N is the average length of time that it takes for the nanoparticle's magnetization to randomly flip as a result of thermal fluctuations, τ_0 is a length of time, characteristic of the material, called the attempt time or attempt period; its typical value is $10^{-9} – 10^{-10}$ second, K is the nanoparticle's magnetic anisotropy energy density and V its volume. KV is therefore the energy barrier associated with the magnetization moving from its initial easy axis direction, through a "hard plane", to the other easy axis direction, k_B is the Boltzmann constant, and T is the temperature.

The *KV* is usually much higher than the thermal energy k_BT, however, with decreasing of particle size, *KV* decreases to values below k_BT. As a result, the magnetic moments are able to overcome the energy barrier and freely flip in any direction, this phenomenon is called superparamagnetism.

Another factor in observing superparamagnetism is the measurement time (τ_m). When the τ_m is much less than the Neel relaxation time ($\tau_m < \tau_N$), a blocked state occurs because there is no direction flip. In this state, the nanomaterials behave like a normal paramagnet but with a much higher susceptibility. When the τ_m is much greater than the Neel relaxation time ($\tau_m > \tau_N$), this results in the superparamagnetic state in which the net moment is zero due to the fluctuations in magnetization.[22] The blocking temperature (T_B) is the temperature between the blocked and superparamagnetic states, or the temperature at which $\tau_m = \tau_N$. It can be calculated by the following equation:

$$T_B = \frac{\Delta E}{K_B \ln\left(\frac{T_m}{T_0}\right)} \tag{2.2}$$

2.1.3.3 Exchange-coupling effect

Kneller and Hawig in 1991 proposed that the exchange spring magnet utilizes the epitaxy between hard and soft magnetic materials. Therefore the hard material helps retain the soft material's anisotropy, which increases its H_c (figure 2.5).[23] The exchange-coupling effect only takes place at the interphase boundary between hard and soft magnets at nanoscale. Such magnets are referred to as `exchange-spring' or `exchange-hardened' magnets and its high magnetization improved the energy product $(BH)_{max}$ .The hard phase enhances the magnetic anisotropy and stabilizes the exchange-coupled soft phase against demagnetization. For an efficient exchange coupling, the thickness of the soft phase cannot exceed about twice the wall thickness of magnetic domains in the hard phase, which typically limits the size of the soft grains to ∼10 nm, and the volume fraction of the soft phase must not be too high in order to lose a large H_c value, which limits the $(BH)_{max}$ of the composite.[24]

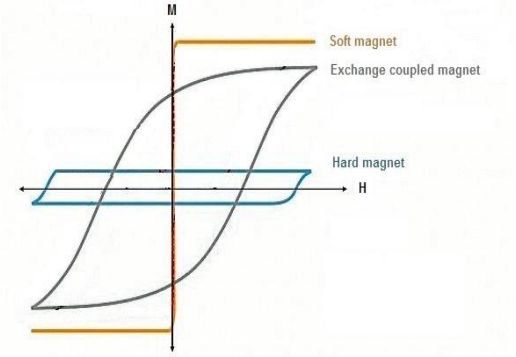

Figure 2.5. Typical hysteresis loops: (i) a hard phase, (ii) a soft phase and (iii) the exchange-coupled nanocomposites made of the soft and hard phases.

2.1.3.4 Exchange bias effect

CS-MNPs have recently received considerable attention owing to their physical and chemical properties that are strongly dependent on the structure in which the magnetic core is coated with a layer of antiferromagnetic (AFM) or ferro/ferromagnetic (FM) shell. In these systems the exchange interaction between hard and soft constituents leads to exchange bias,[25] and improvements in the thermal stability of the core.[26] These materials can exhibit desirable properties, i.e. high saturation magnetization (M_s)and high SAR arising from the hard and soft phases, respectively.[27] The magnetization of small size nanoparticles increases and the coercive field monotonically decreases as the soft-phase shell thickness is increased.[28] Moreover reversal of the FM moment will have an added energetic cost corresponding to the energy necessary to create a Néel domain wall within the AFM film, and thus implies a shift in the switching field of the FM (figure 2.6). The Curie temperature (T_c) of the FM in the FM/AFM bilayers is larger than the Néel temperature (T_N) of the AFM.

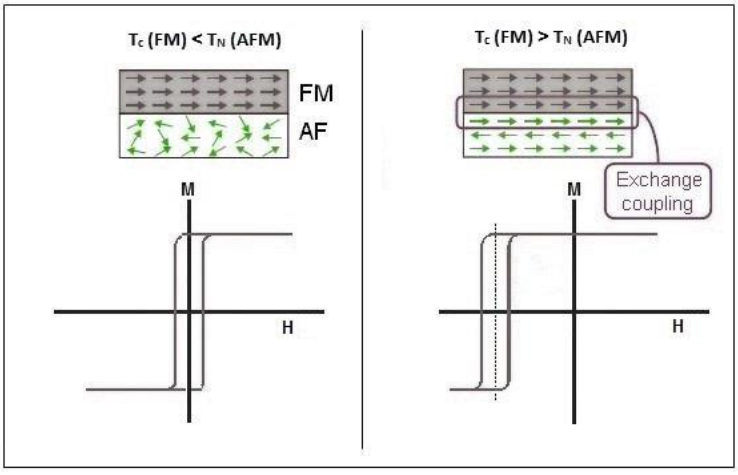

Figure 2.6. Above the T_N of the AFM all its spins are disordered. Below T_N they become ordered and the exchange coupling between FM and AFM spins leads to the shift of the hysteresis loop.

2.1.3.5 Magnetic loss process

Magnetic losses to be utilized for heating arise due to different processes of magnetization reversal in systems of magnetic nanoparticles which depend in different manners on the applied magnetic AC field amplitude and frequency. Moreover, there is a strong dependence of magnetic particle properties on structural ones like mean size, size distribution, particle shape and crystallinity. High-frequency magnetic fields may cause heating in magnetic materials due to different processes of magnetization reversal in the particle system: hysteresis loss, and Brownian and Néel relaxation.

Hysteresis loss is due to the reversal of magnetization of transformer core whenever it is subjected to alternating nature of magnetizing force .Whenever the core is subjected to an AMF, the domain will change their orientation after every half cycle. The power consumed by the magnetic domains for changing the orientation after every half cycle is called hysteresis loss. The hysteresis loss occur in magnetic particles on the order of 100 nm or larger.[29] Hysteresis remains significant in larger single-domain particles as well; however, both H_c and remanence magnetization (M_r) depend strongly on particle volume and both decrease for smaller particles.[30] This dominance occurs when the relaxation time of the particle is equal to the field frequency.

With decreasing particle size, the energy barrier for magnetization reversal decrease, and consequently thermal fluctuations lead to relaxation phenomena. When the particle rotates itself, the particle has undergone Brownian relaxation and thermal energy is delivered through shear stress in the surrounding fluid. On other hand, if the moment rotates while the particle itself remains fixed, the particle has undergone Néel relaxation and thermal energy is dissipated by the rearrangement of atomic dipole moments within the crystal (Figure 2.7).[31]

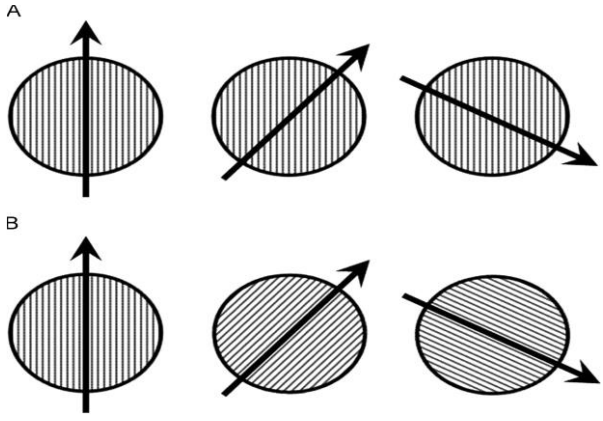

Figure 2.7. a) Néel rotation, B) Brownian rotation reprinted from ref 31.

In the absence of a field, the crystalline anisotropy of the particle affect the orientation of this moment. However, the energy produced from AMF tends to displace the moment from the preferred orientation and relaxation of the moment reverse to equilibrium releases thermal energy, which results in local heating. In the case of a Néel relaxation mechanism, the physical orientation of the particle remains unchanged while the moment alternates between parallel and antiparallel orientations (equation 2.1).[32] Heating occurs in Brownian mechanism via shear in the surrounding carrier fluid. When the magnetic anisotropy of the particle overcome the inertial or viscous resistance, an AMF may cause rotation of the particle in the fluid, while the magnetic moment remains fixed relative to the crystal axis. The viscosity of the solution η and the hydrodynamic volume of the particle V_H affect strongly the Brownian relaxation time, and is given by the following:[33]

$$\tau_B = \frac{3\eta V_H}{KT} \tag{2.3}$$

Néel and Brownian mechanisms occur in parallel, and so the effective relaxation time of the system is given by

$$\frac{1}{\tau} = \frac{1}{\tau_B} + \frac{1}{\tau_N} \tag{2.4}$$

Here it is clear that the effective relaxation time is dominated by the shorter of the two components. Thus Brownian relaxation tends to dominate at larger particle volumes and lower viscosities, and Néel for small particles in viscous solutions. In magnetic fluids, heating effects can be achieved in AC magnetic fields by Néel type relaxation losses or energy dissipation during particle rotation in liquid (Brown losses).

2.1.4 Application in life science

2.1.4.1 Drug delivery system

One of the most attractive applications for MNPs is targeted drug delivery. It is a challenge to deliver the drug to the target organ inside the body because of the circulation system and clearance system of body. Transportation of drugs to a specific site can eliminate side effects and also reduce the dosage required. Where nanoparticles are functionalized with appropriate groups loaded with drugs and directed to and focused at tumor sites by an AMF. The size, surface chemistry, and charge are particularly important for bioavailability of the drug. It is desirable that the size of MNPs is ranging from 10 to 100 nm for drug

delivery applications. A gradient magnetic field needs to be placed in terms of direction and strength of the particle. Particles will move under applied magnetic field. The force felt by a nanoparticle is given by

$$F = (m * \nabla)\, B \tag{2.5}$$

where *B* is the applied field and *m* is the magnetic moment of the particle. The process of drug localization using magnetic delivery systems is based on the competition between the forces exerted on the particles by the blood compartment and the magnetic forces generated from the magnet.

Zimmermann and Pilwat used magnetic erythrocytes for the delivery of a cytotoxic drug, methotrexate.[34] In the 1980s, many authors developed delivery strategies for various drugs using microcapsules and microspheres.[35]

2.1.4.2 Hyperthermia

Hyperthermia is a type of cancer treatment in which body tissue is exposed to high temperature. It is based on the fact that cells show signs of apoptosis when heated in the range of 41 °C to 47 °C and necrosis when heated to above 50 °C.[36] By killing cancer cells and damaging proteins and structures within cells, hyperthermia may shrink tumors.

The advantage of magnetic hyperthermia is: (a) it provides a non-invasive way to raise cell temperatures to a therapeutic level; (b) MNPs can be visualized using MRI; and (c) the particles can also be functionalized and combined with other types of treatment such as chemotherapy or radiotherapy. Maier-Hauff *et al.* studied a clinical breakthrough of therapeutic hyperthermia induced by heating implanted MNPs (figure 2.8).[37] Moreover, the use of nanometer-sized MNPs is much more than micron-sized particles in hyperthermia due to the fact that the smaller nanoparticle will absorb more power at AC magnetic field.[38]

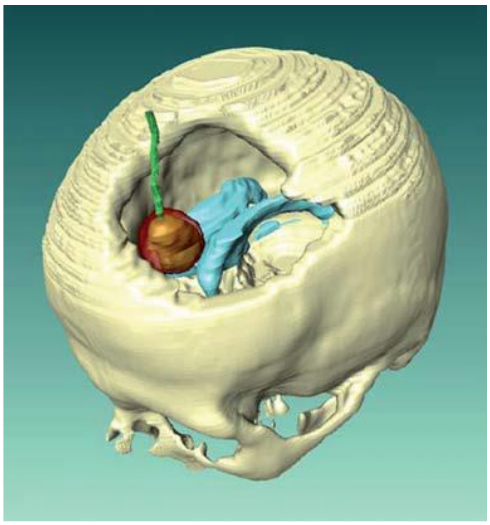

Figure 2.8. Three-dimensional reconstruction image (MagForce NanoPlan_ software) of a skull with a frontal glioblastoma multiforme after magnetic resonance imaging and computed tomography. A calculated 42 °C treatment isotherm surface (transparently red) enclosing.

2.1.4.3 MRI Contrast Agents

For many years, superparamagnetic nanoparticles have been used as contrast agent mainly for diagnosis of soft tissue or cartilage pathologies in MRI and magnetic resonance angiography (MRA). This is because of their T_2* (T = transverse relaxation) property with high sensitivity in T_2* and T_2 weighted images, when compared to other MRI agents.[39] The T_2-relaxation effects result in a signal reduction on T_2-weighted images, thus providing a dark or negative contrast due to the induction of strong magnetic susceptibility on the water protons around the particles.[40] The magnetic fluids should be dispersed into a biocompatible and biodegradable carrier. In the liver, MNPs more than 50 nm in size are rapidly taken by hepatic and splenic macrophages, resulting in hypointense T_2-weighted images of the normal tissue.[41] The lack of Küpffer cells in the tumor helps to differentiate between healthy and malignant regions. On other hand, very small MNPs avoid high uptake by liver and spleen macrophages and thus exhibit long circulating time, and it can be transported to the pathological tissues by endocytosis , transcytosis, and by direct passage through the inflammatory leaky vasculature.[42] As shown in Figure 2.9a-c, the tumor treated with the $MnFe_2O_4$–Herceptin NPs shows color changes from red to blue in the color-coded MR images.[43] In contrast, those treated with the Fe_3O_4–Herceptin NPs have no apparent change in the color-coded MR images (Figure 2.9d–f), indicating the higher MRI sensitivity can be obtained by using high moment superparamagnetic nanoparticles.

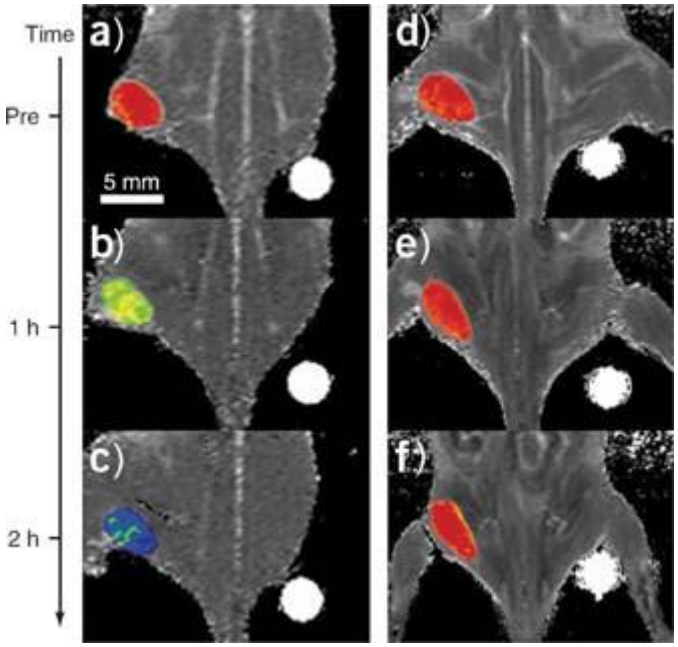

Figure 2.9. a–c) Color maps of *T2*-weighted MR images of a mouse implanted with the cancer cell line NIH3T6.7 at different time points after injection of MnFe2O4–Herceptin and d–f) Fe3O4–Herceptin conjugates. Reprinted from ref 43.

2.1.4.4 Bioseparation

Biomagnetic separation techniques are becoming most recently developed revolutionary technology in bioscience research. Magnetic micro- or nanospheres can be separated easily by an AMF and can be bonded with appropriate ligands, such as antibodies or proteins, with a high affinity to the target cells, bacteria or DNA/RNA. Biomagnetic separation is ideal for automated assay and analysis systems because of its advantages which are fast, reliable sample handling and can be used for large sample volumes without time-consuming centrifugation steps. Superparamagnetic iron oxide particles have been extensively used for separation and purification of cells and biomolecules in bioprocesses.[44]

2.2 DIELS–ALDER REACTION

2.2.1 Introduction

Remote control of the rate of drug release by using an AMF is a persistent challenge in medicine. Controlled release formulations of therapeutic molecules from a magnetic platform offer several advantages, such as delivery of the desirable amount of the drug to the target of interest and synergistic effects of hyperthermia to the affected tissue. In order to provide on-demand drug release it is necessary to have a switching material that can modulate the drug release kinetics upon an external triggering electromagnetic field. Click reactions have the potential to greatly facilitate the development of controlled drug delivery systems and biomaterials. The Diels–Alder (DA) cycloaddition is one of the click reactions that are used in synthetic organic chemistry and material design which do not need any metal catalyst. The DA reaction is efficient in the absence of catalysts, even though the reaction rate can then be slow at room temperature. Thermally rDA between various furan and maleimide derivatives have attracted particular attention because they can occur under mild conditions with high chemo-selectivity.[45] The DA reaction is stereoselective, atom economical, and highly efficient; it is one of the most powerful methods to synthesize unsaturated six-membered rings.[46]

2.2.2 Reaction mechanism

The DA reaction is known as a thermo-reversible reaction between diene and alkene derivatives (dienophiles) to form cyclic hydrocarbon chains in aqueous conditions (figure 2.10a).[47] The intramolecular DA cycloaddition occurs if both the diene and the dienophile are part of the same molecule (Figure 2.10B). Moreover, if at least one heteroatom is involved in the reaction, the reaction called hetero-DA reactions (Figure 2.10C).[48] In contrast of the normal electron-demand DA reaction, for which the reaction occurs between electron-rich dienes and electron-poor dienophiles, an alternative reaction, in which a six-membered ring is formed between an electron-poor diene and an electron-rich dienophile (Figure 2.10D).[49] Therefore, reactive dienophiles are substituted with electron withdrawing groups, such as carbonyls, ketones, carboxyls, nitriles or halogens, while dienes are substituted with electron donating groups, such as alkyl chains.

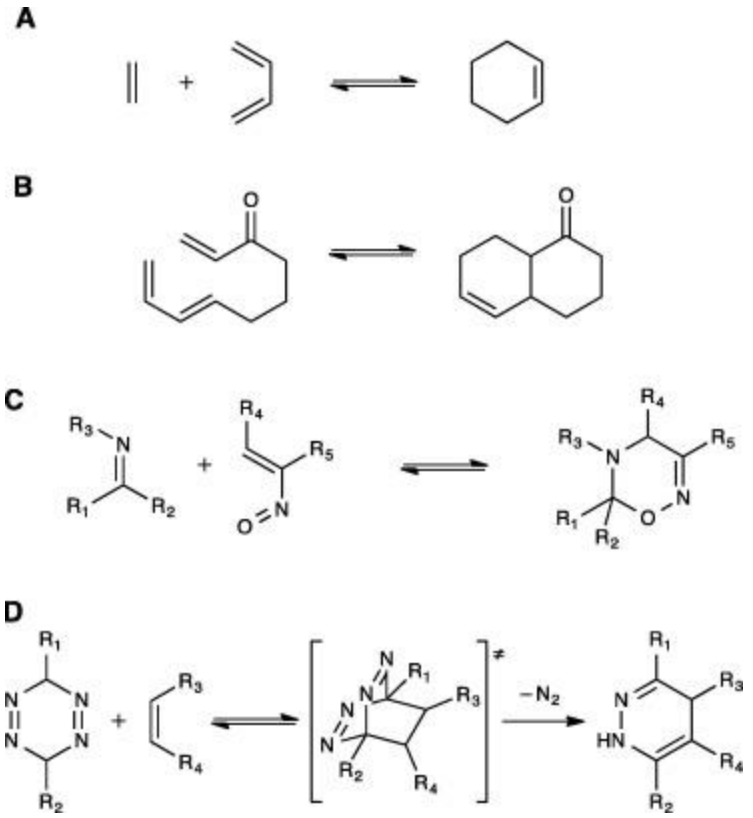

Figure 2.10. a) Normal electron-demand DA reaction, b) intramolecular DA reaction , c) hetero-DA reaction, and d) inverse electron-demand DA reaction. Reprinted from ref 48

The speed and reversibility of the DA reaction is dependent on the temperature. At low temperatures the DA adduct is dominant and the cross-linked networks are relatively stable. The unfavorable electron distribution within the reaction partners will slow the reaction. The cycloaddition reaction will be faster if the electron-poor dienophiles are reacted with electron-rich dienes (normal electron-demand DA reaction).

2.2.3 Synthetic application

DA reaction have attracted particular attention in pharmaceutical or biomedical aspect. Furan and maleimide pairs is the most reactant used in the reaction because of high availability, and can be easily functionalized with the reactive moieties under mild conditions with high chemo-selectivity. Also, it is advantageous that the DA reaction readily proceeds in water which is not toxic and cheap. Furthermore the reaction is accelerated in water due to enhanced hydrogen bonding to the activated complex and hydrophobic interactions between the reactants.[50] Moreover, there is no by-product formed because of the absence of catalyst, so the purity of the product will be high. This is especially important if macromolecules, such as polymers, dendrimers, proteins or nucleic acids, are involved in the reaction. The DA cycloaddition/cycloreversion reaction can be used to protect or deprotect functional groups,

preparation of degradable or self-healing materials, and in the design of controlled drug delivery systems. For instance, Woodward *et al.* used a Diels–Alder reaction to synthesize cortisone and cholesterol. Also the DA reaction has been utilized for the synthesis of dendrimers. The coupling between furan and maleimide was utilized to assemble symmetrical, thermally responsive dendrimers. On the other hand, it is used in the fabrication of surfaces that interact with cells. For example, de Araújo *et al.* applied DA reaction for the immobilization of streptavidin–diene conjugates on maleimide-functionalized glass surfaces.[51] Moreover the reaction is suitable for the preparation of hydrogels which can be used as space filling agents, vehicles for the delivery of drug, and scaffolds for cell delivery. For instance, Nimmo *et al.* produced a new type of vehicles for drug targeting which is furan-modified hyaluronic acid derivatives cross-linked with maleimide-functionalized PEG.[52]

2.3 LAYER-BY-LAYER ASSEMBLY

2.3.1 Introduction

For magnetic targeted drug delivery, the MNPs should possess small sizes, narrow size distributions, and high SAR values. In in vivo applications, MNPs have a higher tendency to agglomerate because of their inherent cohesion due to magnetic interactions.[53] The agglomeration leads to a reduction of the circulation time of magnetic nanoparticles in the bloodstream.[54] To overcome this challenge, the magnetic nanoparticles are coated by polyelectrolyte LBL technique in an attempt to tune physical and chemical properties. The key advantage of the LBL method is the simplicity, versatility, flexibility, and biocompatibility.[55] An increase in the shell thickness significantly reduces the polydispersity of the whole particle system, and increases the predominant repulsive interaction due to surface charges at the outside of the shell.[56] The LBL assembly technique was first developed and introduced in 1966 by Ilerat Dupont.[57] The technique did not receive much credit nor attention from the scientific community until it was pioneered in 1991 by Decher *et al.* as a solution for deposition of charged polymers.[58]

2.3.2 Assembly Concept

LBL assembly consists of the sequential adsorption of complementary multivalent molecules on a surface, occurring either via electrostatic or nonelectrostatic interactions (Figure 2.11). The LBL buildup of multilayer assemblies generally can be performed through a variety of deposition methods including dip-coating, spin-coating, spraying, and perfusion. The electrostatic interaction is one of the most important among the interactions between molecules and surfaces when both molecule and adsorbent surface are electrically charged. As a result of electrostatic interactions, we can obtain multilayer films with well-controlled composition, structure, and thickness by simply repeating the coating.

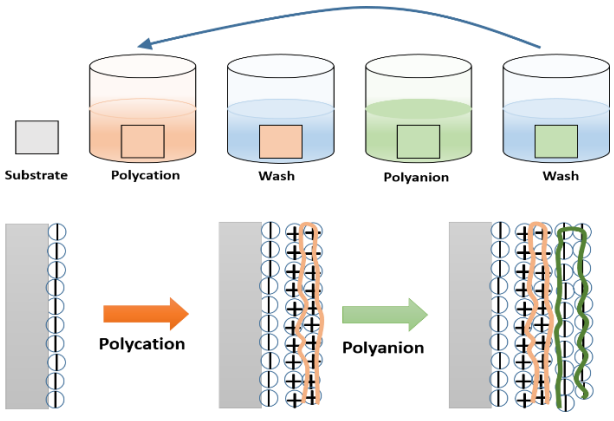

Figure 2.11. Schematic representation of the buildup of multilayer thin films via electrostatic interaction

The architecture and properties of the films deposited by this method (such as thickness, chemical composition, structure, roughness, wettability, and swelling/shrinking behavior) can be well-controlled by varying the properties of the adsorbed species such as the charge density, composition, and structure. The physicochemical properties of the liquid medium such as the salt/buffer composition, solvent quality, ionic strength, and pH also can play a role in the determination of the thickness of the layer. Moreover the external parameters such as temperature, exposure to light, mechanical stress, electrical field, adsorption time, and number of layers deposited during the assembly process affect the coating.[59]

3 EXPERIMENTAL SECTION

3.1 PART I

The CS-MNPs were synthesized by the seed-mediated growth method.[60] In the first step we synthesized $Zn_xCo_{1-x}Fe_2O_4$ nanoparticles with x varying between 0 and 0.8 as seed nanoparticles. Secondly, a $MnFe_2O_4$ shell was over-grown by thermal decomposition onto the surface of the seed particle.

3.1.1 Synthesis of $Zn_xCo_{1-x}Fe_2O_4$ nanoparticle seeds

$Zn(acac)_2$ (x mmol) , $Co(acac)_2$ (1-x mmol), and $Fe(acac)_3$ (2 mmol) were placed in a (50 mL) three-neck round-bottom in the presence of oleic acid (6 mmol), oleylamine (6 mmol), and benzyl ether (20 mL). The mixture was heated to reflux for 60 min at 300 °C, with a heating rate of 8 °C/min, under an argon atmosphere and cooled down to room temperature. Under ambient conditions, ethanol was added to the mixture resulting in black precipitate via centrifugation (4500 rpm, 10 min). The black powder was dissolved in hexane.

3.1.2 Synthesis of $Zn_xCo_{1-x}Fe_2O_4$@$MnFe_2O_4$ nanoparticles

$Mn(acac)_2$ (1 mmol), and $Fe(acac)_3$ (2 mmol) were placed in a (50 mL) three-neck round-bottom in the presence of oleic acid (6 mmol), oleylamine (6 mmol), and benzyl ether (20 mL). After the addition of the $Zn_xCo_{1-x}Fe_2O_4$ nanoparticles suspended in hexane, the mixture was first heated to 100 °C for 30 min to remove the hexane, and then heated to reflux 300 °C for 30 min under an argon atmosphere with a heating rate of 8 °C/min. After cooling, the ethanol was added to the mixture resulting in black precipitate. The obtained precipitate was dispersed in toluene after centrifugation.

3.1.3 Preparation of hydrophilic $Zn_xCo_{1-x}Fe_2O_4$@$MnFe_2O_4$ Nanoparticles

CS-MNPs were transferred from toluene to the aqueous phase by surface modification using TMAOH.[61] The nanoparticles were precipitated and centrifuged, and subsequently TMAOH/butanol (1M) solution was added. The mixture was allowed to react for 30 min under sonication. After the mixture was centrifuged, supernatant was removed and the black precipitate was washed with excess amount of hexane. The nanoparticles were dispersed in water.

3.2 PART II

The CS-MNPs ($Zn_{0.4}Co_{0.6}Fe_2O_4$@x$Zn_{0.4}Mn_{0.6}Fe_2O_4$) have been synthesized by the seed-mediated growth method, where x is the molar concentration of precursor (x=1 and x=0.5, respectively), and y is the synthesis time (y=30 and y=60 min, respectively). $Zn_{0.4}Co_{0.6}Fe_2O_4$ nanoparticles were used as seeds and $Zn_{0.4}Mn_{0.6}Fe_2O_4$ particles were over-grown by thermal decomposition onto the surface of the seed particle.

3.2.1 Synthesis of $Zn_{0.4}Co_{0.6}Fe_2O_4$ nanoparticle seeds

$Zn(acac)_2$ (0.4 mmol) , $Co(acac)_2$ (0.6 mmol), and $Fe(acac)_3$ (2 mmol) were placed in a 50 mL three-neck round-bottom in the presence of oleic acid (6 mmol), oleylamine (6 mmol), and benzyl ether (20 mL). The mixture was heated to reflux for y min at 300 °C, with a heating rate of 8 °C/min, under an argon atmosphere and cooled down to room temperature. Under ambient conditions, ethanol was added to the mixture resulting in black precipitate via centrifugation (4500 rpm, 10 min). The black powder was dissolved in hexane.

3.2.2 Synthesis of $Zn_{0.4}Co_{0.6}Fe_2O_4$@x$Zn_{0.4}Mn_{0.6}Fe_2O_4$ nanoparticles

x$Zn(acac)_2$ (0.4 mmol) , x$Mn(acac)_2$ (0.6 mmol), and x$Fe(acac)_3$ (2 mmol) were placed in a 50 mL three-neck round-bottom in the presence of oleic acid (6 mmol), oleylamine (6 mmol), and benzyl ether (20 mL). After the addition of the $Zn_{0.4}Co_{0.6}Fe_2O_4$ nanoparticles suspended in hexane, the mixture was first heated to 100 °C for 30 min to remove the hexane, and then heated to reflux 300 °C for 60 min under an argon atmosphere with a heating rate of 8 °C/min. After cooling, the ethanol was added to the mixture resulting in black precipitate. The obtained precipitate was dispersed in toluene after centrifugation.

3.3 PART III

3.3.1 Synthesis of truncated octahedron $Zn_{0.4}Co_{0.6}Fe_2O_4$@$Zn_{0.4}Mn_{0.6}Fe_2O_4$ nanoparticles

The CS-MNPs were synthesized by the same method described in section 3.2 with different experimental parameters.

3.3.2 Conjugation of DOX to $Zn_{0.4}Co_{0.6}Fe_2O_4$@$Zn_{0.4}Mn_{0.6}Fe_2O_4$ nano-carriers via thermo-responsive switch

As-synthesized magnetic nanoparticles (50 mg) were mixed with a solution of alendronic acid (100 mg alendronic acid in 25 mL water) and heated for 90 min at 90 °C. The alendronic acid in excess was removed by washing and centrifugation. 2-furfuryl isothiocyanate (100 µL) was added to solution and stirred for 20

h at 45 °C. The excess of 2-furfuryl isothiocyanate was eliminated by washing with distilled water and centrifugation for several times. Afterwards, N-(2-Carboxyethyl)maleimide **(**0.44 mmol) was added and stirred for 20 h at 45 °C. The excess of N-(2-Carboxyethyl)maleimide was removed by washing with PBS. Functionalized nanoparticles (1 mg/mL) were mixed with EDC (20 mg), NHS (20 mg), and DOX (1 mg) and stirred for 24 h at 37 °C. The DOX-loaded nanoparticles were purified by washing and centrifugation several times with distilled water and stored in a refrigerator in the dark before further experiments.

3.4 PART IV

3.4.1 Synthesis of spherical $Zn_{0.4}Co_{0.6}Fe_2O_4$@$Zn_{0.4}Mn_{0.6}Fe_2O_4$ nanoparticles

The CS-MNPs were synthesized by the same method described in section 3.2 with different experimental parameters.

3.4.2 LBL coating of core/shell magnetic nanoparticles

A standard LBL technique was used to coat the nanoparticles. CS-MNPs (2 mg/mL) was added drop-wise during 20 min to aqueous solution of PAH (4 mg/mL) under sonication. The mixture was kept under stirring in the dark and at room temperature during 12 h. The excess of PAH was removed by washing and centrifugation several times with water. Then PAH coated nanoparticles were mixed with PAA (4 mg/mL) during 20 min. The mixture was stirred for 12 h in the dark at room temperature and then purified. The given procedure was repeated until the required number of layers was reached.

3.4.3 Doxorubicin loading onto the last layer (PAA) of the coating

LBL-coated nanoparticles (1 mg/mL, pH 7) were mixed with N-(3-dimethylaminopropyl)-N'-ethylcarbodiimide hydrochloride (EDC) (10 mg) and N-Hydroxysuccinimide (NHS) (10 mg). The solution was agitated for 5 h at room temperature. The excess of EDC and NHS was removed by washing and centrifugation several times with PBS. DOX (2 mg) was added to the mixture and stirred for 24 h at 37 °C. The DOX loaded CS-MNPs were purified by washing and centrifugation several times and kept refrigerated at 4 °C in the dark before further experiments.

3.5 CHARACTERIZATION OF CORE/SHELL MAGNETIC NANOPARTICLES AND ITS FUNCTIONALIZATION

3.5.1 X-ray diffraction (XRD)

A PANanalytical X'Pert Pro MPD X-ray diffractometer was used to determine the crystalline structure of nanoparticles. The diffractograms were recorded using $Cu_{K\alpha}$ radiation (λ=1.54 Å) at room temperature with a step size of 0.02° and a count rate of 2s/step. The mean crystallite size of the nanoparticles was calculated by Scherrer´s formula from the (311) Miller plane of the diffraction pattern.

3.5.2 Transmission electron microscopy (TEM)

TEM analyses were performed on a JEOL JEM-2010 instrument with spatial resolution of 1.4 Å (lattice) and 1.94 Å (point to point).

3.5.3 X-ray photoelectron spectroscopy (XPS)

X-ray photoelectron spectroscopy (XPS) analysis was realized by means of ULVAC PHI 5000 Versa Probe II spectrometer with monochromated Al K_α (1486.7 eV) X-ray radiation. All binding energies were referenced to the carbon 1s peak at 284.6 eV. The spectra were processed with the ULVAC-PHI MultiPak software and the residual background was removed using the Shirley method.

3.5.4 Dynamic light scattering (DLS)

The hydrodynamic diameters of the samples were determined by DLS using an ALV 5000 spectrometer equipped with a Neodymium YAG-laser (λ = 532 nm) at 90° scattering angel.

3.5.5 Fourier transform infrared spectroscopy (FT-IR)

FT-IR measurements were performed on a Bruker Vertex 70 spectrometer under ambient atmosphere (20 scans at a resolution of 4 cm^{-1}) in attenuated total reflectance (ATR) mode. The IR data were processed by means of OPUS v.6.5 (Bruker) software package.

3.5.6 Thermogravimetry (TG)

TG analysis was performed on a Netzsch Iris TG 209C device. The sample was placed in an alumina crucible and heated from room temperature to 700 °C under nitrogen atmosphere with a rate of 20 °C/min.

3.5.7 Zeta potential

For Zeta potential measurements a Malvern Instruments Zetasizer 3000 HSA was used.

3.5.8 Vibrating sample magnetometery (VSM)

Room temperature magnetic measurements were done by a vibrating sample magnetometer (MicroMag 3900, Princeton Measurements Corp., U.S.A) which provides a maximum magnetic field of 1 T.

3.5.9 *In vitro* hyperthermia

Magnetic heating measurements were performed to assay the heating performance of the nano-carriers. The SAR is commonly employed to quantify the heat dissipation rate of a given ferrofluid. SAR measurements of the nanoparticles in water were carried out using two devices: Hüttinger Elektronik, model IG5, which provides an AMF at 1950 kHz and power values up to 7.2 kW; Hüttinger Elektronik, model TIG 20/300, that uses a frequency of 400 kHz and power values up to 20 kW. The ferrofluid sample with a concentration (1 mg/mL) was inserted in a water-cooled magnetic induction coil. The temperature changes during time were recorded using a computer-attached fiber optic temperature sensor (OPT OCON AG).

3.5.10 *In vitro* drug release assay

For release measurements, DOX loaded particles (10 mg) were dispersed in phoshphate buffer saline (10 mL) of pH 5 and/or 7.4. The release experiments were performed at 43 °C under HF-AMF (1950 kHz). At predetermined time intervals, the media taken out for measurement was replaced with an equal volume of fresh buffer solution. The drug release from magnetic nano-carriers was determined by fluorescence spectrometry (FP-6500 Spectrofluorometer) measuring the emission of the released DOX in the supernatant at excitation wavelength of 490 nm. The supernatant was obtained by magnetic decantation of magnetic nano-carriers.

3.5.11 Cytotoxicity assay

For the determination of cell viability the colorimetric MTT metabolic activity assay was used. HeLa cells (3×10^4 cells/well) and Hep G2 cells (1×10^4 cells/well) were cultured in a 96-well plate and incubated for 12 h in the incubator. The cells were treated with culture medium containing functionalized CS-MNPs at different concentrations (12.5–200 µg) and incubated for another 24 h. Afterwards, the cells were washed with PBS for several times to remove free functionalized CS-MNPs. Cytotoxicity of CS-MNPs was further determined by MTT assay. MTT solution (1:10 dilution; 1 mL of MMT stock solution with 9 mL medium) was added to each well and incubated for 2 h. After the supernatant was removed, dimethyl sulfoxide (80 µl) was added to dissolve the formazan crystals. The absorbance spectrum of each well was measured at 550 nm excitation wavelength by spectrophotometry. The relative cell viability (%) was expressed with respect to the negative control wells.

4 RESULTS AND DISCUSSIONS

The results obtained in this work are presented in this chapter. Four parts are included: the effect of Zn substitution on the structural and magnetic properties of $Zn_xCo_{1-x}Fe_2O_4@MnFe_2O_4$ in part I; the effect of experimental parameters on the magnetic properties of $Zn_{0.4}Co_{0.6}Fe_2O_4@Zn_{0.4}Mn_{0.6}Fe_2O_4$ in part II; The third and fourth part of this thesis explain specific examples in which the concepts of part I & II were used to design magnetic drug targeting system for synergistic anticancer therapy. Part III concern about on-command controlled drug release by Diels-Alder reaction using bi-magnetic core/shell nano-carriers; and On-Off switch controlled doxorubicin release from thermo- and pH-responsive coated bi-magnetic nano-carriers in part IV.

4.1 PART I

The section deals with preparation of core/shell $Zn_xCo_{1-x}Fe_2O_4@MnFe_2O_4$ nanoparticles via seed mediated growth, and attempts to investigate the influence of Zn^{+2} substitution on the structure and magnetic properties of CS-MNPs, which can enhance SAR for hyperthermia application.

Thermal decomposition of $Fe(acac)_3$ and controlled consecutive reduction of $Zn(acac)_2$ and $Co(acac)_2$ or $Mn(acac)_2$ with oleic acid and oleylamine at high temperature yield monodisperse core/shell $Zn_xCo_{1-x}Fe_2O_4@MnFe_2O_4$ nanoparticles, which can be easily precipitated from the solution by adding ethanol. The success of forming monodisperse nanoparticles is because of directly slow heating to reflux at 298 °C with heating rate 8 °C/min in benzyl ether.

4.1.1 Effect of Zn substitution on the structural properties of magnetic nanoparticles

The nominal molar compositions of the prepared samples were $CoFe_2O_4@MnFe_2O_4$, $Zn_{0.2}Co_{0.8}Fe_2O_4@MnFe_2O_4$, $Zn_{0.4}Co_{0.6}Fe_2O_4@MnFe_2O_4$, $Zn_{0.6}Co_{0.4}Fe_2O_4@MnFe_2O_4$, and $Zn_{0.8}Co_{0.2}Fe_2O_4@MnFe_2O_4$ for S1, S2, S3, S4 and S5 samples, respectively.

The XRD patterns clearly show that all samples have a cubic spinel structure and are shown in figure 4.1. There is a shift in 2θ towards lower angles with increasing Zn substitution, revealing an increase in the lattice parameters of the samples. The crystallite sizes for these samples are 8.2 ± 0.5 nm (S1), 9.3± 0.4 nm (S2), 10.1 ± 0.2 nm (S3), 11 ± 0.3 nm (S4), and 12.2± 0.4 nm (S5).

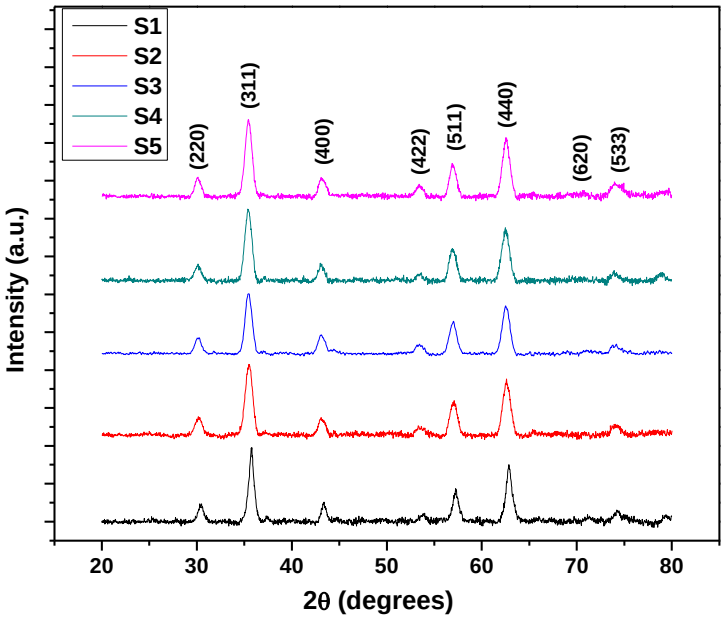

Figure 4.1. XRD patterns of different nanopowders

The XRD patterns of the samples are refined using the Rietveld profile fitting technique. The refinement is carried out by using the PANalytical X'Pert HighScore program and assuming a cubic structure with the Fd3m space group (figure 4.2a). Figure 4.2b shows that the lattice parameter increases from 8.36 Å to 8.394 Å with increasing Zn concentration. This could be related to the change in the ionic size of zinc. When Zn2p is substituted, it prefers the A site [62] and an increase in the lattice parameter is expected as the larger Zn2p (0.74 Å) ions replace the Co2p ions (0.65Å) [63] and lead to an expansion of the structure and, consequently, to an increase of the lattice parameter.

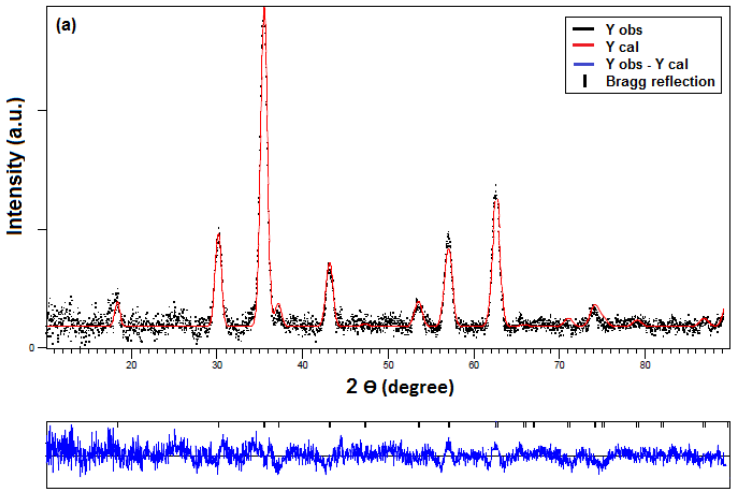

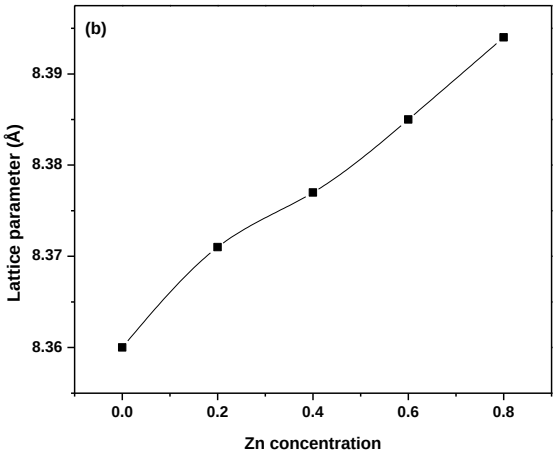

Figure 4.2. a) A typical XRD pattern with Rietveld analysis of S2, b) Variation of the lattice parameter (Å) of the samples with Zn concentration.

The properties of magnetic nanoparticles are expected to be dependent critically on the morphology of the samples. The morphology of the samples was determined by TEM. The mean size of the CS-MNPs have been evaluated by TEM images (Figure 4.3a–e) and confirmed by DF-TEM (Figure 4.3f). The mean average size of the core/shell systems was calculated as 9± 0.5 nm (S1), 10.7 ± 0.4 nm (S2), 11.5 ± 0.6 nm (S3), 12 ± 0.3 nm (S4), and 13.2 ± 0.7 nm (S4). The crystallite size from XRD results comparable with the average particles size determined from TEM images, indicate that the nanoparticles have high crystallinity. The morphology of S3 is different from other samples, which is more related to cubic shape, while the shape of other samples is spherical to truncated octahedron. Thus it will affect the magnetic properties of the samples.

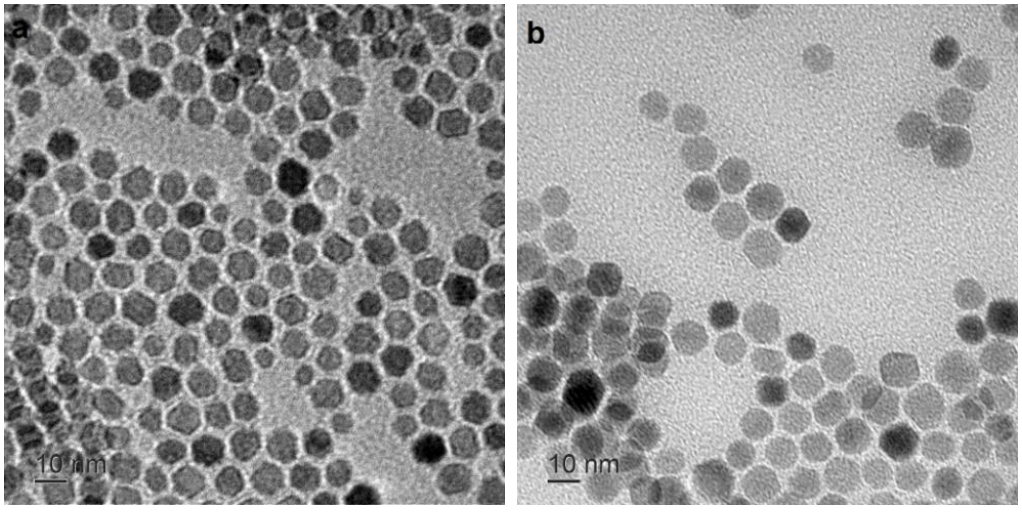

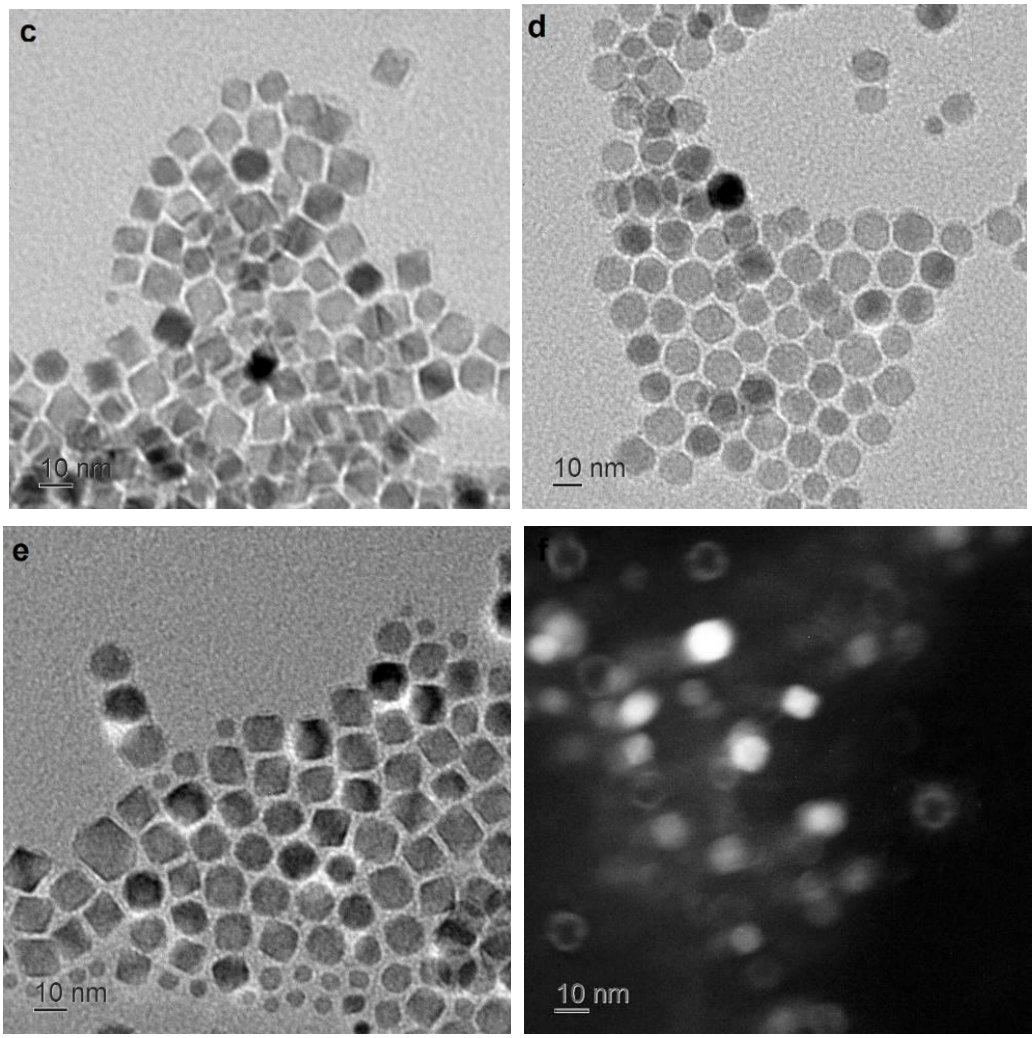

Figure 4.3. TEM images of: a) S1; b) S2; c) S3; d) S4; e) S4 and e) DF- TEM image of S2.

XPS measurements were performed to investigate the valence change of the cations and chemical composition of the samples (figure 4.4a). The XPS analysis indicated that all samples are composed of Fe, Co, Mn, and O. Moreover, sample S2-S5 contain of Zn. Figure 4.4b-f displays XPS deconvolution spectra of S3.

The XPS spectrum of Co2p exhibits two peaks located at binding energies (BE) of 781 and 796.4 eV, which can be attributed to $Co2p_{3/2}$ and $Co2p_{1/2}$, respectively (Figure 4.4b); they are accompanied with corresponding shake ups peaks at 786.5 and 802.7 eV, respectively, indicates Co^{+2} occupy the octahedral sites in the CS-MNPs spinel lattice.[64] In the Mn2p spectrum (Figure 4.4c), the dominant peak $Mn2p_{3/2}$ is at 642.2 eV and the other peak $Mn2p_{1/2}$ is at 653.8 eV, providing a clear evidence for Mn^{2+} chemical state on the sample surface.[65] The $Mn2p_{3/2}$ spectra have peaks located at 640.4, 642.4, and 646.6 eV, which is

in good agreement with the value reported for the Mn^{2+}, Mn^{4+}, and its satellite, respectively.[66] The Fe2p spectra show the two main peak with binding energies of the $Fe2p_{3/2}$ and $Fe2p_{1/2}$ core levels located at 711.2 and 724.3 eV, respectively (Figure 4.4d), with corresponding satellite peaks for $Fe2p_{3/2}$ and $Fe2p_{1/2}$ visible at binding energies of around 719.2 and 731.0 eV, which is consistent with that reported for Fe^{3+} cations.[67] In principle, the satellite peak with the main peaks appears due to two final states caused by photoemission of the Fe site of the oxide. The peak with the binding energy of 711.2 eV is attributed to the Fe^{3+} cation located at the octahedral sites in the spinel structure. The binding energies of the $Zn2p_{3/2}$ and $Zn2p_{1/2}$ core level peaks are 1021.4 and 1044 eV, respectively, confirming the presence of Zn^{2+} cation (Figure 4.4e). The peak at 1021.3 eV is ascribed to Zn^{2+} cations occupying tetrahedral site in CS-MNPs.[68] The O1s peak is deconvoluted into two contributions at 530 and 531 eV, which are attributed to the crystal lattice oxygen and surface-adsorbed oxygen, respectively (Figure 4.4f).

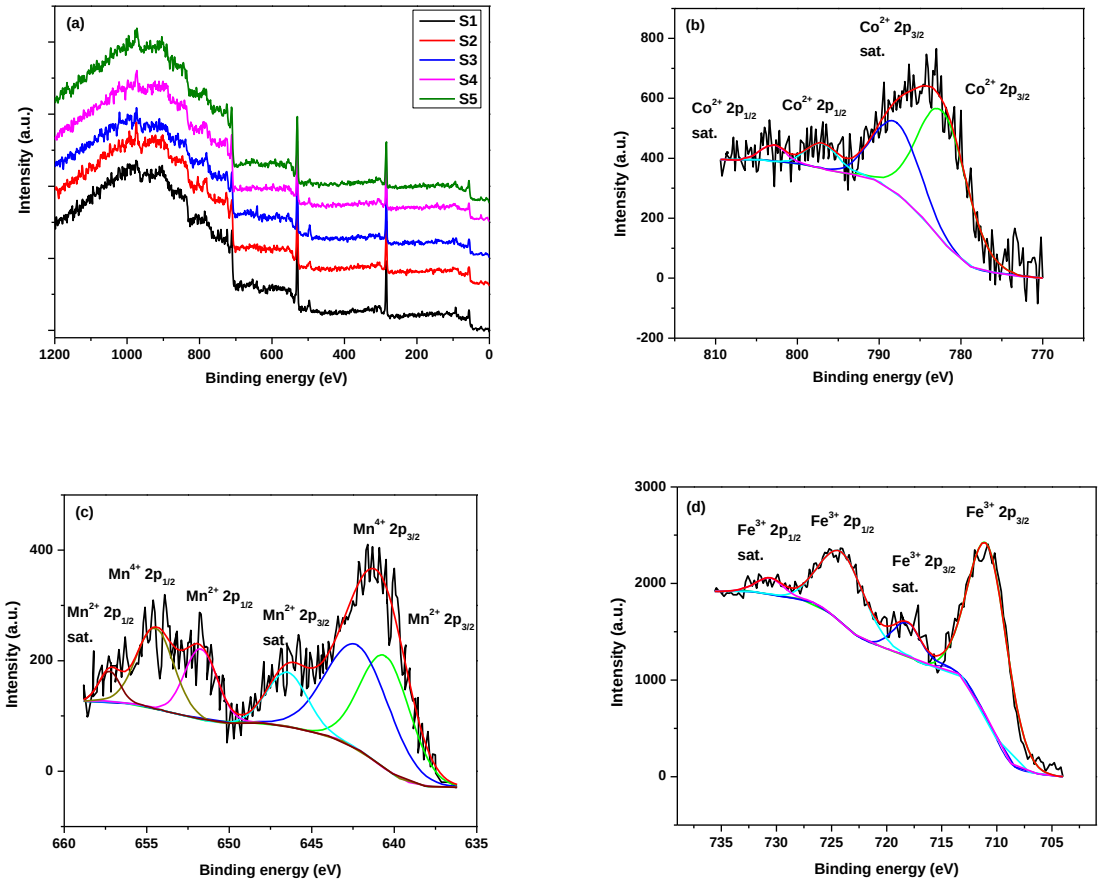

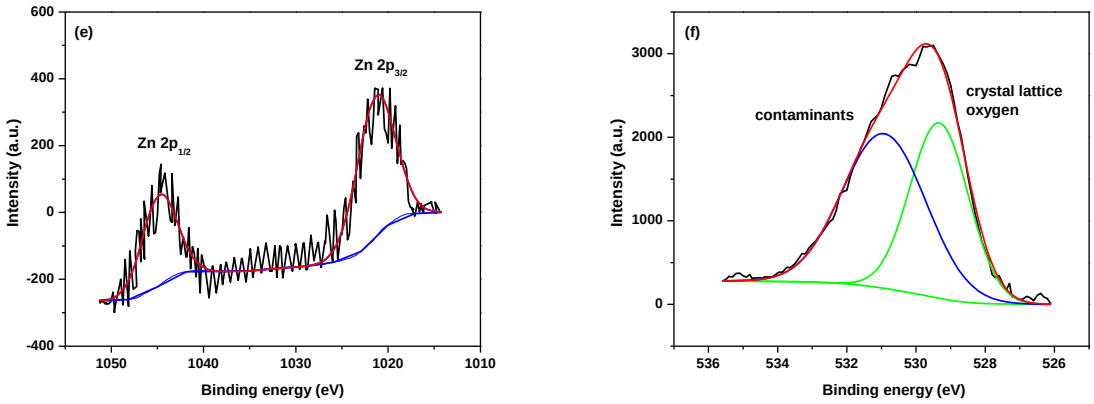

Figure 4.4. a) XPS spectra of CS-MNPs samples. Fitted photoelectron peaks of: b) Co2p1/2 and Co2p3/2; c) Mn2p1/2and Mn2p3/2; d) Fe2p1/2 and Fe2p3/2; e) Zn2p1/2 and Zn2p3/2; f) O1s.

4.1.2 Effect of Zn substitution on the magnetic properties of magnetic nanoparticles

The effects of Zn substitution on the M_s, M_r, and H_c of the samples are listed in Table 4.1 and it shows the variation of M_r and H_c, which decreases with the increase in zinc substitution.

Table 4.1. Comparison of magnetic properties of different samples

Sample	M_s (emu/g)	M_r (emu/g)	Coercivity (Oe)
S1	44.9	0.72	222
S2	54.3	0.3	15.4
S3	61.5	0.25	6.3
S4	51.5	0.21	4.3
S5	47.1	0.17	2.2

The magnetic measurements of the samples are shown in Figure 4.5. The magnetization curves display a superparamagnetic behavior of the systems that could be explained by the small-size effect of the nanoparticles. For low substituted (x= 0, 0.2, 0.4) zinc, M_s increased from 44.9 to 61.5 emu/g and decreased thereafter to a value 47.1 emu/g when x was increased further to 0.8.

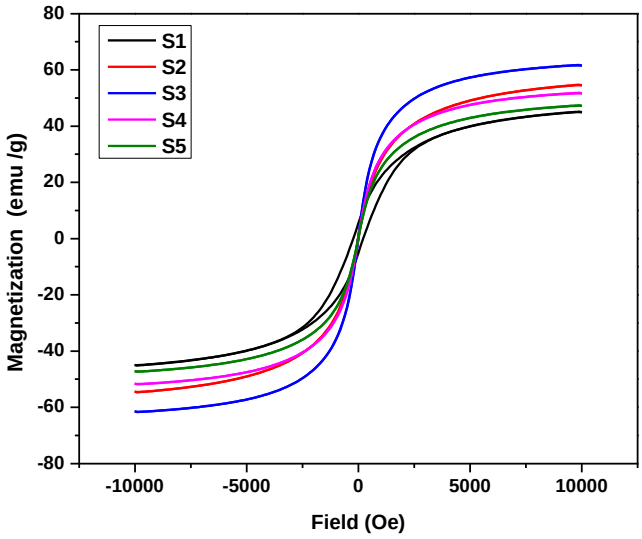

Figure 4.5. Magnetic hysteresis loop of the different nanopowders

The variation of M_s is due to the cation distribution between the tetrahedral (A) and octahedral sites (B) of cations. The increase in M_s can be explained by the fact that, when a small amount of Zn2p is substitutes Co2p, it has a strong preference to occupy the tetrahedral sites.[69] Consequently, it displaces Fe3p ions from the tetrahedral sites to the octahedral sites. This induces the partial removal of antiferromagnetic coupling interactions between Fe^{3+} ions in the tetrahedral sites and the octahedral sites,[70] which can increase the magnetization of the samples based on the Neel's collinear two-sub-lattice model.[71]

Further increase in the Zn substitution with x from 0.4 to 0.8 resultes in a decrease in M_s from 76.78 to 64.89 emu/ g. This decrease of M_s can be explained on the basis of the three sub-lattice model suggested by Yafet-Kittle model.[72] The triangular spin arrangement on B-sites is favorable, which decrease the A-B interaction and increase of B-B interaction. As a result of this phenomena, the antiferromagnetic coupling interactions between Fe^{3+} ions in each octahedral site are dominant which decreases the M_s.

The shape anisotropy plays a key role in determining the magnetic properties of nanoparticles. For the particle with large surface to volume ratio, the surface contributions to the magnetic properties become important, thus the surface anisotropy (K_s) associated with the shape becomes significant where surface anisotropy is created from the different spin direction between core and surface.[73] Therefore, cube shape (S4), having a smaller surface anisotropy, hence reduced spin disordering is advantageous to attain a larger M_s compared to a spheres.

Figure 4.6a shows the temperature versus time, measured at 1980 kHz frequency and in a power of 1592 W, for all samples. The maximum temperature change exceeding 320 K was observed for S3, whereas the samples with higher or lower Zn content demonstrated lower heating.

The investigation of the hyperthermic efficiency of the CS-MNPs was performed by evaluating the SAR. The SAR values were estimated from the initial slope of the temperature versus time curves (*dT/dt*). The efficiency of heating for a magnetic fluid is described by the SAR.[74]

$$\mathrm{SAR} = \frac{c}{m} \times \frac{dT}{dt} \tag{4.1}$$

where *C* is the specific heat capacity of the medium, and *m* is the mass of the sample.

Figure 4.6b present the variation of SAR with power of different Zn-substituted CS-MNPs at high frequency (1950 kHz). The graph shows that the S1 provides a low SAR, while a sizeable value is measured once the samples are doped with a small amount of Zn ions (S2). Interestingly, the SAR further increases with increase in the amount of doping, reaches a maximum for S3, but it drops down for S5. The SAR value of S3 is twice SAR value of the core ($Zn_{0.4}Co_{0.6}Fe_2O_4$), indicating that the magnetic nanoparticles are interfacial exchange coupled between hard and soft magnetic phases.

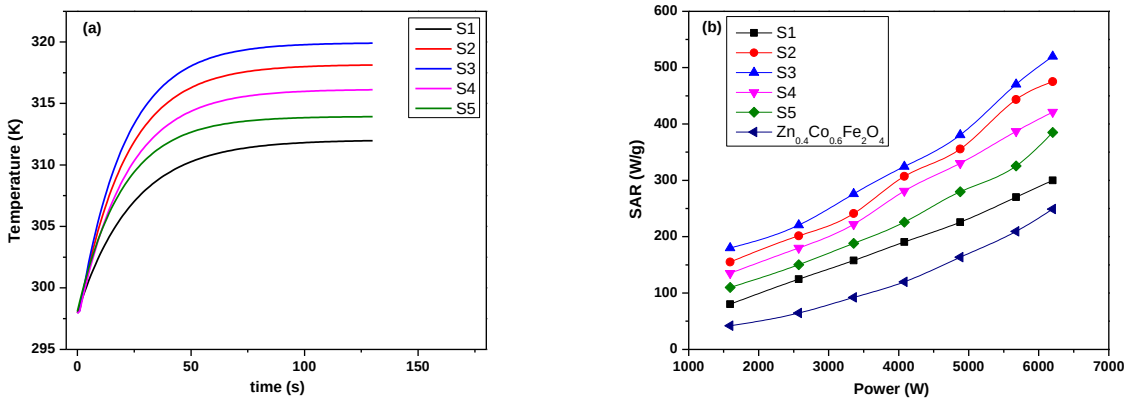

Figure 4.6. a) Heating process of different samples, b) The SAR functions for the frequency (1955 kHz) of samples.

The heating power depends not only on the parameters of the external applied field H_0 and the frequency f, but also on the magnetization of the material, and on the characteristic time of the magnetization reversal. The power loss density (W/m^3) due to Neel relaxation and Brownian relaxation is expressed as [33].

$$SAR\ \alpha\ f H_0 M_s^2 V \left(\frac{2\pi f\tau}{1+(2\pi f\tau)^2}\right) \quad (4.2)$$

For small nanoparticles in the single-domain or superparamagnetic range, heating arises from the Néel and Brownian relaxation. Néel relaxation dominates when the nanoparticles are less than 20 nm.[75] This further implies that the Brownian relaxation in the samples does not contribute to the heat dissipation mechanism, therefore assuming the control of the hyperthermic effect independently of any external parameter. Tuning the magnetic properties of nanoparticles through the control of their nanostructure will contribute to the development to optimized agents for hyperthermia. The fast inductive heat generation of nanoparticles increases the efficacy of cell death hyperthermia and reduces the toxicity during therapy.

4.2 PART II

In this part we focused on chemical synthesis of truncated octahedron CS-MNPs in order to improve their SAR. We investigated microstructural and magnetic properties of CS-MNPs system with hard core ($Zn_{0.4}Co_{0.6}Fe_2O_4$) and tunable thickness of soft shell ($Zn_{0.4}Mn_{0.6}Fe_2O_4$). The thickness of the shell is tuned by varying the concentration of the precursor, while the shape and the size of the core are controlled by the time of reaction. We demonstrated an increase of SAR of CS-MNPs compared with the magnetic core, indicating that the core and the shell are effectively exchange coupled. As a result, the magnetic properties, such as SAR and M_s of these CS-MNPs could be controlled by tuning the core/shell physical parameters and chemical compositions.

4.2.1 Effect of experimental parameters on the structural properties of magnetic nanoparticles

Four CS-MNPs samples were synthesized using seed mediated growth. Two samples have the same core diameter (7 nm), but different shell thicknesses of 2±0.3 nm (Sample S1) and 1±0.1 nm (Sample S2) respectively. Other two samples have the core diameter of 5 nm and shell thicknesses of 2±0.2 nm (Sample S3) and 1±0.1 nm (Sample S4), respectively. The mean size of the CS-MNPs and the thickness of the shell have been evaluated by TEM images (Figure 4.7a–d) and confirmed by DF-TEM (Figure 4.7e). The mean average size of core/shell systems was calculated as 9.3± 0.5 nm (S1), 8.1 ± 0.5 nm (S2), 7.0 ± 0.6 nm (S3), and 6.2 ± 0.4 nm (S4).

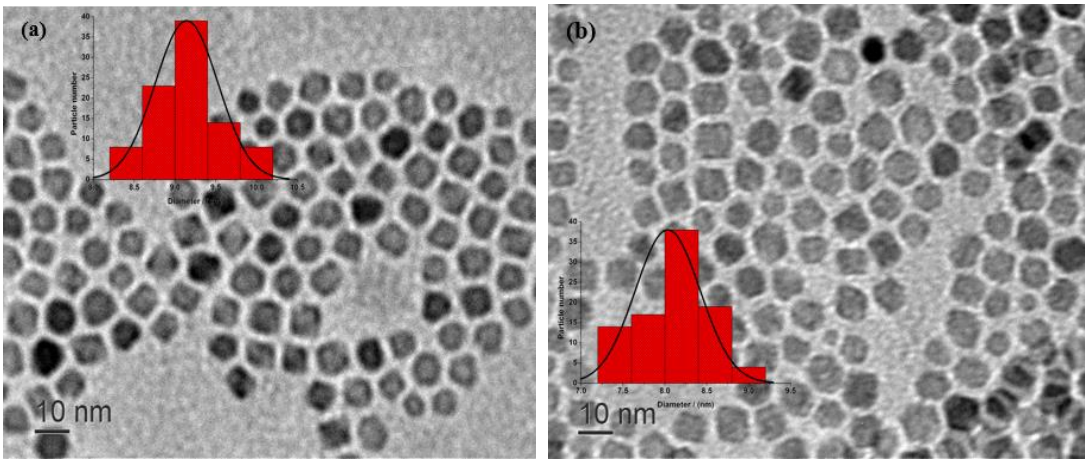

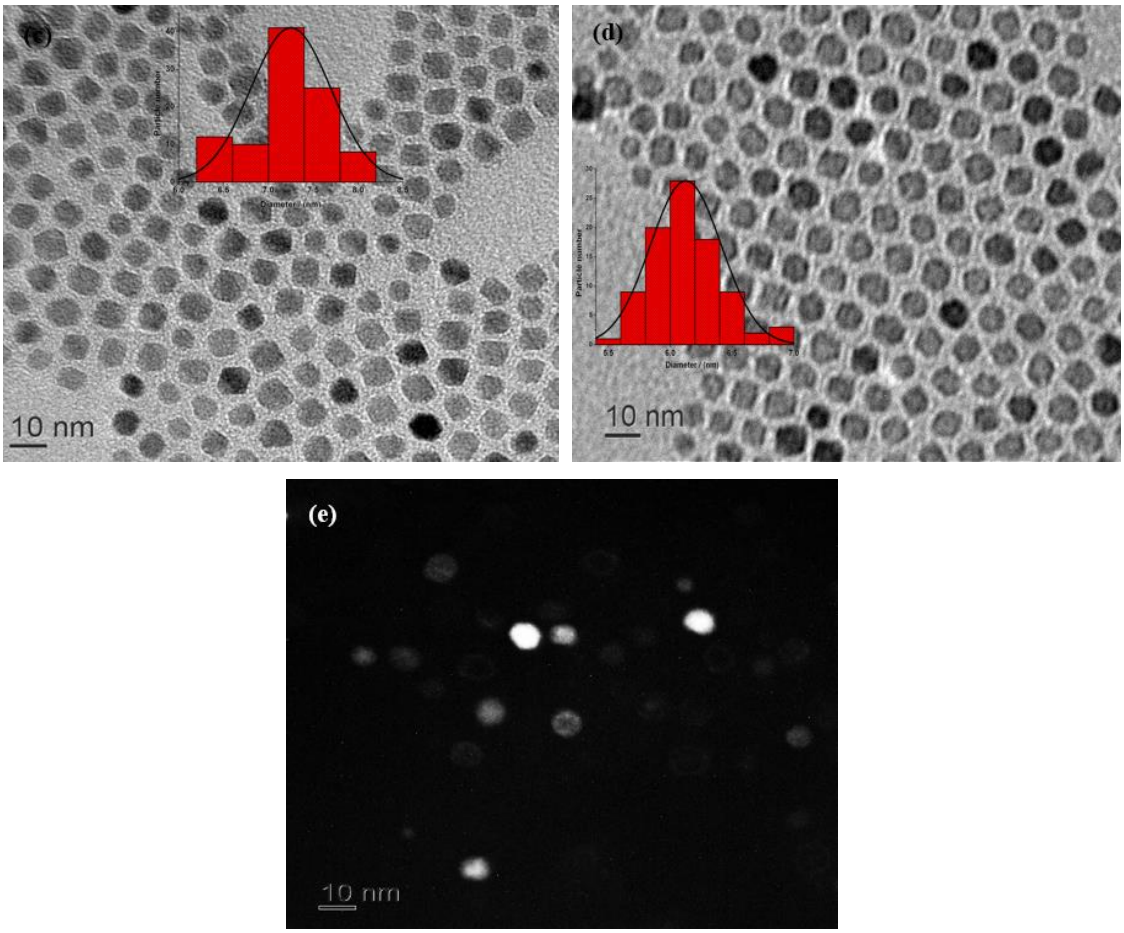

Figure 4.7. TEM images of: a) S1; b) S2; c) S3; d) S4 and e) DF- TEM image of S1.

Figure 4.8a shows the XRD patterns of all samples. The XRD pattern and the Rietveld profile refinement of S1, using the PANalytical X'Pert HighScore program are shown in Figure 4.8b. Based on these result the Bragg reflections of all samples match the reported values for the face-centered cubic structure with the space group Fd3m (Powder Diffraction Files, card no 22-1086 and no.89-1009). No evidence of impurity phases was detected. The mean crystallite size for all samples are 8.2 ± 0.5 nm (S1), 7.3± 0.4 nm (S2), 6.2 ± 0.3 nm (S3), and 5.4± 0.3 nm (S4). We note an increase of the mean crystallite size with the increasing of the concentration of the precursor and the reaction time.

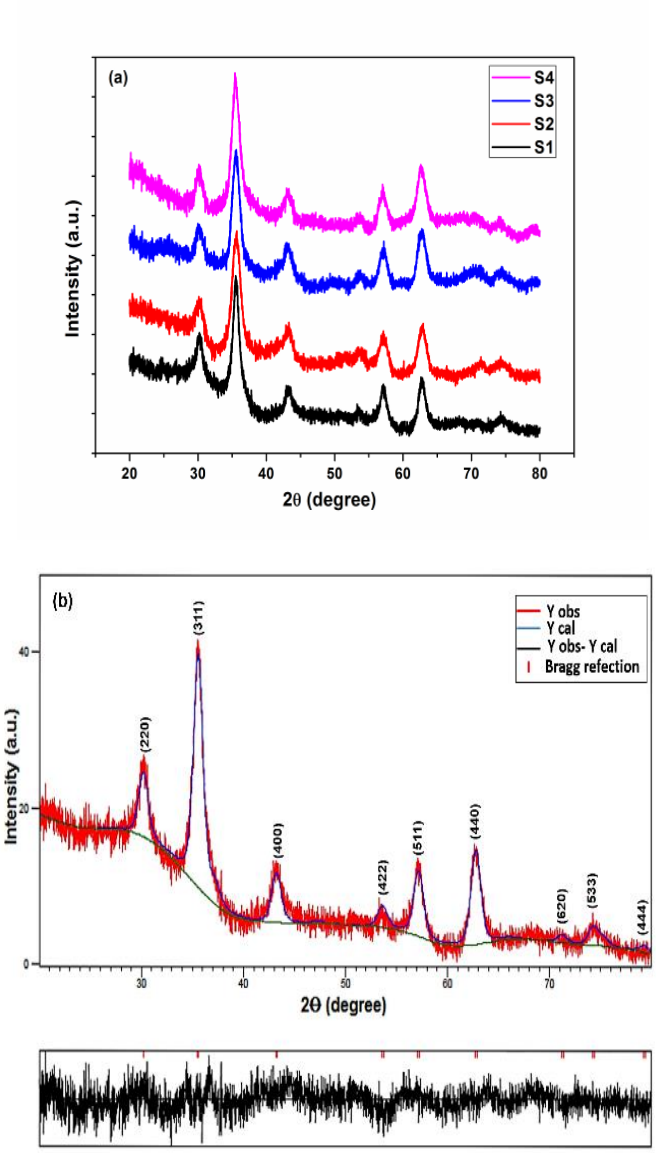

Figure 4.8. X-ray diffraction patterns of different nanopowders. b) a typical XRD pattern

Figure 4.9 exhibits that the lattice parameter of the samples and it increased from 8.371 Å to 8.394 Å. This could be related to the variation of particle size versus the concentration of the precursor and the reaction time.

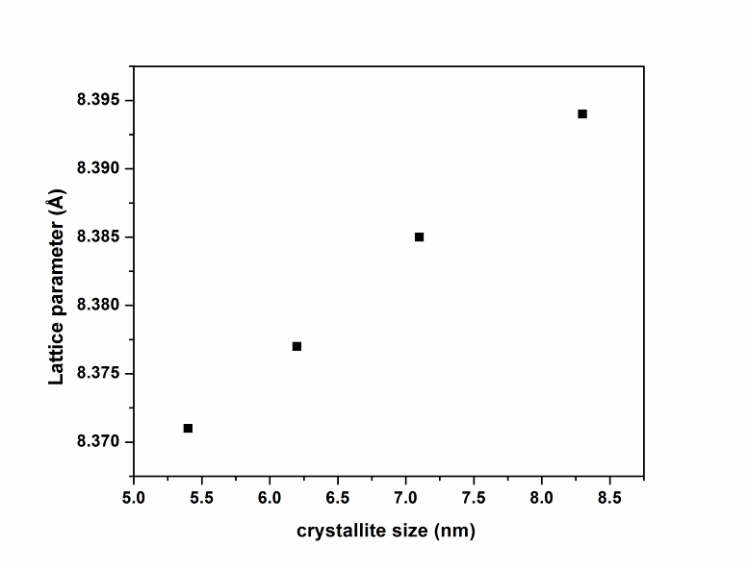

Figure 4.9. The lattice parameter (Å) of the samples

To verify the composition of the $Zn_{0.4}Co_{0.6}Fe_2O_4$@$Zn_{0.4}Mn_{0.6}Fe_2O_4$ nanopowders, XPS analysis was applied to investigate the binding energy of surface atoms present in the samples. The XPS analysis indicated that all samples are composed of Fe, Co, Mn, Zn, and O (Figure 4.10a).

The XPS spectrum of Co2p recorded from sample S1 are characterized by binding energies of the $Co2p_{3/2}$ and $Co2p_{1/2}$ core levels of 781 and 796.4 eV, respectively, with corresponding shake ups peaks at 786.5 and 802.7 eV, respectively (Figure 4.10b). This confirms that the Co^{2+} cations occupy the octahedral sites in the CS-MNPs spinel lattice. From the Mn2p spectrum, it was found that the peak at 640.4 eV is from $Mn2p_{3/2}$, with a satellite peak at 646.6, while the peak at 652.3 eV is caused by $Mn2p_{1/2}$ with a satellite peak at 657.8 eV (Figure 4.10c). This result provides a clear evidence for Mn^{2+} chemical state on the sample surface. The Fe2p spectra show the two main peaks with binding energies of 711.2 and 724.3 eV which were respectively assigned to $Fe2p_{3/2}$ and $Fe2p_{1/2}$, and accompanied by two satellite peaks at binding energies of 719.2 and 731.0 eV (Figure 4.10d), which is indicative of the presence of Fe^{3+} cations The binding energies of the $Zn2p_{3/2}$ and $Zn2p_{1/2}$ core level peaks are 1021.4 and 1044 eV (Figure 4.10e), respectively confirming the presence of Zn^{2+} cations in tetrahedral site. The O1s peak is fitted to two peaks at 530 and 531 eV (Figure 4.10f), which are ascribed to the featured of the crystal lattice oxygen and surface-adsorbed oxygen, respectively.

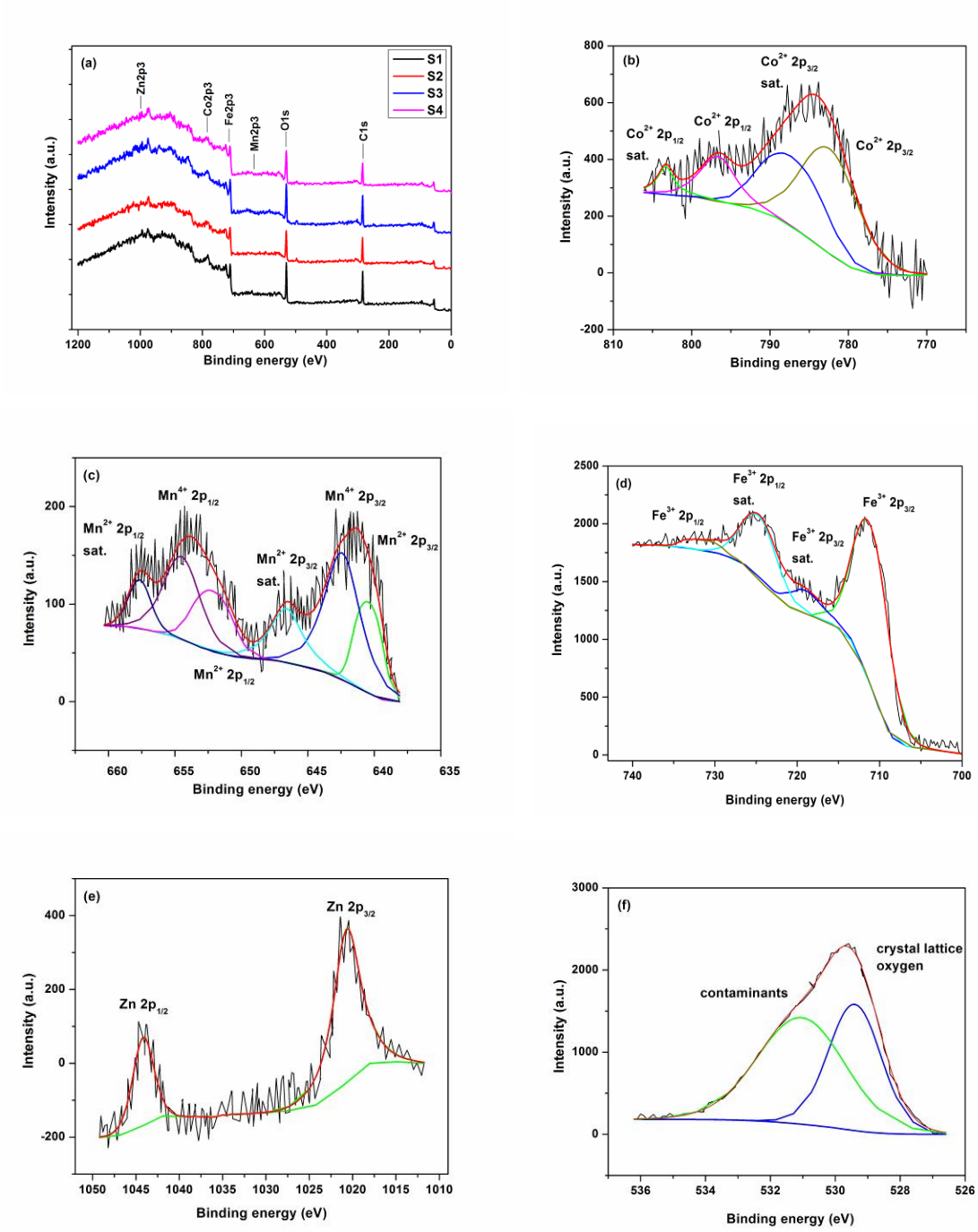

Figure 4.10. a) XPS spectra of different samples. Fitted photoelectron peaks of: b) Co2p1/2 and Co2p3/2; c) Mn2p1/2and Mn2p3/2; d) Fe2p1/2 and Fe2p3/2; e) Zn2p1/2 and Zn2p3/2; f) O1s.

All samples were studied with EDX analysis to examine the elemental composition of the particles. Figure 4.11a shows the EDX analysis of S1. The peaks assigned to Fe, Co, Mn, Zn, C and O elements can be clearly observed. Figure 4.11b shows the variation of cobalt and manganese in different samples, which confirms that the amount of cobalt and manganese in the samples is increasing with increasing the concentration of precursor and the reaction time.

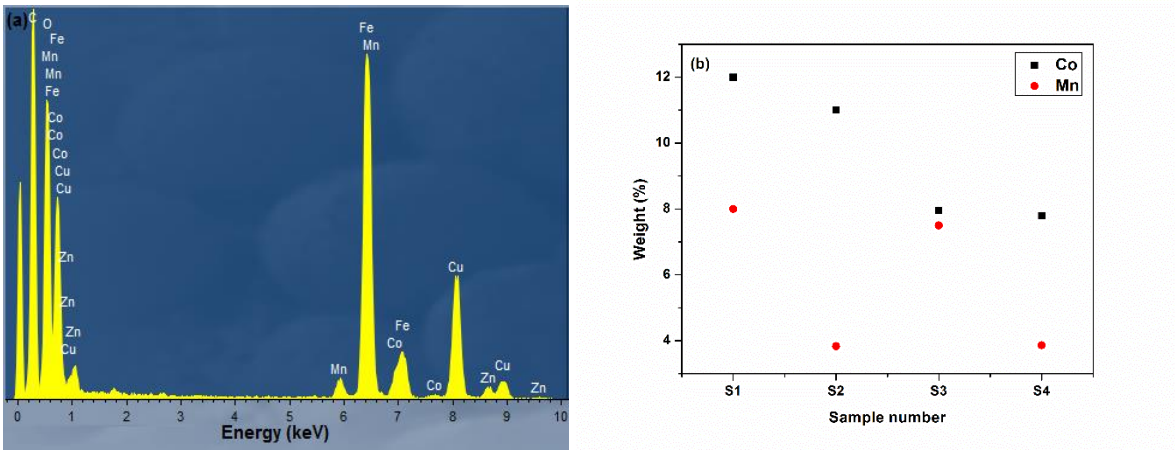

Figure 4.11. a) The typical EDX analysis of S1. b) The variation of Co and Mn in the samples.

4.2.2 Effect of experimental parameters on the magnetic properties of magnetic nanoparticles

Figure 4.12a shows the temperature versus time, measured at 1980 kHz frequency and in a power of 2574 W, for all samples are investigated. It can be seen that the S4 show a higher heating process after 80 sec, which go towards lower temperature with the core; 316 K for S1, 314.4 K for S2, 312.5 for S3, 310.4 K for S4, 306.3 K for core (7 nm), and 304.7 K for core (5nm).

Several methods of T_c determination are hardly applicable to ferrofluids: magnetization measurements are not possible at temperatures above the boiling point of the dispersion medium (e.g. water); optical methods suffer from the extremely high optical absorption and are restricted only for strong diluted magnetic colloids.

Using a calorimetric measurement technique we found a clear correlation between the temperature dependence of the magnetization of the ferrites and the energy absorption in an AMF. As we are limited to temperatures below the boiling point of the carrier liquid, we applied an extrapolation method to calculate the energy absorption up to the T_c of the nanoparticles. In this way we obtained an estimate of

the T_c of the magnetic nanoparticles in dispersion. As novelty, this determination of the Curie point is completely based on measurements made in the colloidal dispersion.

Under the ideal condition of non-interacting, monodisperse particles, the fitting functions for (dT/dt) versus T for both the heating and the cooling process is often referred as to the T_c.[76]

As a result, by using a linear extrapolation for the cooling and heating branches, we expect to have T_c as the intersection point of temperature change over time with temperature (Figure 4.12c), and yields 394 K, 378 K, 368 K, and 360 K for samples S1, S2, S3, and S4, respectively. The decrease of T_c with the decrease in particle size in the present case is attributed to the fluctuations of the electron spins become more prominent in the smaller size of particles.[77] The dependence of the T_c on size confirmed by most of studies.[78]

Since the calorimetric measurements have been made at low temperatures we avoided undesired effects like particle growth, inhomogeneous radiative heat transfer and phase conversion to another ferromagnetic phase. Also, we have the advantages of short time measurements, accurate temperature uniformity, high power measurements and direct determination of the losses. The method allows for an accurate measurement of the temperature absorption of magnetic fluids in high frequency magnetic fields, a feature which is of outstanding importance for biomedical applications.

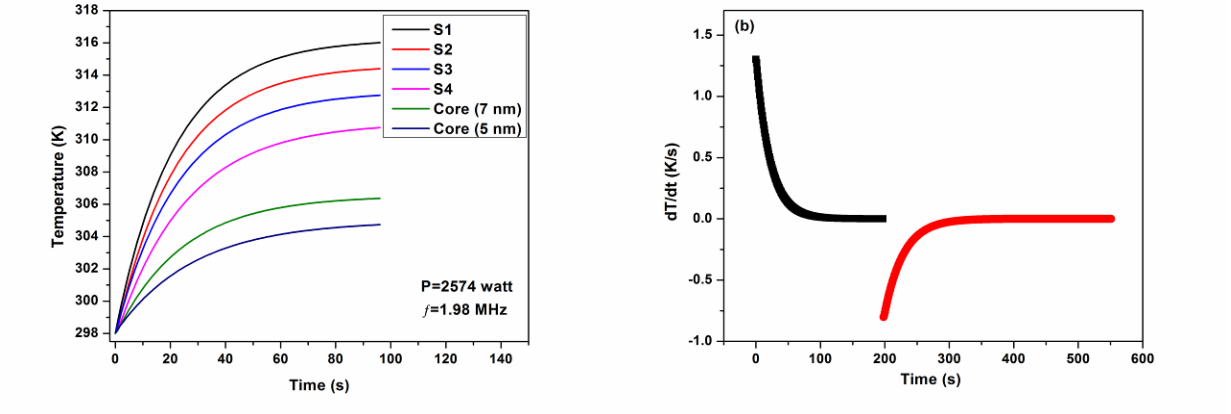

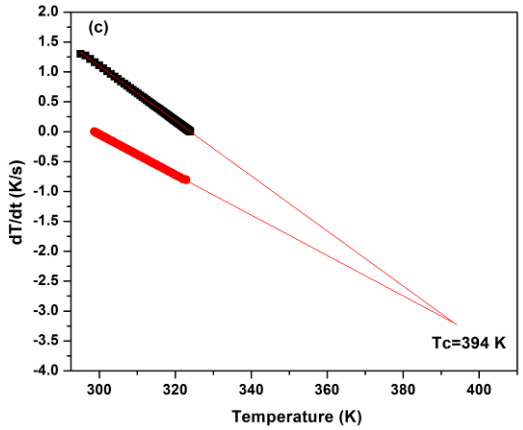

Figure 4.12. a) Heating process of different samples. b) Temperature variation rate in unit time (dT/dt) with exposure time of S1. c) Temperature change rate in unit time (dT/dt) versus time of S1.

Figure 4.13 shows the room temperature field dependent magnetization curves for different size of $Zn_{0.4}Co_{0.6}Fe_2O_4$@$Zn_{0.4}Mn_{0.6}Fe_2O_4$ (6–10 nm). The magnetization curve of CS-MNPs in powder form was measured at 300 K in external magnetic fields from -1 T to 1 T. All samples show superparamagnetic properties with low H_c values as well as remanence magnetization. We find M_s shows an increasing trend with the increasing of the size of CS-MNPs as seen in table 4.2. The 1 T magnetization at 300 K decreases from 59.6 emu/g for the S1 particles to 42.8 emu/g for the S4 particles. The magnetization curves of all samples display a superparamagnetic behavior that could be assigned to the small-size effect of the nanoparticles, which is important in biomedical applications whereas the nanoparticles aggregation or cluster formation should be avoided.

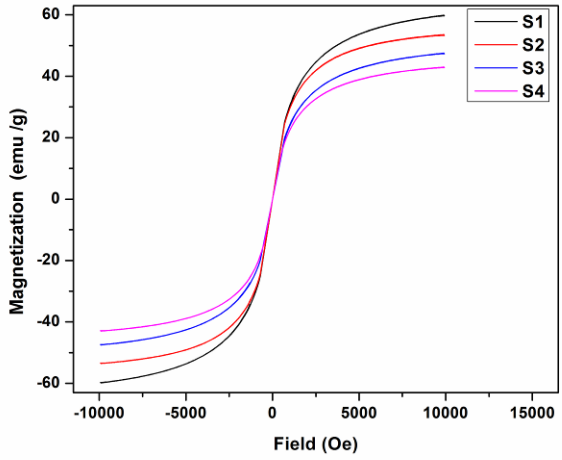

Figure 4.13. Magnetic hysteresis loop of the different sizes $Zn_{0.4}Co_{0.6}Fe_2O_4$@$Zn_{0.4}Mn_{0.6}Fe_2O_4$ nanopowders

Table 4.2. Comparison of magnetic properties of different size $Zn_{0.4}Co_{0.6}Fe_2O_4$@$Zn_{0.4}Mn_{0.6}Fe_2O_4$

Sample	M_s (emu/g)	M_r (emu/g)	H_c (Oe)	T_c (K)
S1	59.6	0.2	4.2	394
S2	53.3	0.1	2.4	378
S3	47.3	0.17	3.6	368
S4	42.8	0.21	3.4	360

CS-MNPs possess a disordered spin layer at their surfaces, and when the size of the nanoparticle is small, the ratio of disordered layer to the radius of the CS-MNPs is significant. Surface spin disorder thus leads to reduced M_s for smaller nanoparticles as defined here:[79]

$$\boldsymbol{M_s = M_{sb}\left[\frac{r-d}{r}\right]^3} \tag{4.3}$$

Where r is the radius, d is the thickness of the MNPs surface exhibiting disordered spins, and M_{sb} is the bulk M_s. We emphasize that the reduced M_s values arise from the spin-disorder effect.

The efficiency of heating for a magnetic fluid is described by the SAR (equation 4.1). The SAR values that arise from the relaxation processes are roughly proportional to the M_s and magnetocrystalline anisotropy constant (K), and are inversely proportional to the size distribution of the nanoparticles.[80]

Figure 4.14 present the variation of SAR with power of different size of $Zn_{0.4}Co_{0.6}Fe_2O_4$@$Zn_{0.4}Mn_{0.6}Fe_2O_4$ at two frequencies (1950, 450 kHz). The graphic shows a linear variation of SAR with power. The SAR values of all the samples show an increase with an increase in size of CS-MNPs. In addition to this, however the samples (S3 and the core) have the same size, the observed SAR values for S3 are found to be higher as compared to that of the single-component magnetic nanoparticles. This clearly indicates that the obtained $Zn_{0.4}Co_{0.6}Fe_2O_4$@$Zn_{0.4}Mn_{0.6}Fe_2O_4$ nanoparticles are magnetically exchange-coupled.

In the case of 9 nm S1 nanoparticles the maximum 521 W/g SAR value was obtained, whereas for the 6 nm S4 particles the values didn't exceed 340 W/g at an AC field of 5677 W (Figure 4.14a). We observe here that the magnitude of the SAR value increases as the particle size increased and the frequency decreased (Figure 4.14b).

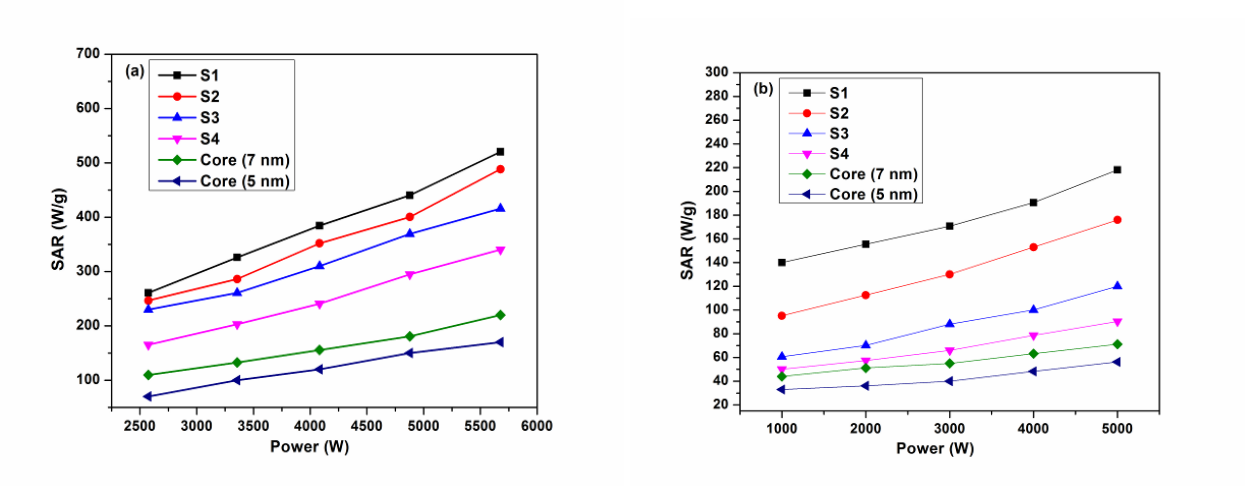

Figure 4.14. The SAR functions for the frequencies a) 1955, and b) 450 kHz of samples

This increase in SAR values indicates that the magnetic coupling may play an important role in defining the heating mechanisms. The magnetic exchange coupling between nanocrystals lead to decrease of the anisotropy energy, which allows increase of the total magnetic moment for magnetic nanoparticles.[81]

In the case of large nanoparticles, heating occurs due to the hysteresis losses and the Brownian relaxation. For small nanoparticles in the single-domain or superparamagnetic range, heating arises from the Neel and Brownian relaxation. Neel relaxation dominates when the nanoparticles are less than 20 nm, and Brownian relaxation dominates when the nanoparticles are larger than 20 nm.[75] In the case of our systems the increase of heating efficiency with CS-MNPs size is attributed to the Neel relaxation of nanoparticle. Another related parameter which strongly influences the SAR value is the shell thickness.

The impact of the thickness of the CS-MNPs on magnetic properties has been studied by varying the precursor concentration. As expected from the increased shell thickness made in sample S1, it was observed the highest SAR. So increasing the shell thickness will enhance the exchange reaction in CS-MNPs. Also the shape of magnetic nanoparticle is a key factor which influences magnetic properties. Noh *et al.* showed that the SARs of CS-MNPs were influenced by the shape of magnetic nanoparticle, and also observed that cubic $Zn_{0.4}Fe_{2.6}O_4$ had a higher M_s as compared to spherical MNPs of the same volume.[61]

4.3 PART III

We performed the functionalization of the CS-MNPs via DA reaction for bonding of DOX via a corresponding linker and later the rDA reaction for dis-bonding. The method uses the property of the reversible breaking of C=C bond as thermo-responsive switch. The drug release rate is controlled on-demand by switching the external magnetic field. With a fast heating rate of magnetic colloid and a carbon bond/disbond thermally activated mechanism in the nanoparticles, an accelerated drug release rate could be achieved (scheme 4.1).

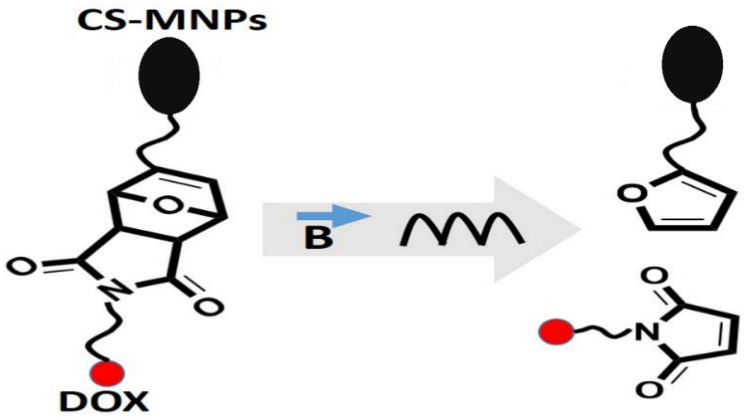

Scheme 4.1. Retro-Diels-Alder reaction mechanism

4.3.1 Structural characterizations of truncated octahedron magnetic nanoparticles

The XRD pattern of the nanopowder is shown in Figure 4.15 The Bragg reflections indexed to planes (220), (311), (400), (422), (551), (440) and (335) match with the reported values of the face-centered cubic (fcc) unit cell of the spinel structure with the space group Fd-3m (card no. 98-007-9524, PDF-4 Database). No residual phases were observed. The mean crystallite size is 7.8±0.4 nm.

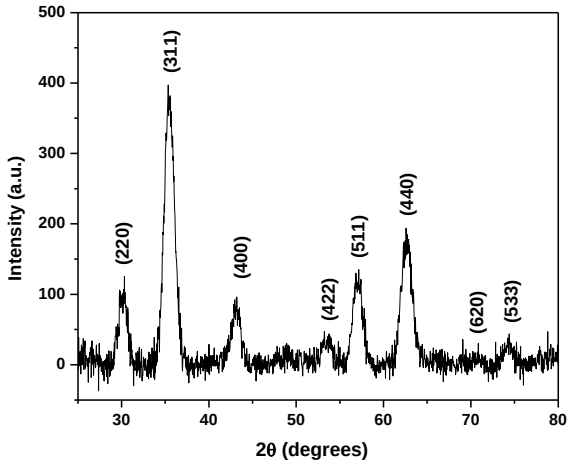

Figure 4.15. XRD pattern of CS-MNPs

The mean hydrodynamic diameter of the CS-MNPs dispersed in hexane, investigated by DLS, was calculated as 10.9±0.5 nm. The TEM measurements of CS-MNPs nanoparticles are displayed in Figure 4.16a. The images suggest a polyhedron-type shape of essentially monodispersed nanoparticles with a mean diameter of 9.7±0.4 nm. The DF-TEM confirm the CS-MNPs morphology of hard/soft magnetic phases (Figure 4.16b). The shell thickness was evaluated as 2±0.3 nm.

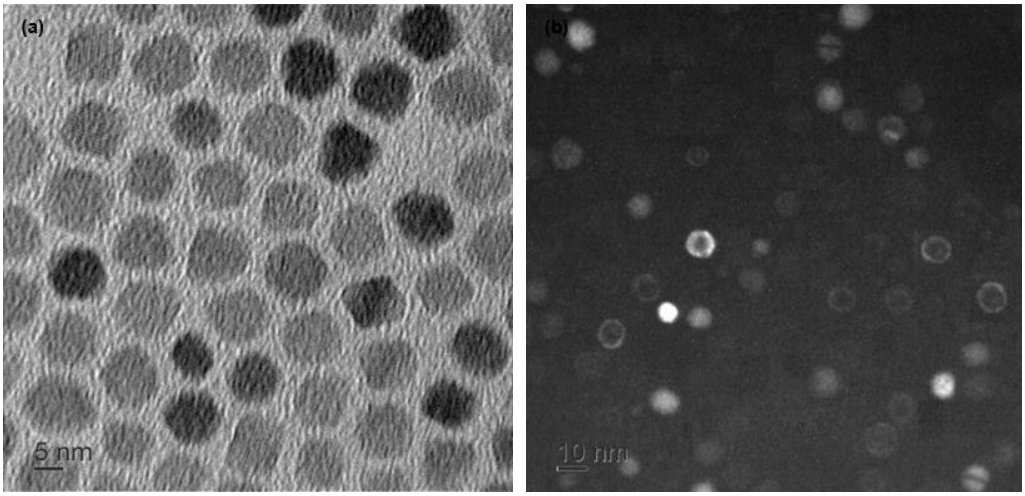

Figure 4.16. a) TEM and b) DF-TEM micrographs of CS-MNPs.

XPS was performed to analyze the valence state of the cations and chemical composition of the CS-MNPs. Figure 4.17a shows the XPS photoemission peaks of O1s, Mn2p, Co2p, Zn2p, and Fe2p core levels. The Co2p spectrum has been deconvoluted into four contributions (Figure 4.17b). The first two peaks with binding energies (BE) of 782.11 and 787.50 eV are attributed to $Co2p_{3/2}$ and its satellite, whereas the peaks centered at 797.32 and 802.65 eV correspond to $Co2p_{1/2}$ and its satellite, respectively. The $Co2p_{1/2}$ and $Co2p_{3/2}$ peaks proved the Co^{2+} species in an octahedral spinelic structure.[82] Their corresponding satellites with BE splitting of 6.2 eV confirm the Co bivalent cations in the octahedral sites.[83,84] Two broad and asymmetric peaks at 642.0 and 653.3 eV (Figure 4.17c), correspond to $Mn2p_{3/2}$ and $Mn2p_{1/2}$, respectively.[85] The $Mn2p_{3/2}$ photoemission peak can be deconvoluted into three contributions centered at 640.4, 642.4, and 646.6 eV, attributed to Mn^{2+}, Mn^{4+} (that suggests oxidation of Mn^{2+} cations), and its satellite, respectively.[66,86] The asymmetric $Mn2p_{3/2}$ peak indicates the presence of mixed-valence manganese cations. The co-presence of manganese in different oxidation states is consistent with reported data on the $MnFe_2O_4$ structural phase.[87] The XPS spectrum fitting of Fe2p displays the peaks of Fe^{2+} and Fe^{3+} cations and its satellites (Figure 4.17d). The Fe2p peaks are composed of two main asymmetric peaks, $Fe2p_{3/2}$ and $Fe2p_{1/2}$ with BE centered at about 711.0 and 725.0 eV respectively, and match to α-Fe_2O_3 phase formation. The BE centered at 711 eV is attributed to Fe^{3+} cations in the spinel structure.[88] In addition, the two common satellite peaks at 719.72 and 732.40 eV confirmed the Fe oxidation states of CS-MNPs.[89] Fe_3O_4 does not show any satellite peak due to overlapping of two satellite peaks corresponding to Fe^{3+} (at 8.0 eV) and Fe^{2+} (at 6.0 eV).[90] Figure 4.17e shows the Zn2p high resolution XPS spectrum. The $Zn2p_{3/2}$ and $Zn2p_{1/2}$ core level peaks at 1021.4 and 1044 eV, respectively, are in agreement with the oxidation state of Zn^{2+} in the sample.[91,92] The peak at 1021.4 eV confirms the Zn^{2+} occupying octahedral sites.[93] The O1s peak is deconvoluted into two contributions at 530 and 531 eV, that are attributed to the crystal lattice oxygen and surface-adsorbed oxygen, respectively (Figure 4.17f).[94]

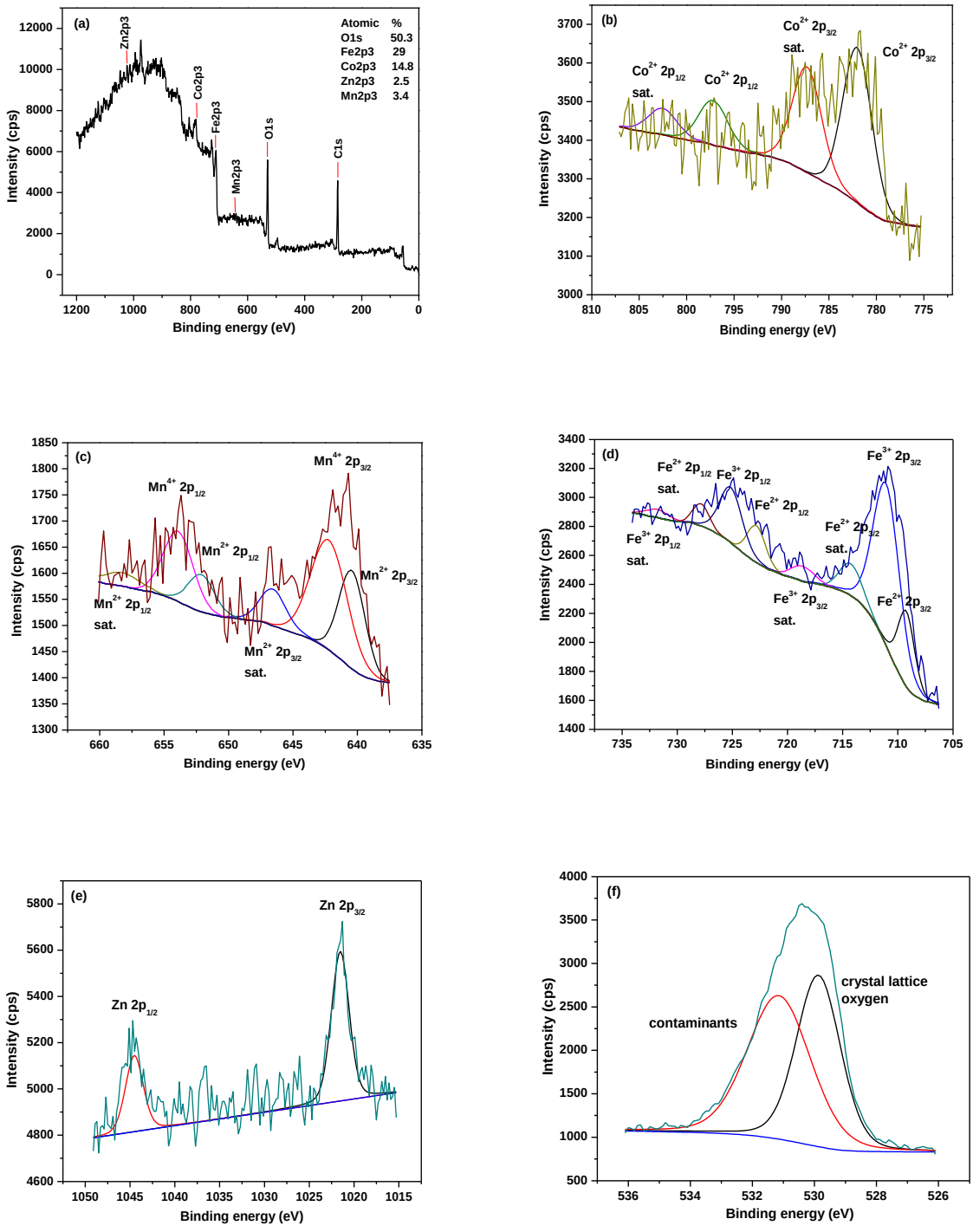

Figure 4.17. a) XPS spectra of CS-MNPs. Fitted photoelectron peaks of: b) Co2p1/2 and Co2p3/2; c) Mn2p1/2and Mn2p3/2; d) Fe2p1/2 and Fe2p3/2; e) Zn2p1/2 and Zn2p3/2; f) O1s.

The effect of time on the colloidal stability of CS-MNPs capped with TMAOH was investigated by DLS. However, the time-dependent hydrodynamic diameter of the CS-MNPs does not show significant variation (Figure 4.18).

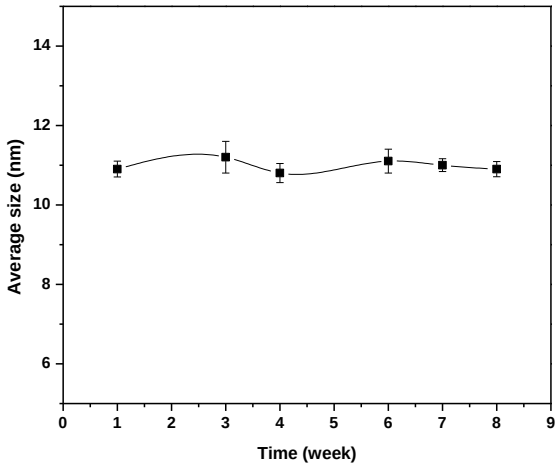

Figure 4.18. Stability of CS-MNPs in water up to 8 weeks.

4.3.2 Magnetic properties of truncated octahedron magnetic nanoparticles

The magnetic measurements of CS-MNPs and functionalized CS-MNPs are shown in Figure 4.19. The magnetization curves display a superparamagnetic behavior of the systems that could be assigned to the small-size effect of the nanoparticles. This property is important in biomedical applications whereas the nanoparticles aggregation or cluster formation should be avoided.[95] The M_s of core-shell nanoparticles was calculated as 50 emu/g. The lower value of M_s (29 emu/g) of functionalized CS-MNPs could be explained by non-magnetic contribution of the surface layer that is accounted in the weight of the sample. A relatively high M_s of functionalized nanoparticles could be an important factor for magnetically targeted delivery system.

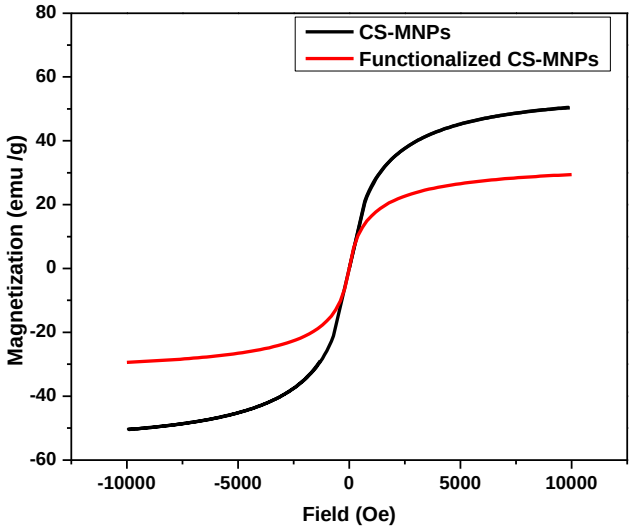

Figure 4.19. The magnetization curves of CS-MNPs and functionalized CS-MNPs.

By using a linear extrapolation for the heating (upon AMF) and cooling branches, we can evaluate the T_c as the intersection point of temperature change over time (dT/dt) with temperature (Figure 4.20). The T_c of CS-MNPs in aqueous medium was estimated at 363 K.

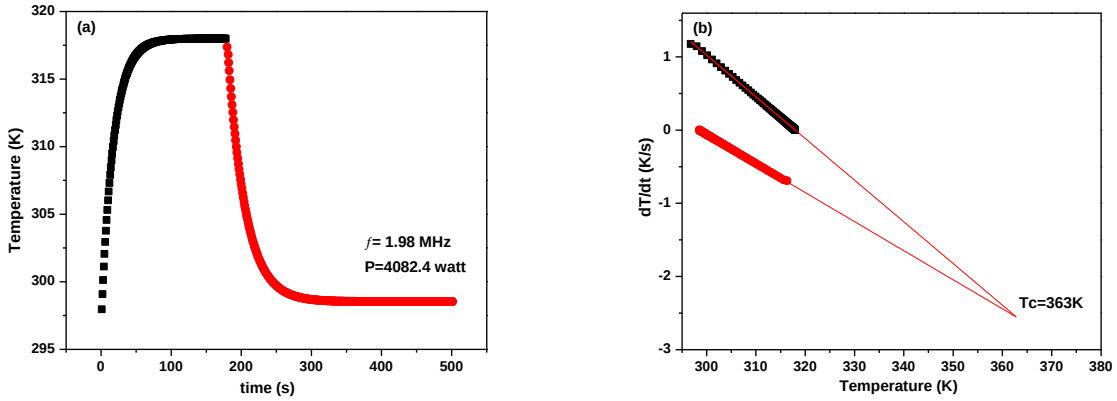

Figure 4.20. a) Temperature curves over time of CS-MNPs. b) Temperature change rate in unit time (dT/dt) versus temperature of CS-MNPs.

In order to evaluate the heating performance on CS-MNPs, we have calculated the SAR according to the equation 4.1. Figure 4.21 displays the dependence of SAR with different power values at two frequencies for core and CS-MNPs. The SAR values of CS-MNPs were compared with those of single-component magnetic nanoparticles. The SAR of magnetic cores ranges from 20 to 130 W/g at 450 KHz and from 34 to

163 W/g at 1950 KHz. In contrast, for CS-MNPs SAR was estimated in the limits of 70 to 210 W/g at 450 KHz and from 218 to 452 W/g at 1950 KHz. The SAR of core-shell nanoparticles is significantly higher than those of single component particles. This clearly indicates CS-MNPs are magnetically exchange-coupled and proved an important enhancement of magnetic heat induction.

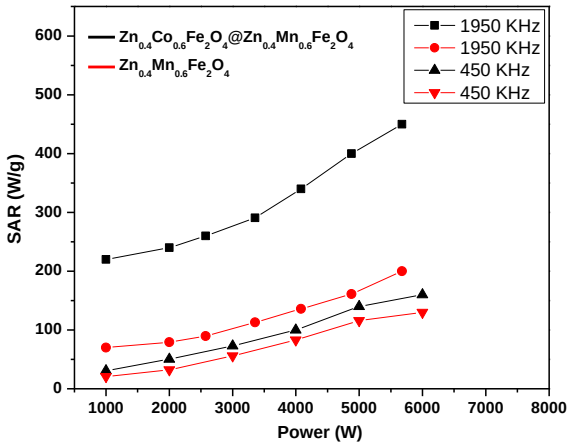

Figure 4.21. The dependence of SAR on electromagnetic power for the magnetic fluid samples at selected frequency values.

4.3.3 Cytotoxicity assay of functionalized magnetic nanoparticles

HepG2 is a perpetual cell line consisting of human liver carcinoma cells, derived from the liver tissue of a 15-year-old Caucasian male who had a well-differentiated hepatocellular carcinoma. HepG2 can be grown in a large scale, and secret a variety of plasma proteins, such as transferring, fibrinogen, plasminogen and albumin. They can be stimulated with human growth hormone. HepG2 are adherent, epithelial-like cells growing as monolayers and in small aggregates.[96] HeLa cell is derived from a cervical carcinoma from a 31 year old female and have served as a standard for understanding many fundamental biological processes. They have many basic characteristics as the normal cells, such as producing proteins, expressing and regulating genes, and are susceptible to infections.

To determine the cytotoxicity of the functionalized CS-MNPs, The HeLa and Hep G2 cells were treated with culture medium containing functionalized CS-MNPs at different concentrations (12.5–200 µg) and incubated for another 24 h. The cell viability of Hep G2 is decreased to 87 % after 24 h of treatment within the highest concentration of functionalized CS-MNPs (Figure 4.22a); however, cell viability of HeLa

maintains more than 90 % for the CS-MNPs (Figure 4.22b), indicating that the functionalized CS-MNPs are non-toxic. Therefore, it can potentially be applied as drug carriers for biological applications.

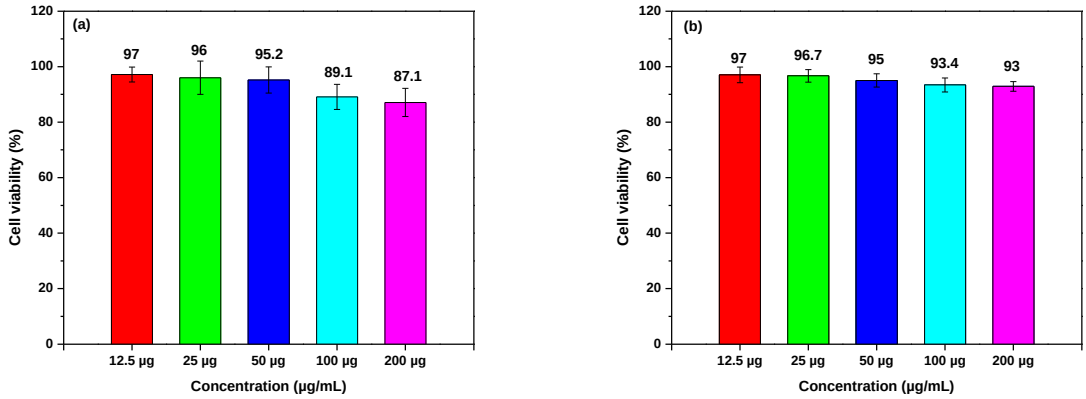

Figure 4.22. Cell viabilities of functionalized CS-MNPs with a) Hep G2, and b) HeLa cells measured by MTT assay.

4.3.4 Conjugation of doxorubicin to functionalized magnetic nanoparticles

In the process of drug loading and releasing, the drug molecules (DOX) can be easily attached onto the surface of CS-MNPs through an amide bond. We prepared functional CS-MNPs according to figure 4.23. The CS-MNPs were first synthesized through a seed-mediated growth method. The particle surfaces (1) were modified with TMAOH in order to disperse the CS-MNPs in an aqueous media. To stabilize and functionalize the hydrophilic CS-MNPs, alendronic acid which has a primary amine (2) is used to form the thiourea compound (3) upon addition of 2-furfuryl isothiocyanate. The DA cycloadduct (4) was synthesized using the Furan-modified magnetic nanoparticle as dienes and N-(2-Carboxyethyl)maleimide as dienophiles.

Prior to enable a rDA mediated release, DOX (5) was conjugated to the as-synthesized particles by amide conjugation in the presence of the crosslinkers EDC and NHS. Moreover, the drug-loaded nano-carriers could be targeted to the specific site under the application of an external magnetic field to improve drug release capability. The loading efficiency of nanoparticles is about 92%.

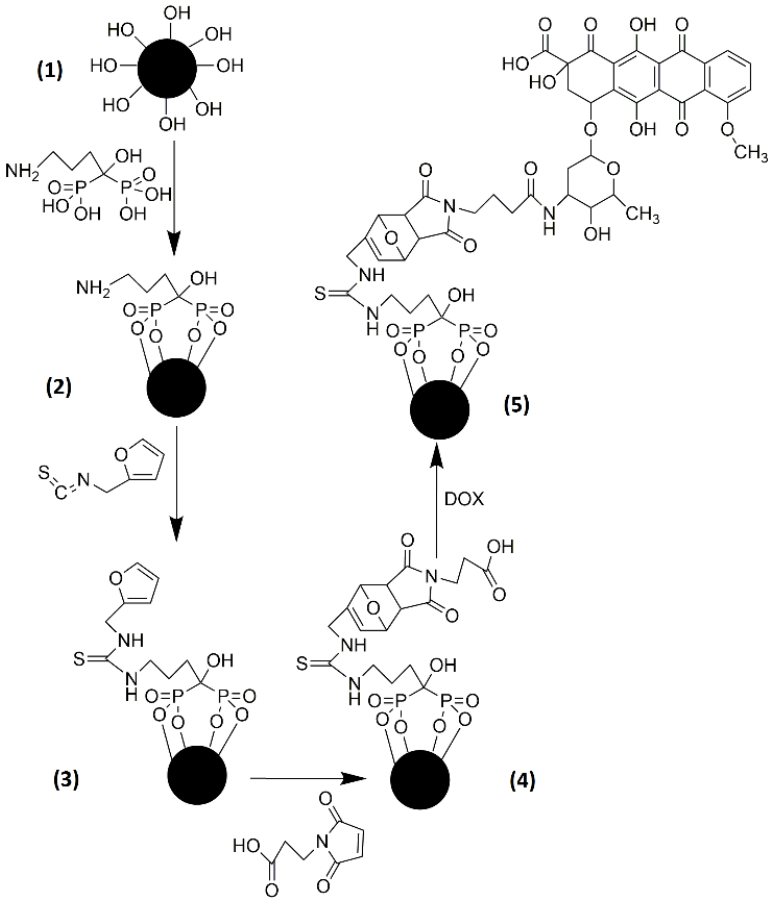

Figure 4.23. Illustration of the functionalization mechanism of CS-MNPs

The FTIR analyses were performed in order to attest the functionalization on CS-MNPs (Figure 4.24). The spectrum of CS-MNPs confirms the presence of metal-oxygen intrinsic stretching vibrations in both octahedral (580 cm^{-1}) and tetrahedral sites (620 cm^{-1}) of the spinel lattice. Typical C-H vibration in the wavelength range of 2800-3000 cm^{-1} and a broad peak of C=O vibration of the carboxyl functional groups in the range of 1600 - 1750 cm^{-1} are attributed to the oleic acid, an intermediate in the synthesis. The spectrum of further TMAOH functionalized magnetic nanoparticles presents a vibrational band in the limits of 3000-3500 cm^{-1} that could be assigned to the adsorbed water molecules on the nanoparticles surface (sample 1). Two characteristic peaks of alendronic acid bonded to TMAOH, at 1635 cm^{-1} and 1125 cm^{-1}, are associated to P=O bending vibration and to C-N vibrational band, respectively (sample 2). The IR spectrum of CS-MNPs bearing furan shows the typical stretching vibration signals of C-H (760 cm^{-1}, 1240 cm^{-1}) and C=C (1510 cm^{-1}) functional groups (sample 3). The disappearance of the antisymmetric S=C=N band between 2000-2100 cm^{-1} confirms the surface modification of the particles. The vibrational bands between 1700-1500 cm^{-1} correspond to C=O functional group that are specific to maleimide. The vibrational band of the acid amide group is located at 1650 cm^{-1} due to the -CO stretching vibration

(sample 4). The significant peaks observed at 1530 and 877 cm^{-1} corresponded to the C−N stretching vibrations and to the N−H bending vibration of −CO−NH− group, respectively, confirming the loading of DOX (sample 5).

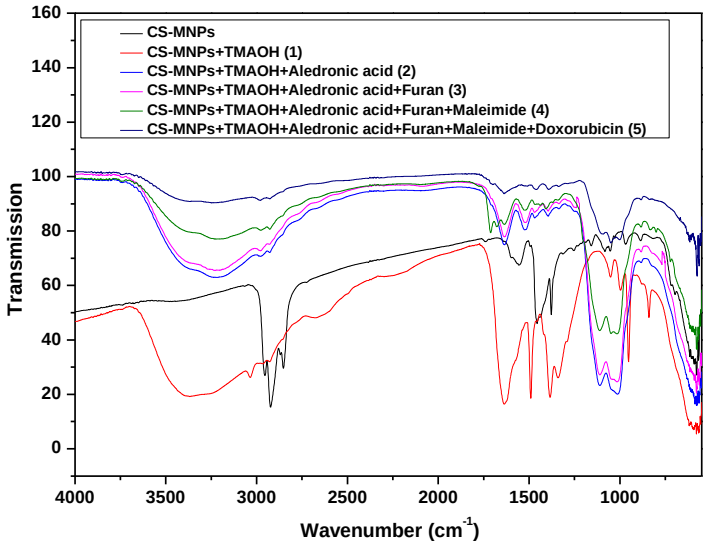

Figure 4.24. FTIR spectra of functionalized CS-MNPs.

The TG curves of the functionalized nanoparticles are performed to prove the functionalization of the CS-MNPs (Figure 4.25). The measurements showed that the mass loss increases with the increase in the reacting mass ratio. For all the patterns, a major weight loss was observed between 200 and 600 °C which is due to the thermal decomposition of the organic species on the CS-MNPs surface, as indicated by FTIR. The TG curve of sample 1 displays an initial weight loss (3.6 %). The weight loss in the temperature range 30−120 °C is attributed to the removal of adsorbed water and to the hydroxyl groups that belong from TMAOH and/or alkanolamine. The weight loss (13.12%) of Sample 2 in the temperature range 200-500 °C was associated to the alendronate desorption zone. The TG curves of the sample 3 clearly shows a decrease in mass at an early stage (17.2 %), which is ascribed to the loss of the furan moieties. rDA reaction occurred for sample 4 in the heating process to generate some free maleimide and furan groups in the sample, which contributed to the increase of weight loss to 20.1 %. Crosslinking reaction occurred between some free maleimide groups enhancing its thermal stability and reducing the amount of weight loss at 400–500 °C. Finally, the significant weight loss (24.68 wt %) of sample 5 is attributed to the release of DOX. The mass loss decreased rapidly from approximately 250 °C to 400 °C, which can be associated to the rDA reaction and DOX decomposition.

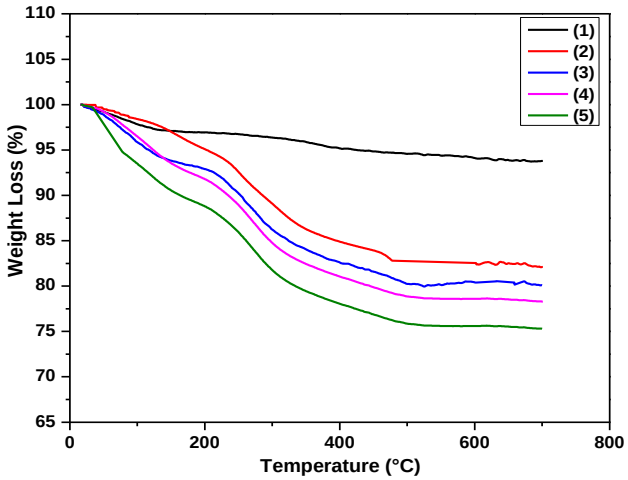

Figure 4.25. TG patterns of functionalized CS-MNPs.

4.3.5 Doxorubicin release profiles

The thermo-responsive nano-carriers are desirable to preserve their payload at body temperature and to rapidly deliver the drug within locally heated tissue to overcome side effects as pathophysiological changes in the vascular system and washout from the tumor. There are several challenges associated with the self-healing materials based on DA reaction, such as the occurrence at high temperatures (80-120 °C) to trigger the rDA reaction that is not compatible with biological applications.[97,98]

The drug release rate of our magnetic system is thermally on-demand controlled by switching on or off of HF-AMF. Upon AMF (frequency 1950 kHz, power 6200 W) the temperature of the sample increased from 37 °C to 50 °C, and remained in this plateau for 15 min (Figure 4.26a). Figure 4.26b shows the cumulative release of DOX from functionalized CS-MNPs at 50 °C. The release profile shows more than 90% (after 15 min) release of the DOX molecule. At elevated temperatures we note a reverse reaction and the reformation of maleimide and furan moieties respectively. With a fast heating rate of magnetic colloid upon AMF and a C=C bond/disbond thermally activated mechanism of functionalized nanoparticles, an accelerated drug release rate has been achieved. We observed a non-significant drug release at body temperature.

The thermo-responsive release of the DOX from CS-MNPS was evaluated by varying the temperature of the samples (Figure 4.26c). At low temperature (25 °C) no release of doxorubicin was detected. A

significant DOX amount was released at 48 °C compared to 37 °C (40 % and 5 %, respectively). The higher release rate observed at elevated temperatures corresponds to an increased reverse rate in the rDA reaction.

The release of DOX from functionalized CS-MNPs is on-demand controlled by switching on (i.e. 46 % release during a period of 4 min at 50 °C) or switching off the AMF as shown in Figure 4.26d.

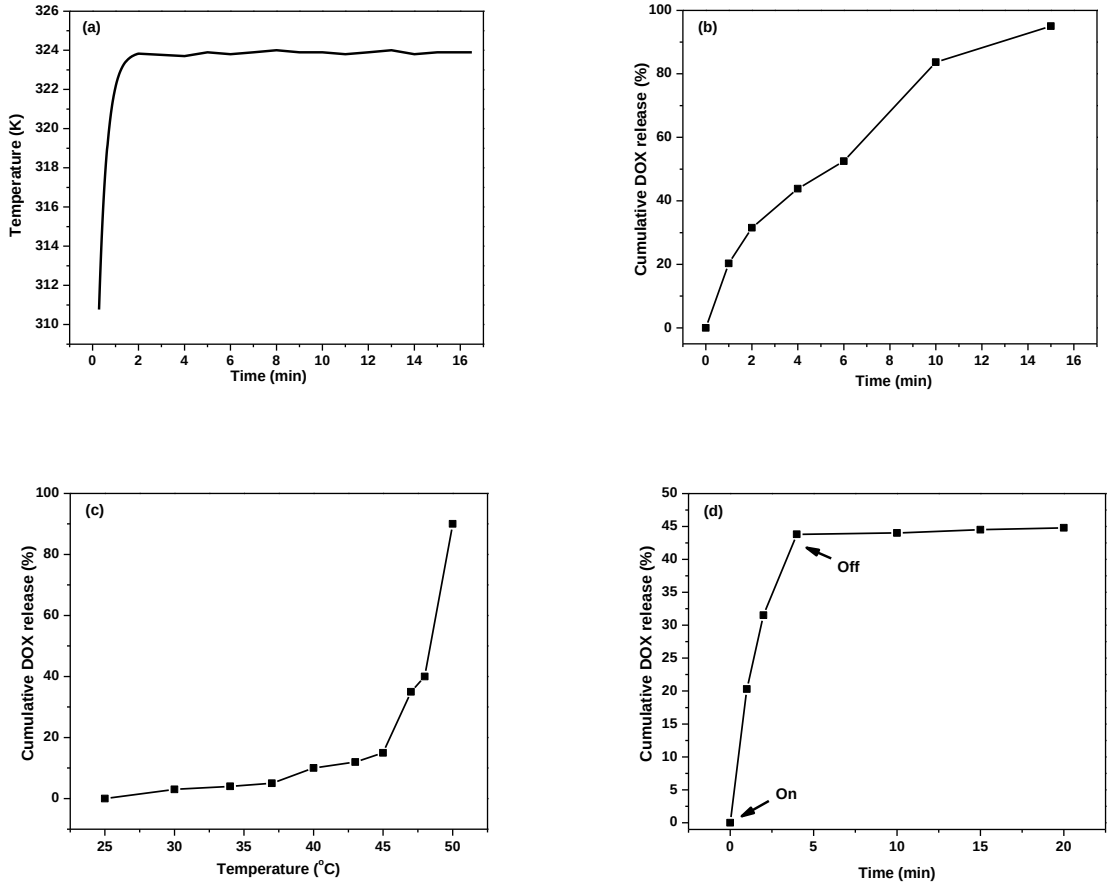

Figure 4.26. a) Time-dependent temperature curve of CS-MNPs under AMF. b) Cumulative DOX release profile under AMF. c) DOX release profile as a function of temperature. d) Switch-on under AMF and switch-off profile release of DOX.

Some authors have demonstrated that hyperthermia has potential as an effective treatment for many solid tumors without injury to normal tissue for temperatures at or above 50 °C.[99,100] Cancer cells may confer thermo-tolerance as a result of continuous heat exposure within 30 min at 43 °C.[101] Inhibition of heat-shock proteins (HSPs) in tumor cells could overcome the thermo-resistance and enhances the apoptosis during magnetic hyperthermia by increasing the rate of heat transfer which is obtained by CS-

MNPs. Otherwise, some authors indicated an uncoupling of thermo-tolerance and Hsp70 expression under slow rate heating conditions.[102] Magnetic hyperthermia is a viable tool for on-demand drug release inducing melting and subsequent capsule rupture on exposure *via* water ingress *in vivo*.[103] We report a novel magnetic drug release system that uses click chemistry reactions on-demand by heating upon AMF. A fast drug release is activated by rDA reaction and could be applied synergistically with hyperthermia.

Other authors reported a new class of functionalized iron oxide nanoparticles initiating the rDA reaction at 70 °C without AMF.[104] Even though those temperatures seem to be very high for a biological medium, recent studies have shown the existence of local heating profiles generated at the magnetic nanoparticles surface upon AMF, leading to high temperatures within a contour only of a few nanometers.[105] Some authors use gold nano-rods to initiate the polyethylene glycol chain release through rDA by the photo-thermal effect.[106]

The stability of DOX loaded nanoparticles was evaluated up to 8 weeks in PBS at 25 °C (Figure 4.27). The results show that the stability of DOX loaded CS-MNPs was around 85 %.

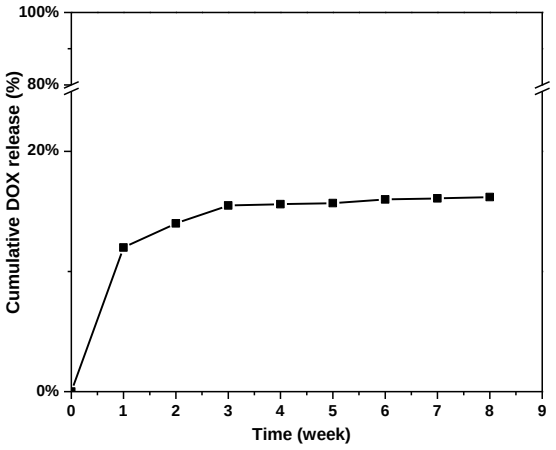

Figure 4.27. Stability of DOX loaded CS-MNPs in PBS up to 8 weeks.

4.4 PART IV

This section concern the development of a dual pH- and thermo-responsive magnetic nanoparticles drug carrier by using the LBL technique which is suitable for the magneto-thermal therapy and controlled release. Spherical CS-MNPS with high magnetic responsiveness, synthesized by seed-mediated growth, were coated with PAH and PAA multilayers (Scheme 4.2). Subsequently, the release profile of the nano-carriers was investigated via loading DOX molecules. The method uses the oscillating magnetic field as external trigger and the polyelectrolyte membrane as receptor. Due to the induced thermo-responsiveness, the polymeric shell releases the entrapped drug by dissociation. The drug release rate is remotely controlled using on-off durations of oscillating magnetic field for a sustained drug release.

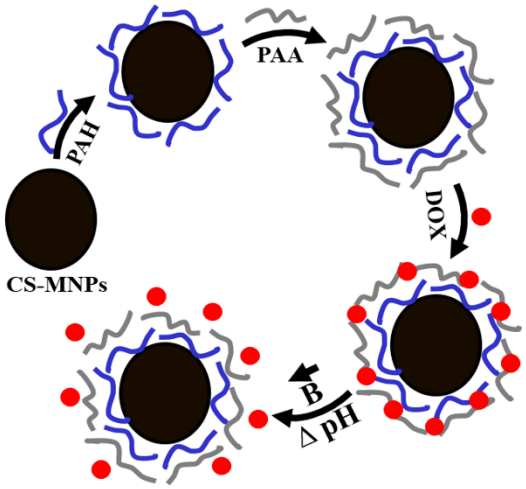

Scheme 4.2. LBL assembly of CS-MNPs

4.4.1 Structural characterizations of spherical magnetic nanoparticles

The XRD pattern of the nanopowder is shown in Figure 4.28. The (220), (311), (400), (422), (511), and (440) diffraction peaks are matched to the Bragg reflections of the spinel ferrite structure. The mean crystallite size is 7.8±0.5 nm.

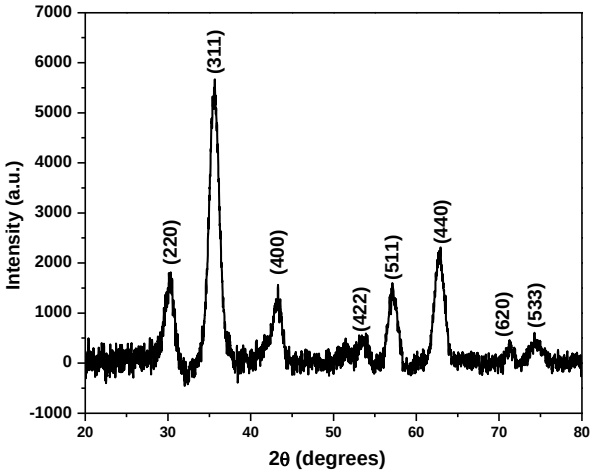

Figure 4.28. XRD pattern of CS-MNPs

DLS was used to determine the mean hydrodynamic diameter of the particles (9.7±0.6 nm).

XPS measurements were performed to examine the valence change of the cations and chemical composition of the CS-MNPs. Figure 4.29a shows the XPS photoemission peaks of O1s, Mn2p, Co2p, Zn2p, and fe2p core levels. The XPS of Co2p regions can be fitted into four contributions (Figure 4.29b). The XPS spectrum of Co2p exhibits two strong peaks located at BE of 781 and 796.4 eV, which can be attributed to $Co2p_{3/2}$ and $Co2p_{1/2}$, respectively, and are associated with corresponding shake ups peaks at 786.5 and 802.7 eV, respectively. The Co2p spectrum indicate that Co exist in 2+ oxidation state, since the intense shakeup Co2p satellites are acquired from the unpaired valence 3d electron orbitals of the high spin Co^{2+}.[64] In the Mn2p spectrum (Figure 4.29c), the major peak $Mn2p_{3/2}$ is at 642.2 eV and the minor one $Mn2p_{1/2}$ is at 653.8 eV, providing a clear evidence for Mn^{2+} chemical state on the sample surface.[65] The $Mn2p_{3/2}$ spectra can be deconvoluted into three contributions centered at 640.4, 642.4, and 646.6 eV, which is in good agreement with the value reported for Mn^{2+}, Mn^{4+}, and its satellite, respectively.[66] The Fe2p spectra are characterized by BE of the $Fe2p_{3/2}$ and $Fe2p_{1/2}$ core levels of 711.2 and 724.3 eV, respectively (Figure 4.29d), and are accompanied by two corresponding satellite peaks for $Fe2p_{3/2}$ and $Fe2p_{1/2}$ visible at binding energies of around 719.2 and 731.0 eV, which is indicative of the presence of Fe^{3+} cations.[67] The binding energies of the $Zn2p_{3/2}$ and $Zn2p_{1/2}$ core level peaks are 1021.4 and 1044 eV, respectively, confirming the presence of Zn^{2+} species (Figure 4.29e).[91] The O1s peak is deconvoluted into two contributions at 530 and 531 eV, which are attributed to the crystal lattice oxygen and surface-adsorbed oxygen, respectively (Figure 4.29f).

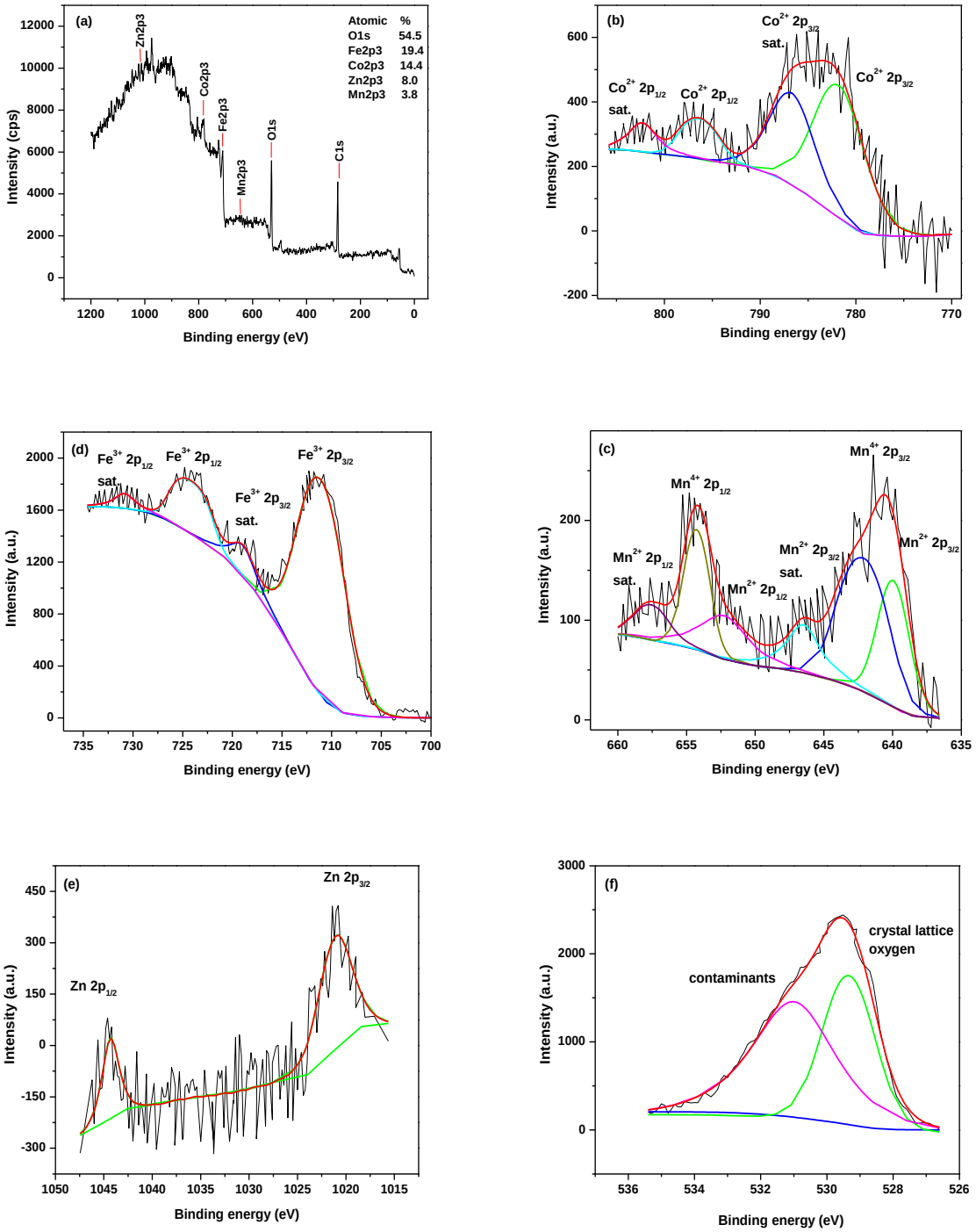

Figure 4.29. a) XPS spectra of CS-MNPs. Fitted photoelectron peaks of: b) Co2p1/2 and Co2p3/2; c) Mn2p1/2and Mn2p3/2; d) Fe2p1/2 and Fe2p3/2; e) Zn2p1/2 and Zn2p3/2; f) O1s.

4.4.2 Magnetic properties of spherical magnetic nanoparticles

Magnetization analysis was carried out using a vibrating sample magnetometer in external magnetic fields ranging from -1 T to 1 T in order to study the static magnetic properties of CS-MNPs in powder form at room temperature. The magnetization curve of CS-MNPs, (PAH/PAA)-CS-MNPs (Sample S1), $(PAH/PAA)_2$-CS-MNPs (Sample S2), and $(PAH/PAA)_3$-CS-MNPs (Sample S3) show a superparamagnetic behavior with a M_s of 45.6, 22.3, 18.7, and 13.1 emu/g, respectively (Figure 4.30).

The lower value of M_s of coated CS-MNPs could be assigned to the coating of the surface layer that reduced the weight ratio of CS-MNPs in the sample. Superparamagnetic property and high SAR values are the key parameters for controlled drug release *and* synergistic hyperthermia.

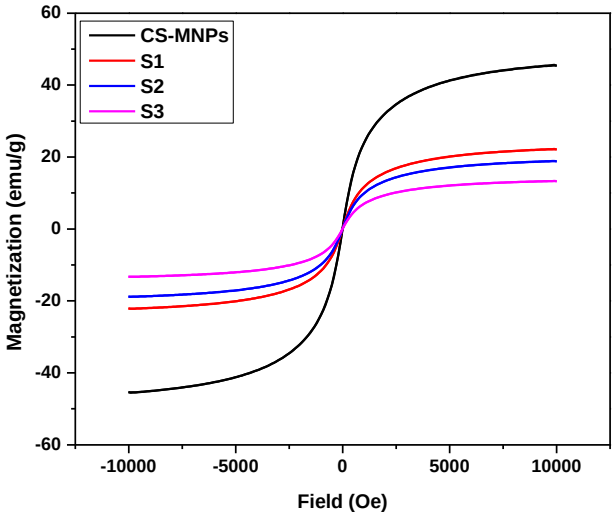

Figure 4.30. The magnetization curves of CS-MNPs and coated CS-MNPs.

Figure 4.31a shows the temperature curves over time of CS-MNPs at different power values. In order to evaluate the heating performance on these CS-MNPs, the SAR value was measured. The sample was subjected to HF-AMF with different power values from 2500 to 5700 W at a frequency of 1950 kHz. SAR values expressed as W/g were calculated according to the equation (4.1).

Figure 4.31b presents the variation of the SAR of the ferrofluid with the power of the HF-AMF. As expected, higher SAR values were recorded by increasing the applied power. In the case of CS-MNPs, the SAR values are (ranging from 200 to 360 W/g) higher compared to the core SAR values (ranging from 90 to 170 W/g). This clearly indicates that the obtained $Zn_{0.4}Co_{0.6}Fe_2O_4$@$Zn_{0.4}Mn_{0.6}Fe_2O_4$ nanoparticles are magnetically exchange-coupled.

For superparamagnetic particles, the SAR will result from relaxation processes. These processes in ferrofluids are either due to reorientation of the magnetization within the particle (Néel losses) or due to reorientation of the particles and concomitant frictional losses (Brown losses).[107] In the case of systems with small dimensions of nanoparticles the contribution due to Brownian losses can be considered negligible. The SAR for superparamagnetic nanoparticles depends on the Néel losses.

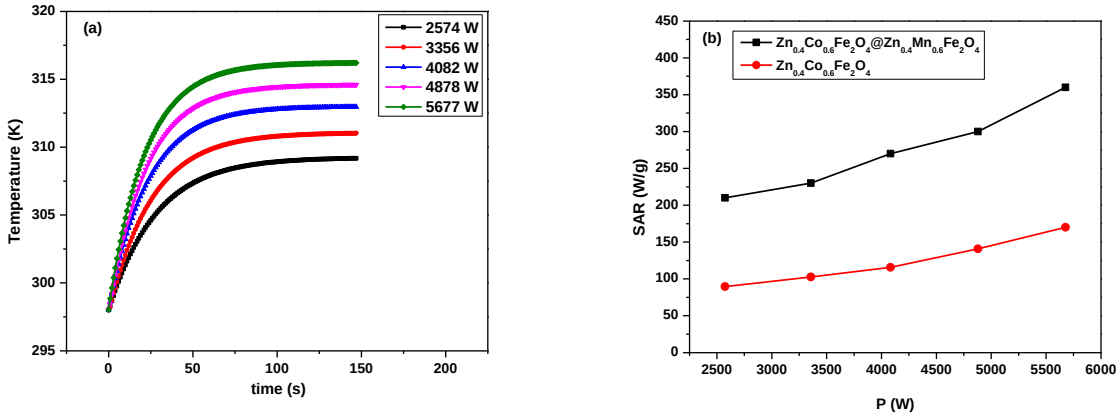

Figure 4.31. a) Temperature curves over time of CS-MNPs at different power values. b) The SAR functions of core and CS-MNPs.

4.4.3 Cytotoxicity Assay of nanoparticles

To evaluate the cytotoxicity of the core-shell magnetic nanoparticles, the functionalized CS-MNPs were incubated with HeLa, and Hep G2 cell lines and a standard MTT cell assay was used for the study. The cell viability of Hep G2 is decreased to 92 % after 24 h of treatment within the high-dosage concentrations of functionalized CS-MNPs (200 µg/mL) (Figure 4.32a); however, the cell viability of HeLa maintains around 98 %, indicating that the functionalized CS-MNPs are nontoxic (Figure 4.32b). Therefore, the functionalized CS-MNPs can potentially be used as drug carriers in biological applications.

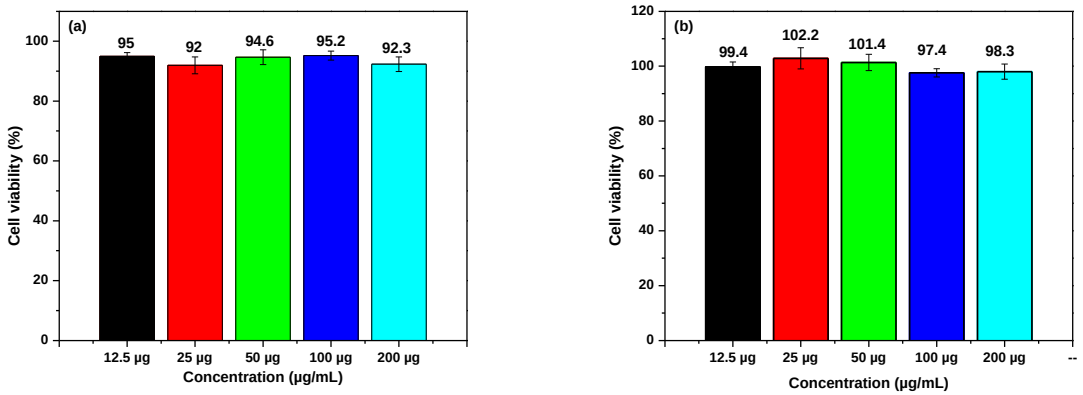

Figure 4.32. Cell viabilities of CS-MNPs with a) HeLa, and b) Hep G2 cells measured by MTT assay.

4.4.4 Loading of doxorubicin with coated magnetic nanoparticles

TEM images shows the shape and size of uncoated and coated MNPs (Figure 4.34). Figure 4.34a shows the DF-TEM of the CS-MNPs confirming the formation of CS-MNPs. The morphological change and the size enlargement are attributed to formation of the organic shell on the surface of the CS-MNPs, forming the encapsulation of the system into core-shell form. The thickness of the polyelectrolyte layer (S3) is estimated to be around of 6 nm.

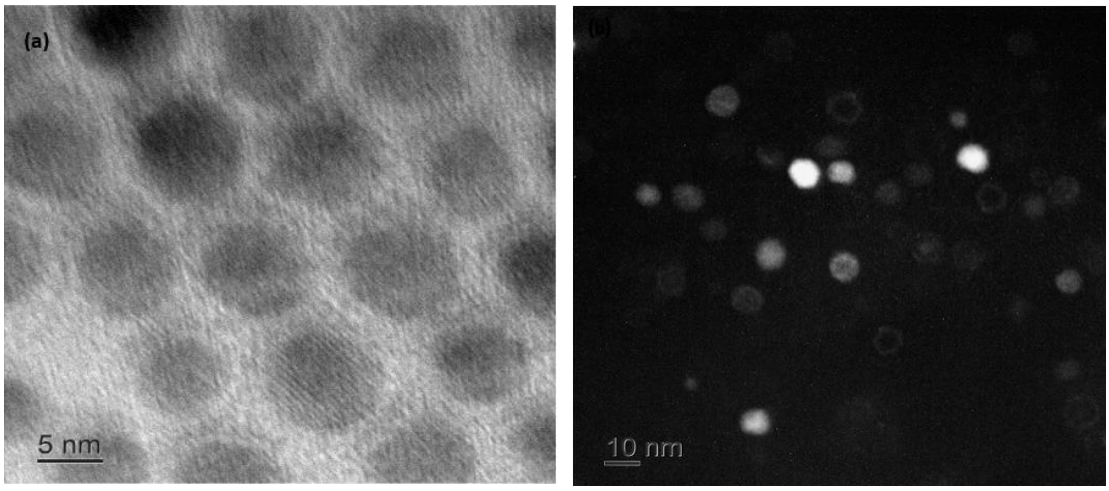

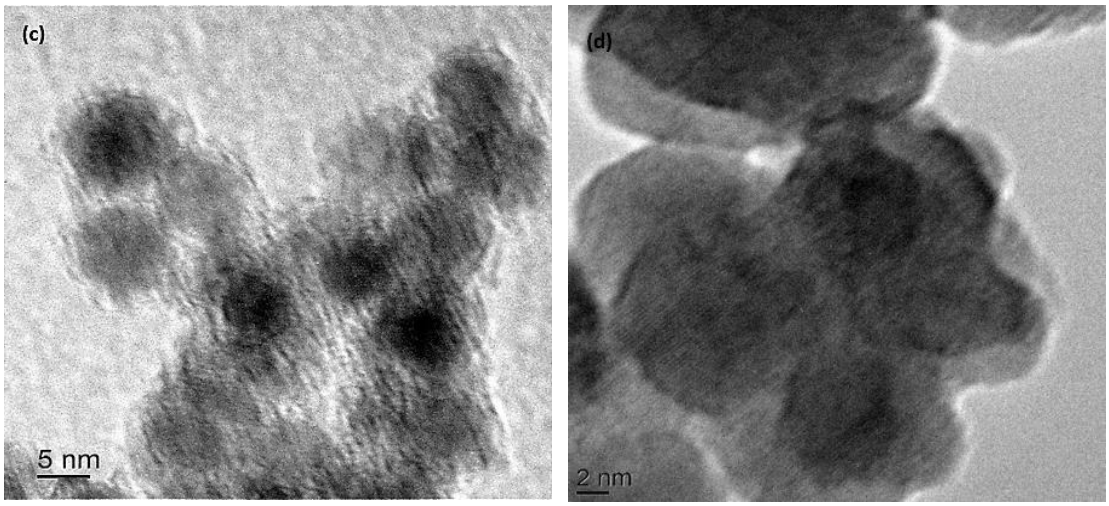

Figure 4.33. a) TEM images of CS-MNPS dispersed in hexane. b) Dark field-TEM images of CS-MNPS. c) CS-MNPS coated with PAH as the first layer. d) CS-MNPS coated with PAA as the last layer, 6 layer coated.

The change in the hydrodynamic size after each coating step was characterized by DLS (Figure 4.34 and Table 4.3). The mean hydrodynamic size of CS-MNPs dispersed in water is 55±2.3 nm. After first coating (PAH) on CS-MNPs, the particle diameter increased to 94±4.2 nm.

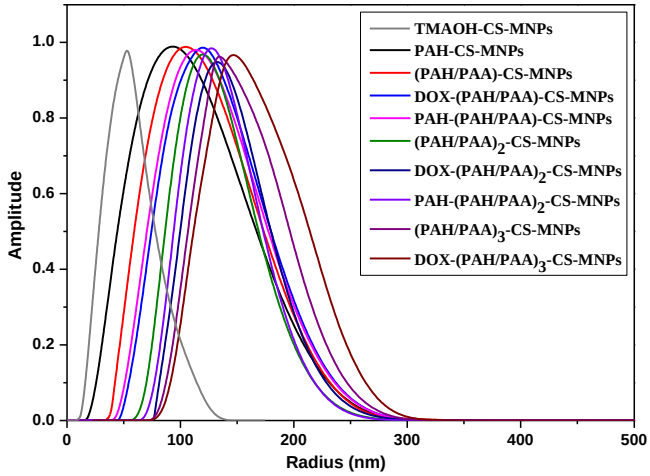

Figure 4.34. DLS measurements of CS-MNPs and differently coated magnetic nanoparticles.

Zeta potential measurement results show reversals of the surface charge of the MNPs upon each step of their coating (Figure 4.35 and Table 4.3). After positively charged PAH was coated onto the surface of the MNPs, the zeta potential and thus the total charge of the nanoparticles was changed from negative (-70 mV) to positive (+55 mV), which indicates the coating of MNPs with the oppositely charged

polyelectrolytes. The loading of DOX did not affect the surface charge significantly. High Zeta potentials of the samples indicate the high dispersity and stability of the nanoparticles in the medium.

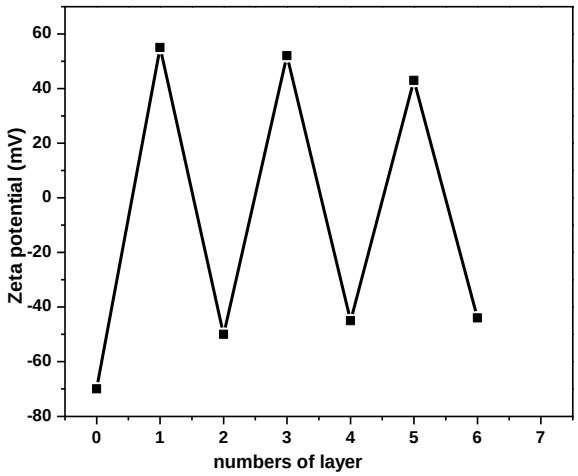

Figure 4.35. Zeta potential measurements of differently coated magnetic nanoparticles.

Table 4.3. DLS and Zeta potential result of uncoated magnetic nanoparticles and differently coated magnetic nanoparticles.

Functionalized MNPs	**Radius (nm)**	**Zeta potential (mV)**
MNPs in Hexane	9.7±0.6	
MNPs-TMAOH	55±2.3	-70
PAH-MNPs	94±4.2	+55
(PAH/PAA)-MNPs	104±4.8	-50
DOX-(PAH/PAA)-MNPs	115±3.9	-30
PAH-(PAH/PAA)-MNPs	110±4.5	+52
$(PAH/PAA)_2$-MNPs	118±4.8	-45
DOX-$(PAH/PAA)_2$-MNPs	128±5.8	-25
PAH-$(PAH/PAA)_2$-MNPs	120±3.7	+43
$(PAH/PAA)_3$-MNPs	133±3.9	-44
DOX-$(PAH/PAA)_3$-MNPs	140±4.2	-22

The FTIR analyses were performed in order to reveal the coating on the MNPs and the loading of DOX. Figure 4.36 confirms the functional groups of the polyelectrolyte layer coatings of as-synthesized nano-carriers. The spectrum of CS-MNPs shows the presence of Fe-O stretches at both the octahedral and tetrahedral sites. These can be seen in the large peaks around 580 and 620 cm^{-1}, and also shows typical C-H vibration in the wave length range of 2800-3000 cm^{-1}. The typically vibrations in the wavelength range of 3000-3500 cm^{-1} could be attributed to the adsorbed water molecules on the nanoparticles surface. After first coating with PAH, the spectra confirmed the presence of the NH_3 groups with stretching vibration band near 1500 cm^{-1} and 1600 cm^{-1}. The characteristic vibrational bands include the symmetric and antisymmetric stretching frequencies of the carboxylate ion (COO^-) at 1408 and 1562 cm^{-1}, respectively, indicating the PAA layer formation. The significant peaks observed at 1555 cm^{-1} could be attributed to the N−H bending vibration of the −CO−NH− groups and confirmed the loading of DOX.

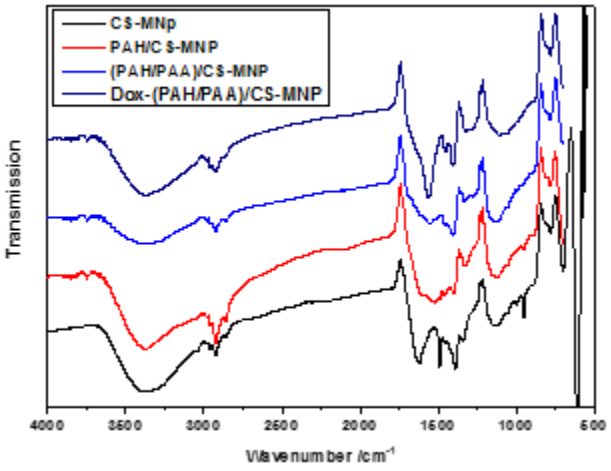

Figure 4.36. FT-IR spectra of functionalized CS-MNPs.

4.4.5 Doxorubicin release profile

The desired anticancer drug (DOX) is attached to the last layer (PAA) of the coated CS-MNPs in the presence of the crosslinkers EDC and NHS for controlled release. The loading efficiency of DOX (90.5 %) on the coated CS-MNPs was obtained. The HF-AMF is used as an external on-off switching control to trigger the release of DOX from the coated CS-MNPs through magnetic heating.

The samples were placed inside a water-cooled copper coil producing an HF-AMF with the frequency of 1950 kHz and a maximum power of 7200 W to measure the release of DOX considering parameters such as pH (5,7.2), buffer type (PBS), and temperature (25, 37, 40, 43 °C). At the on-off cycle, the sample was heated from 37 °C to 43 °C over the course of 3 min of pulsed duration with 7 min of cooling temperature profiles (Figure 4.37a). The results show that the DOX release from (PAH/PAA)-CS-MNPs (S1) is about 60 % after 80 min of a single pulse of HF-AMF (Figure 4.37b). In contrast, when multiple on-off cycles were applied, approximately 40 % of the DOX was released from S1 in the first on-off cycles, while more DOX was released in a gradual response after subsequent on-off cycles up to 8 cycles (80 min; Figure 4.37c). A dramatic change in the amount of released drug is evident when applied to multiple on-off cycles. The drug release profiles of DOX show two stages: a burst release of DOX is obtained under HF-AMF within first 3 min followed by a slower rate of release.

The coating thickness plays an important role in the elution of drug as it slows the dissociation of a drug from the coating and subsequently resulted in slower drug release rate. A similar on-off switchable drug release behavior was also observed for S2 and S3 (Figure 4.37c). The result show that the DOX was released from S2 within 110 min of subsequent on-off cycles, while DOX was released slower from S3 after subsequent on-off cycles of 140 min.

This system can control the amount of drug release after the burst release of the first on-off cycle as a function of the duration of the magnetic pulse. The amount of DOX released over each on-off cycle varies directly with the duration of magnetic pulse. Thus, drug release could be controlled by modulating both the frequency and duration of magnetic pulse. Other authors reported a DOX release from functionalized core/shell magnetic nanoparticles at 37 °C without controlling the rate of released DOX.[108]

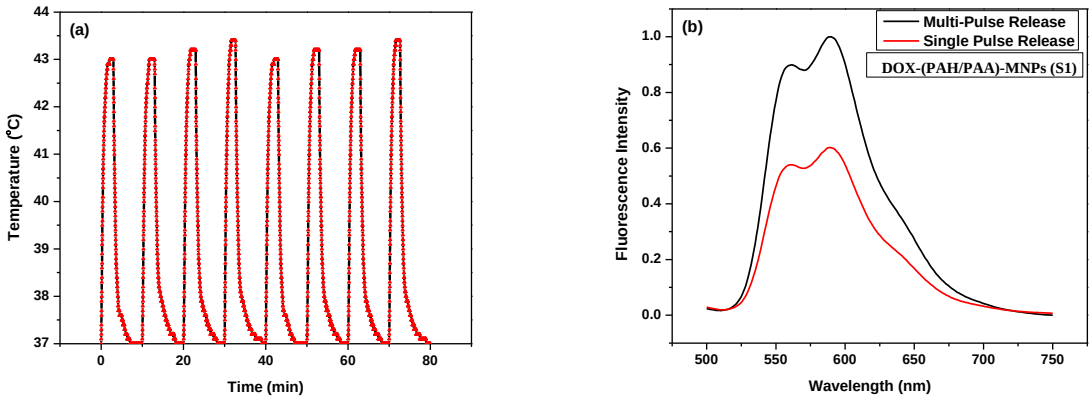

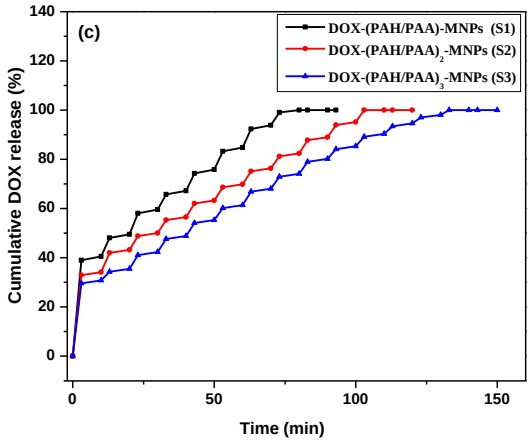

Figure 4.37. a) HF-AMF triggered release of DOX loaded coated CS-MNPs in on-off cycles profiles. b) Fluorescence intensity profiles upon the application of HF-AMF after 80 min in multiple pulses and in a single pulse. c) DOX release profiles upon the application of HF-AMF

Studies on the pH and temperature induced release of DOX were carried out. The extent of DOX release from the sample in the PBS (pH 5.0) is higher than the ones with pH of 7.4 (Figure 4.38a). The 100 min cumulative release in pH 7.4 media is about 40 %, whereas that in pH 5.0 media is about 100%, which indicates that the low pH helps to accelerate the release of DOX at tumor cell.

Cumulative DOX release as a function of time with application of an HF-AMF but at different temperatures, i.e. 25 °C, 37 °C, 40 °C, and 43 °C, in PBS at pH 5 are represented in Figure 4.38b. The amount of DOX released was 43 % at 25 °C due to the hydrolysis kinetic of the layer at acidic pH. On the other hand 65 % of DOX release was observed at 37 °C. After reaching the temperature to 40 °C, the DOX release was strongly enhanced and increased to 77 %. The maximal release of DOX was found at 43 °C. Acidic pH facilitates the release of the drug by promoting the dissociation of the layer adjacent to the heat generated by CS-MNPs after subjected to HF-AMF, which accelerate the rate of the hydrolysis reaction and induce the thermo-responsiveness of the polymer. Thus, by combining both changes of the pH and higher temperature, a controlled release of the DOX can be obtained.

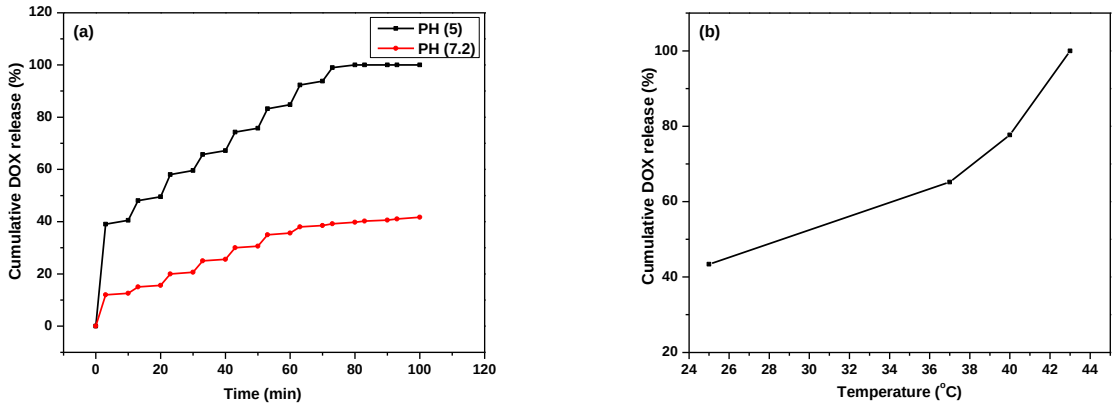

Figure 4.38. a) Cumulative release of DOX upon the application of HF-AMF at different pH for DOX loaded coated CS-MNPs. b) Cumulative DOX release profile as a function of temperature at acidic pH.

Pulsatile drug delivery systems have attracted attraction because of their multiple advantages over conventional dosage forms. They deliver the drug at the selective time, at the selective site of action and in the right amount, which provides more benefit and increased patient compliance. The drug is released slowly and completely as a pulse after a lag time. These products follow the sigmoid release profile characterized by a time period. They reduce the dose frequency, and cost, which reduces the side effects, and thus improving patient compliance.

Some authors developed magnetic hydrogel nanocomposites for remote controlled pulsatile drug release.[109] Nanocomposites were synthesized by incorporation of superparamagnetic Fe_3O_4 particles in negative temperature sensitive poly (*N*-isopropylacrylamide) hydrogels. Other authors use a high-frequency magnetic field to control the pulsatile release of vitamin B_{12} from a ferrogel.[110] Other Using Magnetic Implants for local drug delivery which provide a pulsatile release of the drug.[111] Katono *et al.* developed an interpenetrating polymer networks composed of polyacrylic acid and poly(acrylamide-co-butyl methacrylate), that showed a positive thermosensitvity.[112] The swelling of these hydrogel was reversible, responding to the temperature changes. Ilmain *et al.* reported an interpenetrating network of polyacrylic acid and polyacrylamide that swell above their UCST, due to hydrogen bond between the two different networks.[113] Shin *et al.* designed a temperature- and pH-responsive drug delivery system by using interpenetrating polymer network hydrogels constructed with polyacrylic acid and polyvinyl alcohol.[114]

5 SUMMARY AND CONCLUSION

A multi-perspective investigation, including (i) the selection of MNPs to meet the individual needs of future biomedical applications, (ii) the effect of experimental parameters on the behavior of MNPs, (iii) the functionalization of MNPs and (iv) the drug release investigation, has been carried out in this work. The first part covered general considerations concerning the synthesis of CS-MNPs. It showed how the unique physical and magnetic properties of the CS-MNPs can be specifically tuned by variation of the zinc substitution. The morphology, crystal structure and magnetic properties of the $Zn_xCo_{1-x}Fe_2O_4@MnFe_2O_4$ have been investigated. The formation of $Zn_xCo_{1-x}Fe_2O_4@MnFe_2O_4$ was confirmed by the XRD technique, and TEM. XPS measurements showed the elements distribution, homogeneity, and formation of core/shell of the as prepared samples. The lattice constant, ionic radii, and crystallite size were found to increase with the increase in zinc concentration. The M_s and SAR was found to increase with the increase in zinc substitution (x=0.4) and can be explained in terms of the cation distribution between the tetrahedral and octahedral sites of the spinel structure of the core. Low H_c was observed for the higher Zn concentration for the nanoparticles. The nano-crystallinity and high SAR values of the magnetic nanoparticles suggest it can be used for many practical applications such as magnetic drug delivery, hyperthermia and MRI.

The second part of this thesis covered the structural and magnetic properties of $Zn_{0.4}Co_{0.6}Fe_2O_4@$ $Zn_{0.4}Mn_{0.6}Fe_2O_4$ which can be tailored by the precursor concentration and reaction time. The particle size can easily be controlled by adjusting the reaction time, precursor concentration, and the heating rate. It was demonstrated that the particle size increased with reaction time. The impact of the core/shell $Zn_{0.4}Co_{0.6}Fe_2O_4@$ $Zn_{0.4}Mn_{0.6}Fe_2O_4$ exchange interaction on the specific absorption rate has been investigated. Core/shell exchange coupling leads to an increase of the specific absorption rate. Also the concentration of the precursor and the synthesis time had comparatively effects on the magnetic heating power. We suggest that the present work might be helpful for the design of core/shell particles for a variety of systems that depend on heat induction, including magnetic hyperthermia therapy and drug delivery system. This study is also needed for the proper design of the material based on a choice of the features to be tuned.

In part 3 a novel magnetic drug release system that uses click chemistry reactions on-demand by heating upon AMF has been reported. Our synthetic design, which is based on a different multifunctionalization of CS-MNPs, thus controls the release of the DOX whilst maintaining the colloidal stability and magnetic properties of the CS-MNPs. A fast drug release is activated by rDA reaction and could be applied

synergistically with hyperthermia. At body temperature the amount of released drug is hardly detectable, thus minimizing the adverse effects of anti-cancer drug. Exposure of the system to several distinct temperatures demonstrated a strongly temperature-dependent release of the DOX from the nano-carriers, supporting a DA/rDA mechanism. The drug release rate is controlled by switching “off” or “on” the AMF without significant heating of the medium. High sensitivity and excellent biocompatibility of our versatile system yield an improved efficacy of a medical treatment as outlined above and allow to design of remotely controllable highly functional nano-systems.

In contrast of the rDA activated rapid release system, the part 4 concerned the development of a pH and magnetic dual-responsive drug delivery system, consists of functionalized core/shell bi-magnetic nanoparticles, which – via a layer-by-layer technique – are coated by multiple polyelectrolytes and functionalized with the chemotherapeutics doxorubicin. We expect that a rapid heat generation of CS-MNPs will induce cell necrosis suppressing the development of MDR and thermo-tolerance (e.g. heat shock protein) that usually is associated with slow heating rate. Improved DOX release was observed at acidic environment (pH 5.0) and at higher temperature (43 °C). This behavior approved the multiple stimuli responsive of the nano-carrier. On-off switch controlled release could be successfully tuned through adjustment of the number of layers and the applying magnetic field. Following DLS, Zeta potential and TEM analysis, it was found that the system was highly dispersed and stable in the medium. The system displayed good cytocompatibility, superparamagnetism, and thermosensitivity. The system exhibited a good therapeutic efficacy by providing repeated, long-term, on demand drug delivery for a variety of medical application, thus enhancing the therapeutic efficacy of the drug. Such a novel magnetic drug delivery system makes the functionalized CS-MNPs suitable for cancer treatment.

APPENDIX

A1. CHEMICALS

Description	CAS No.	Supplier
Zinc acetylacetonate hydrate	108503-47-5	Sigma-Aldrich
Cobalt (II) acetylacteonate	14024-48-7	Sigma-Aldrich
Iron (III) acetylacetonate	14024-18-1	ACROS Organics
Manganese (II) acetylacteonate	14024-58-9	Sigma-Aldrich
Tetramethylammonium hydroxide solution	75-59-2	Sigma-Aldrich
Alendronic acid	121268-17-5	Santa Cruz Biotechnology
Oleic acid	112-80-1	Sigma-Aldrich
oleylamine	112-90-3	Sigma-Aldrich
1,2-Hexadecanediol	6920-24-7	Sigma-Aldrich
benzyl ether	103-50-4	Sigma-Aldrich
N-(2-carboxyethyl)maleimide	7423-55-4	Sigma-Aldrich
2-furfuryl isothiocyanate	4650-60-6	Fluka
N-(3-dimethylaminopropyl)-N'-ethylcarbodiimide hydrochloride	25952-53-8	Fluka
N-hydroxysuccinimide	6066-82-6	Sigma-Aldrich
doxorubicin hydrochloride	25316-40-9	Sigma-Aldrich
Poly(acrylic acid)	9003-01-4	Sigma-Aldrich
Poly(allylamine hydrochloride)	71550-12-4	Sigma-Aldrich

A2. LIST OF ABBREVIATIONS

Magnetic nanoparticles	MNPs
Core/shell magnetic nanoparticles	CS-MNPs
Specific absorption rate	SAR
Doxorubicin	DOX
High-frequency alternating magnetic field	HF-AMF
Alternating magnetic field	AMF
Retro Diels/Alder reaction	rDA
Diels/Alder reaction	DA
Layer-by-layer	LBL
Poly(allylamine-hydrochloride)	PAH
polyacrylic acid	PAA
Magnetic resonance imaging	MRI
Reference	ref
Ferromagnet	FM
Antiferromagnet	AFM
Minute	min
Hour	h
Second	sec
N-(3-dimethylaminopropyl)-N'-ethylcarbodiimide hydrochloride	EDC
N-Hydroxysuccinimide	NHS
X-ray diffraction	XRD
Transmission electron microscopy	TEM
Dark-field Transmission electron microscopy	DF-TEM
X-ray photoelectron spectroscopy	XPS
Dynamic light scattering	DLS
Fourier transform infrared spectroscopy	FT-IR
Thermogravimetry	TG
Vibrating sample magnetometery	VSM
Saturation magnetization	M_s
Remanence magnetization	M_r
Coercivity	H_c
Curie temperature	T_c
Binding energy	BE

A3. PUBLICATIONS

A3.1 Journal article

M. Hammad, V. Nica, R. Hempelmann

On-Command Controlled Drug Release by Diels-Alder Reaction Using Bi-Magnetic Core/Shell Nano-carriers. (Submitted to Colloids and Surfaces B: Biointerfaces)

M. Hammad, V. Nica, R. Hempelmann

On-Off Switch Controlled Doxorubicin Release from Thermo- and pH-Responsive Coated Bi-Magnetic Nano-Carriers. (Submitted to Journal of Nanoparticles Research)

M. Hammad, V. Nica, R. Hempelmann

Synthesis and characterization of bi-magnetic core/shell for hyperthermia applications. (Submitted to IEEE Transactions on Magnetics)

M. Hammad, V. Nica, R. Hempelmann

Enhanced Specific Absorption Rate of Bi-magnetic Nanoparticles for Heating Applications. (In preparation)

A3.2 Conference proceedings

M. Hammad and R. Hempelmann

Functionalization of Magnetic Nanoparticles by Diels-Alder Reaction.

15th German Ferrofluid Workshop, 15 - 17 July 2015, Rostock, Germany.

V. Nica, **M. Hammad**, M.L. Garcia Martin, R. Hempelmann

Shape Anisotropic Bi-magnetic Nanoparticles for Application in Hyperthermia.

TIM15-16 Physics Conference, 26 - 28 May 2016, Timisoara, Romania.

M. Hammad, V. Nica, and R. Hempelmann

Synthesis and Characterization of Bi-magnetic Core/Shell for Hyperthermia Applications.

11th European Magnetic Sensors and Actuators**,** 12 - 15 July 2016, Torino, Italy.

V. Nica, **M. Hammad**, M.L. Garcia Martin, R. Hempelmann

Influence of the Surfactants on the Physiochemical Properties of Hard/Soft Bi-magnetic Nanoparticles.
11th European Magnetic Sensors and Actuators**,** 12 - 15 July 2016, Torino, Italy.

V. Nica, **M. Hammad**, M.L. Garcia Martin, R. Hempelmann
On-Command Multifunctional Bi-magnetic Core-Shell Nanoparticles for Biomedical Applications
Advances in Functional Materials (AFM 2016), 8 - 11 Augst 2016, Jeju, South Korea

V. Nica, **M. Hammad**, M.L. Garcia Martin, R. Hempelmann
Enhanced Specific Absorbtion Rate of Exchange Coupled Bi-Magnetic Nanoparticles for High Frequency Electromagnetic Absorption
Europe-Korea Conference on Science and Technology (EKC 2016), 27 - 30 July 2016, Berlin, Germany

A4. ACKNOWLEDGEMENT

I'm very happy to have this opportunity to thank all the people who have helped me during the past years. I was grateful to receive the admission of Saarland University, and to be able to spend my time under the supervision of Prof. Dr. Rolf Hempelmann. I would like to thank my advisor, Prof. Dr. Rolf Hempelmann, for his sharing of passion on science, novel ideas, and confidence. I really appreciate his constant encouragement and mentoring, as well as support.

Special thanks to my partner Dr. Valentin Nica, who measured the magnetization curves and XPS of the magnetic nanoparticles, and for many fruitful discussions. I am very grateful for his help to analyze the measurements.

I have received a lot of help from former and current members in Prof. Hempelmann's group. I appreciate help on the Specific absorption rate measurement from Dan Durneata. Thanks to Dr. Michael Schmitt for DLS measurements. Thanks to Mrs. Sylvia Kuhn for the TEM measurements. Thanks to Rudolf Richter for the help in technical problems.

I'd like to thank Prof. Alexandra Kiemer for the cytotoxicity assay. Also I want to thank Prof. Dr. Gregor Jung and his group member, Michael Vester, for the spectrofluorometry.

Finally, I would like to gratefully thank my family for their love and support, and especially my father for all his encouragement and patience.

Mohaned Hammad

Saarbrücken, 2016

A5. REFERENCES

[1] K. J. Widder, A. E. Senyei, D. G. Scarpelli, *Proc. Soc. Exp. Biol. Med.* **1978**, *158*, 141.
[2] A. Senyei, K. Widder, G. Czerlinski, *J. Appl. Phys.* **1978**, *49*.
[3] S. Laurent, D. Forge, M. Port, A. Roch, C. Robic, L. Vander Elst, R. N. Muller, *Chem. Rev.* **2008**, *108*, 2064.
[4] D. Portet, B. Denizot, E. Rump, J.-J. Lejeune, P. Jallet, *J. Colloid Interface Sci.* **2001**, *238*, 37.
[5] V. F. Puntes, K. M. Krishnan, A. P. Alivisatos, *Science (80-.).* **2001**, *291*, 2115.
[6] A.-H. Lu, E. L. Salabas, F. Schüth, *Angew. Chemie Int. Ed.* **2007**, *46*, 1222.
[7] H. M. Song, Y. J. Kim, J. H. Park, *J. Phys. Chem. C* **2008**, *112*, 5397.
[8] P. Tartaj, M. P. Morales, S. Veintemillas-Verdaguer, T. Gonzalez-Carreño, C. J. Serna, *Handb. Magn. Mater.* **2006**, *16*, 403.
[9] F. X. Redl, C. T. Black, G. C. Papaefthymiou, R. L. Sandstrom, M. Yin, H. Zeng, C. B. Murray, S. P. O'Brien, *J. Am. Chem. Soc.* **2004**, *126*, 14583.
[10] C. B. Murray, C. R. Kagan, M. G. Bawendi, *Annu. Rev. Mater. Sci.* **2000**, *30*, 545.
[11] T. Hyeon, S. S. Lee, J. Park, Y. Chung, H. Bin Na, *J. Am. Chem. Soc.* **2001**, *123*, 12798.
[12] N. R. Jana, Y. Chen, X. Peng, *Chem. Mater.* **2004**, *16*, 3931.
[13] K. Butter, A. . Philipse, G. . Vroege, *J. Magn. Magn. Mater.* **2002**, *252*, 1.
[14] Z. J. Zhang, Z. L. Wang, B. C. Chakoumakos, J. S. Yin, *J. Am. Chem. Soc.* **1998**, *120*, 1800.
[15] S. Neveu, A. Bee, M. Robineau, D. Talbot, *J. Colloid Interface Sci.* **2002**, *255*, 293.
[16] Y. Il Kim, D. Kim, C. S. Lee, *Phys. B Condens. Matter* **2003**, *337*, 42.
[17] R. H. Kodama, S. A. Makhlouf, A. E. Berkowitz, *Phys. Rev. Lett.* **1997**, *79*, 1393.
[18] Y. Ce, H. Yang-Long, G. Song, *Chinese Phys. B* **2014**, *23*, 57505.
[19] A. P. Guimarães, *Principles of Nanomagnetism*, Springer Berlin Heidelberg, **2010**.
[20] F. E. Luborsky, *J. Appl. Phys.* **1961**, *32*.
[21] L. Néel, *J. Phys. le Radium* **1950**, *11*, 49.
[22] C. M. Sorensen, in *Nanoscale Mater. Chem.*, John Wiley & Sons, Inc., **2002**, pp. 169–221.
[23] E. F. Kneller, R. Hawig, *IEEE Trans. Magn.* **1991**, *27*, 3560.
[24] R. Coehoorn, D. B. de Mooij, C. de Waard, *J. Magn. Magn. Mater.* **1989**, *80*, 101.
[25] J. Nogués, I. K. Schuller, *J. Magn. Magn. Mater.* **1999**, *192*, 203.
[26] V. Skumryev, S. Stoyanov, Y. Zhang, G. Hadjipanayis, D. Givord, J. Nogues, *Nature* **2003**, *423*, 850.
[27] K. Sone, H. Naganuma, M. Ito, T. Miyazaki, T. Nakajima, S. Okamura, *Sci. Rep.* **2015**, *5*, 9348.
[28] F. Liu, J. Zhu, W. Yang, Y. Dong, Y. Hou, C. Zhang, H. Yin, S. Sun, *Angew. Chemie Int. Ed.* **2014**, *53*, 2176.
[29] Z. Li, M. Kawashita, N. Araki, M. Mitsumori, M. Hiraoka, M. Doi, *Mater. Sci. Eng. C* **2010**, *30*, 990.
[30] R. Hergt, W. Andra, C. G. d'Ambly, I. Hilger, W. A. Kaiser, U. Richter, H. G. Schmidt, *IEEE Trans. Magn.* **1998**, *34*, 3745.
[31] A. E. Deatsch, B. A. Evans, *J. Magn. Magn. Mater.* **2014**, *354*, 163.
[32] W. F. Brown, *Phys. Rev.* **1963**, *130*, 1677.
[33] R. E. Rosensweig, *J. Magn. Magn. Mater.* **2002**, *252*, 370.
[34] D. Kriterien, **1976**.
[35] K. J. Widder, R. M. Morris, G. A. Poore, D. P. Howard, A. E. Senyei, *Eur. J. Cancer Clin. Oncol.* **1983**, *19*, 135.
[36] P. Wust, B. Hildebrandt, G. Sreenivasa, B. Rau, J. Gellermann, H. Riess, R. Felix, P. M. Schlag, *Lancet Oncol.* **2002**, *3*, 487.
[37] K. Maier-Hauff, R. Rothe, R. Scholz, U. Gneveckow, P. Wust, B. Thiesen, A. Feussner, A. von Deimling, N. Waldoefner, R. Felix, A. Jordan, *J. Neurooncol.* **2007**, *81*, 53.

[38] U. Jeong, X. Teng, Y. Wang, H. Yang, Y. Xia, *Adv. Mater.* **2007**, *19*, 33.
[39] E. Terreno, D. D. Castelli, A. Viale, S. Aime, *Chem. Rev.* **2010**, *110*, 3019.
[40] R. Qiao, C. Yang, M. Gao, *J. Mater. Chem.* **2009**, *19*, 6274.
[41] A. Ito, M. Shinkai, H. Honda, T. Kobayashi, *J. Biosci. Bioeng.* **2005**, *100*, 1.
[42] C. Corot, K. G. Petry, R. Trivedi, A. Saleh, C. Jonkmanns, J.-F. Le Bas, E. Blezer, M. Rausch, B. Brochet, P. Foster-Gareau, D. Balériaux, S. Gaillard, V. Dousset, *Invest Radiol* **2004**, *39*, 619.
[43] J.-H. Lee, Y.-M. Huh, Y. Jun, J. Seo, J. Jang, H.-T. Song, S. Kim, E.-J. Cho, H.-G. Yoon, J.-S. Suh, J. Cheon, *Nat Med* **2007**, *13*, 95.
[44] D. K. Yi, S. T. Selvan, S. S. Lee, G. C. Papaefthymiou, D. Kundaliya, J. Y. Ying, *J. Am. Chem. Soc.* **2005**, *127*, 4990.
[45] A. Gandini, *Prog. Polym. Sci.* **2013**, *38*, 1.
[46] K. C. Nicolaou, S. A. Snyder, T. Montagnon, G. Vassilikogiannakis, *Angew. Chemie Int. Ed.* **2002**, *41*, 1668.
[47] J. M. Palomo, *European J. Org. Chem.* **2010**, *2010*, 6303.
[48] M. Gregoritza, F. P. Brandl, *Eur. J. Pharm. Biopharm.* **2015**, *97, Part B*, 438.
[49] A.-C. Knall, M. Hollauf, C. Slugovc, *Tetrahedron Lett.* **2014**, *55*, 4763.
[50] D. C. Rideout, R. Breslow, *J. Am. Chem. Soc.* **1980**, *102*, 7816.
[51] A. D. De Araújo, J. M. Palomo, J. Cramer, O. Seitz, K. Alexandrov, H. Waldmann, *Chem. - A Eur. J.* **2006**, *12*, 6095.
[52] C. M. Nimmo, S. C. Owen, M. S. Shoichet, *Biomacromolecules* **2011**, *12*, 824.
[53] Y. Jiao, J. Parra, P. Akcora, *Macromolecules* **2014**, *47*, 2030.
[54] O. Azzaroni, K. H. A. Lau, *Soft Matter* **2011**, *7*, 8709.
[55] B. Fischer, J. Wagner, M. Schmitt, V. Trieu, R. Hempelmann, *Zeitschrift f{\textbackslash}{ü}r Phys. Chemie* **2006**, *220*, 69.
[56] S. F. Medeiros, A. M. Santos, H. Fessi, A. Elaissari, *Int. J. Pharm.* **2011**, *403*, 139.
[57] R. K. Iler, *J. Colloid Interface Sci.* **1966**, *21*, 569.
[58] G. Decher, J.-D. Hong, *Makromol. Chemie. Macromol. Symp.* **1991**, *46*, 321.
[59] Y. Lvov, G. Decher, H. Moehwald, *Langmuir* **1993**, *9*, 481.
[60] S. Sun, H. Zeng, D. B. Robinson, S. Raoux, P. M. Rice, S. X. Wang, G. Li, *J. Am. Chem. Soc.* **2004**, *126*, 273.
[61] S. Noh, W. Na, J. Jang, J.-H. Lee, E. J. Lee, S. H. Moon, Y. Lim, J.-S. Shin, J. Cheon, *Nano Lett.* **2012**, *12*, 3716.
[62] C. Liu, B. Zou, A. J. Rondinone, Z. J. Zhang, *J. Am. Chem. Soc.* **2000**, *122*, 6263.
[63] R. D. Shannon, *Acta Crystallogr. Sect. A* **1976**, *32*, 751.
[64] H. Xia, D. Zhu, Y. Fu, X. Wang, *Electrochim. Acta* **2012**, *83*, 166.
[65] Y. Fu, P. Xiong, H. Chen, X. Sun, X. Wang, *Ind. Eng. Chem. Res.* **2012**, *51*, 725.
[66] H. W. Nesbitt, D. Banerjee, *Am. Mineral.* **1998**, *83*, 305.
[67] G. C. Allen, K. R. Hallam, *Appl. Surf. Sci.* **1996**, *93*, 25.
[68] D. Sibera, J. Kaszewski, D. Moszyński, E. Borowiak-Paleń, W. Łojkowski, U. Narkiewicz, *Phys. status solidi* **2010**, *7*, 1420.
[69] J. M. Hastings, L. M. Corliss, *Rev. Mod. Phys.* **1953**, *25*, 114.
[70] P. G. Bercoff, H. R. Bertorello, *J. Magn. Magn. Mater.* **1997**, *169*, 314.
[71] J. Smit, H. P. J. Wijn, **1959**, 384.
[72] Y. Yafet, C. Kittel, *Phys. Rev.* **1952**, *87*, 290.
[73] M. P. Morales, S. Veintemillas-Verdaguer, M. I. Montero, C. J. Serna, A. Roig, L. Casas, B. Martínez, F. Sandiumenge, *Chem. Mater.* **1999**, *11*, 3058.
[74] A. Skumiel, *J. Magn. Magn. Mater.* **2006**, *307*, 85.
[75] S. H. Chung, A. Hoffmann, S. D. Bader, C. Liu, B. Kay, L. Makowski, L. Chen, *Appl. Phys. Lett.* **2004**,

85.
[76] V. Nica, H. M. Sauer, J. Embs, R. Hempelmann, *J. Phys. Condens. Matter* **2008**, *20*, 204115.
[77] D. S. B. and E. M. B. and E. N. Miranda, *J. Phys. Condens. Matter* **2012**, *24*, 226004.
[78] V. Lopez-Dominguez, J. M. Hernàndez, J. Tejada, R. F. Ziolo, *Chem. Mater.* **2013**, *25*, 6.
[79] Y. Jun, J. Seo, J. Cheon, *Acc. Chem. Res.* **2008**, *41*, 179.
[80] J. Jang, H. Nah, J.-H. Lee, S. H. Moon, M. G. Kim, J. Cheon, *Angew. Chemie Int. Ed.* **2009**, *48*, 1234.
[81] a Kostopoulou, K. Brintakis, M. Vasilakaki, K. N. Trohidou, a P. Douvalis, a Lascialfari, L. Manna, a Lappas, *Nanoscale* **2014**, *6*, 3764.
[82] J. Park, A. N. Pasupathy, J. I. Goldsmith, C. Chang, Y. Yaish, J. R. Petta, M. Rinkoski, J. P. Sethna, H. D. Abruna, P. L. McEuen, D. C. Ralph, *Nature* **2002**, *417*, 722.
[83] N. V. Long, Y. Yang, T. Teranishi, C. M. Thi, Y. Cao, M. Nogami, *RSC Adv.* **2015**, *5*, 56560.
[84] M. Oku, K. Hirokawa, *J. Electron Spectros. Relat. Phenomena* **1976**, *8*, 475.
[85] Z.-Y. Tian, P. H. Tchoua Ngamou, V. Vannier, K. Kohse-Höinghaus, N. Bahlawane, *Appl. Catal. B Environ.* **2012**, *117–118*, 125.
[86] M. C. Biesinger, B. P. Payne, A. P. Grosvenor, L. W. M. Lau, A. R. Gerson, R. S. C. Smart, *Appl. Surf. Sci.* **2011**, *257*, 2717.
[87] T. Herranz, S. Rojas, M. Ojeda, F. J. Pérez-Alonso, P. Terreros, K. Pirota, J. L. G. Fierro, *Chem. Mater.* **2006**, *18*, 2364.
[88] S. Yang, Y. Guo, N. Yan, D. Wu, H. He, Z. Qu, J. Jia, *Ind. Eng. Chem. Res.* **2011**, *50*, 9650.
[89] K. Zhang, W. Zuo, Z. Wang, J. Liu, T. Li, B. Wang, Z. Yang, *RSC Adv.* **2015**, *5*, 10632.
[90] S. Bera, A. A. M. Prince, S. Velmurugan, P. S. Raghavan, R. Gopalan, G. Panneerselvam, S. V Narasimhan, *J. Mater. Sci.* **n.d.**, *36*, 5379.
[91] M. Vijayaraj, C. S. Gopinath, *J. Catal.* **2006**, *241*, 83.
[92] Y.-N. NuLi, Y.-Q. Chu, Q.-Z. Qin, *J. Electrochem. Soc.* **2004**, *151*, A1077.
[93] A. A. Tahir, K. G. U. Wijayantha, *J. Photochem. Photobiol. A Chem.* **2010**, *216*, 119.
[94] X. Liang, P. Liu, H. He, G. Wei, T. Chen, W. Tan, F. Tan, J. Zhu, R. Zhu, *J. Hazard. Mater.* **2016**, *306*, 305.
[95] Q. A. Pankhurst, J. Connolly, S. K. Jones, J. Dobson, *J. Phys. D. Appl. Phys.* **2003**, *36*, 167.
[96] M. Bokhari, R. J. Carnachan, N. R. Cameron, S. A. Przyborski, *J. Anat.* **2007**, *211*, 567.
[97] A. P. Bapat, J. G. Ray, D. A. Savin, E. A. Hoff, D. L. Patton, B. S. Sumerlin, *Polym. Chem.* **2012**, *3*, 3112.
[98] B. J. Adzima, C. J. Kloxin, C. N. Bowman, *Adv. Mater.* **2010**, *22*, 2784.
[99] F. K. Storm, W. H. Harrison, R. S. Elliott, D. L. Morton, *Cancer Res.* **1979**, *39*, 2245.
[100] S. Hegewisch-Becker, K. Braun, M. Otte, A. Corovic, D. Atanackovic, A. Nierhaus, D. K. Hossfeld, K. Pantel, *Clin. Cancer Res.* **2003**, *9*, 2079.
[101] G. C. Li, N. F. Mivechi, G. Weitzel, *Heat Shock Proteins, Thermotolerance, and Their Relevance to Clinical Hyperthermia*, **1995**.
[102] R. L. Anderson, T. S. Herman, I. Van Kersen, G. M. Hahn, *Int. J. Radiat. Oncol.* **1988**, *15*, 717.
[103] L. Che Rose, J. C. Bear, P. Southern, P. D. McNaughter, R. Ben Piggott, I. P. Parkin, S. Qi, B. P. Hills, A. G. Mayes, *J. Mater. Chem. B* **2016**, *4*, 1704.
[104] T. T. T. N'Guyen, H. T. T. Duong, J. Basuki, V. Montembault, S. Pascual, C. Guibert, J. Fresnais, C. Boyer, M. R. Whittaker, T. P. Davis, L. Fontaine, *Angew. Chemie - Int. Ed.* **2013**, *52*, 14152.
[105] A. Riedinger, P. Guardia, A. Curcio, M. A. Garcia, R. Cingolani, L. Manna, T. Pellegrino, *Nano Lett.* **2013**, *13*, 2399.
[106] S. Yamashita, H. Fukushima, Y. Niidome, T. Mori, Y. Katayama, T. Niidome, *Langmuir* **2011**, *27*, 14621.
[107] Y. Yuan, D.-A. B. Tasciuc, *J. Magn. Magn. Mater.* **2011**, *323*, 2463.
[108] L. Wang, Y. Yan, M. Wang, H. Yang, Z. Zhou, C. Peng, S. Yang, *J. Mater. Chem. B* **2016**, *4*, 1908.

[109] N. S. Satarkar, J. Z. Hilt, *J. Control. Release* **2008**, *130*, 246.
[110] S. Hu, T. Liu, D. Liu, S. Chen, *Langmuir* **2007**, *12*, 11.
[111] A. J. Rosengart, M. D. Kaminski, H. Chen, P. L. Caviness, A. D. Ebner, J. A. Ritter, *J. Magn. Magn. Mater.* **2005**, *293*, 633.
[112] H. Katono, A. Maruyama, K. Sanui, N. Ogata, T. Okano, Y. Sakurai, *J. Control. Release* **1991**, *16*, 215.
[113] F. Ilmain, T. Tanaka, E. Kokufuta, *Nature* **1991**, *349*, 400.
[114] H. S. Shin, S. Y. Kim, Y. M. Lee, *J. Appl. Polym. Sci.* **1997**, *65*, 685.